Femtosecond Laser Joining of Silver Submicron/Nanoparticles

by

Hong Huang

A thesis

presented to University of Waterloo

in fulfillment of the

thesis requirement for the degree of

Doctor of Philosophy

in

Mechanical Engineering

Waterloo, Ontario, Canada, 2015

Author’s Declaration

This thesis consists of material all of which I authored or co-authored: see Statement of Contributions included in the thesis. This is a true copy of the thesis, including any required final revision, as accepted by my examiners.

I understand that my thesis may be made electronically available to the public.

Statement of Contributions

During the PhD study since September 2011, five peer-reviewed journal papers (as first author) have been published, with an additional one which contributes to the thesis under review. Among the five published papers, four of them are directly related to the thesis; and the other one also covers the topic of fs laser joining. In addition, four co-authored papers which cover fs laser fabrication and plasmonics are published as well.

1. **H. Huang**, W. W. Duley, and Y. Zhou, "Oxygen assisted interconnection of silver submicron/nanoparticles with femtosecond laser radiation", submitted. (Thesis work)

2. **H. Huang**, M. Sivayoganathan, W. W. Duley, and Y. Zhou, "High integrity interconnection of silver submicron/nanoparticles on silicon wafer by femtosecond laser irradiation", Nanotechnology, 26 (2015), 025303. (Thesis work)

3. **H. Huang**, M. Sivayoganathan, W. W. Duley, and Y. Zhou, "Efficient localized heating of silver nanoparticles by low-fluence femtosecond laser pulses", Applied Surface Science, 331(2015), 392–398. (Thesis work)

4. **H. Huang**, A. Hu, M. Sivayoganathan, W. W. Duley, Z. H. Huang, and Y. Zhou, "Femtosecond laser fabrication of silver plasmonic structures for application as single particle SERS detectors", Materials Research Express, 1(2014), 025022. (Thesis work)

5. **H. Huang**, L. Liu, P. Peng, A. Hu, W. W. Duley, and Y. Zhou, "Controlled joining of silver nanoparticles with femtosecond laser radiation", Journal of Applied Physics, 112(2012), 123519. (Thesis work)

6. **H. Huang**, A. Hu, P. Peng, W. W. Duley, and Y. Zhou, "Femtosecond laser-induced microwelding of silver and copper", Applied Optics, 52(2013), 1211-1217. (PhD work)

7. **H. Huang**, W. W. Duley, and Y. Zhou, "Femtosecond laser micro-joining of silver and copper: investigation of joint strength and joining mechanism", submitted. (PhD work)

8. L. Lin, **H. Huang**, M. Sivayoganathan, L. Liu, G. Zou, W. Duley, Y. Zhou, "Assembly of silver nanoparticles on nanowires into ordered nanostructures with femtosecond laser radiation", Applied Optics, 54(2015), 2524-2531. (PhD work)

9. Z. Jiao, **H. Huang**, L. Liu, A. Hu, W. Duley, P. He, and Y. Zhou, "Nanostructure evolution in joining of Al and Fe nanoparticles with femtosecond laser irradiation", Journal of Applied Physics 115(2014), 134305. (PhD work)

10. L. Liu, **H. Huang**, A. Hu, G. Zou, L. Quintino, and Y. Zhou, "Nano Brazing of Pt-Ag Nanoparticles under Femtosecond Laser Irradiation", Nano-Micro Letters, 5(2013), 88-92. (PhD work)

11. P. Peng, **H. Huang**, A. Hu, A. P. Gerlich, and Y. Zhou, "Functionalization of Silver Nanowire Surfaces with Copper Oxide for Surface-Enhanced Raman Spectroscopic Bio-Sensing", Journal of Materials Chemistry, 22(2012), 15495-15499. (PhD work)

Conference:

1. **H. Huang**, A. Hu, P. Peng, W. W. Duley, Y. Zhou, "Femtosecond laser welding Ag microwire to Cu substrate", Oral presentation, 2012 Material Science & Technology conference, Pittsburgh, USA.

Abstract

The development of future devices is towards to the miniaturization and performance improvement. This requires the large scale integration of nanodevices. Nanojoining is an essential step for the industrial scale production of nanodevices which possess extensive applications in nanoelectronics, nanophotonics and biomedicines. Many techniques have been developed to produce nanojoining, and among them femtosecond (fs) laser nanojoining is a promising one due to its limited thermal damage to the fabricated nanomaterials. However the fs laser nanojoining technique is still not probably characterized. In this thesis, the research of fs laser nanojoining of silver (Ag) nanomaterials with or without polyvinylpyrrolidone (PVP) coating is conducted in different environments (aqueous solution, air, vacuum), targeting to different application areas.

It is reported that the joining behavior of PVP coated Ag nanoparticles (NPs) can be manipulated by controlling the distribution of localized surface plasmon induced electric field enhancement (or hotspots) and/or the decomposition of PVP coatings into amorphous carbon or some ionized products. This facilitates the fabrication of joined-NPs structures with tunable plasmonic properties by tuning the geometries of the structures, for possible application as SERS (surface enhanced Raman spectroscopy) detector. For Ag particles without PVP coating and exposed to vacuum (10^{-6} Torr), their joining behavior under fs laser radiation is also controlled by the hotspots; and high integrity interconnection of Ag particles can be obtained benefiting from the localized ablation of the particles in the hotspots. The joining efficiency can be improved by introducing reactive oxygen gas which

produces external heating to the irradiated particles through O-Ag reaction on the surface of Ag particles in the hotspots.

Overall, the hotspots-dependent fs laser nanojoining technique which is developed in this research provides an alternative way for precise fabrication of nanodevices based on the interconnection of nanoscale functional components.

Acknowledgements

Greatest gratitude goes to my supervisors Dr. Y. Norman Zhou, and Dr. Walter W. Duley. I am indebted to Dr. Zhou for introducing me into the project of femtosecond laser nanojoining and awarding me the full freedom of exploring the unknowns in the field; and I sincerely admire his stringent attitude to scientific research. I appreciate Dr. Duley for his tremendous support not only in research but also in the daily life. His encyclopedic knowledge helps me avoid lots of useless effort input. I really enjoy the discussions with him and the coming out of exciting ideas. Finishing this work cannot be possible, without the continuous guidance and support from both of my supervisors.

I would like to thanks the help from Dr. Lei Liu at Tsinghua University and Dr. Anming Hu at the University of Tennessee. The cooperation with them in the first two years of my PhD study when they were at University of Waterloo, build a good starting point of purchasing my PhD degree. I would also like to thank Dr. Mugunthan Savayoganathan, Dr. Yuquan Ding and Dr. Scott Lawson at University of Waterloo for their helps and suggestions in experimental and thesis writing. Special thanks go to Dr. Peng Peng at University of Waterloo for his thoughtful discussion and suggestions on research, and for the help all the way through my PhD study. And thanks all my friends in CAMJ group and in Waterloo for their kind helps, and the happy time with them.

Financial support from the four-year term State Scholarship Fund of China is greatly appreciated.

Finally, I would like to express my deepest appreciation to my parents for their understanding and unconditional support, to my wife Cuiping Wu for her love, encouragement, and continuous support, and to my son Jake for bringing me the happiness.

Dedication

To My Family

Table of Contents

List of Figures

List of Symbols

ε	dielectric function of materials
k^*	wave number
l	number of surface plasmon mode
ω_p	plasma frequency
ω_l	frequency of surface plasmon
ω_{LSP}	frequency of localized surface plasmon
n_0	conduction electrons density
e	electron charge
ε_0	permittivity of the vacuum
m_0	effective mass of electron
α	polarizability
n_m	refractive index of dielectric material
$\langle S \rangle$	Poynting vector
c	speed of light
Q_{abs}	absorption efficiency
A^*	geometrical cross-section
m	complex refractive index
f	filling factor
K	imaginary part of the complex refractive index
σ_{ex}, σ_{sca}, σ_{abs}	extinction, scattering and absorption cross-sections
A	ratio between particle size and wavelength of light
λ, I	wavelength and intensity of laser light
r	radius of nanoparticles
τ_L,	pulse duration
τ_e, τ_l	electron cooling time, lattice heating time
β	attenuation constant
δ_s, δ_p	skin layer depth, laser penetration depth
L_{diff}	thermal diffusion length
T_e, T_l	electron and lattice temperature
k_e, k_l	electron and lattice thermal conductivity
C_e , C_l	electron and lattice heat capacity
γ	electron-lattice interaction factor
F	laser fluence
C	heat capacity
ρ	volumetric mass density
E_{abs}	absorbed energy
H_m	enthalpy of formation
V	volume of nanoparticles

Chapter 1 Introduction

1.1 Nanomaterial and Nanojoining

Nanomaterials are defined as materials with sizes less than one hundred nanometers (nm) in at least one dimension. Based on the number of dimensions, nanomaterials can usually be classified into: (1) zero-dimensional (0D) nanoparticle (NP); (2) one-dimensional (1D) nanowire, nanobelt, nanotube etc.; (3) two-dimensional (2D) nanosheet, nanofilm and so on; (4) three-dimensional (3D) structured nanomaterial. When the size of the materials goes down to nanometer scale, the size effect allows the nanomaterials to possess some unique properties compared to bulk materials.

One effect is the depression of melting temperature. Size-dependent melting was first reported by Takagi [1]; it was shown that the melting temperature of the material decreases with the reduction of its size. In Fig.1-1 a transmission electron microscope (TEM) study is summarized illustrating the relationship between the size and melting temperature of SiO_2 encapsulated silver (Ag) NP, which indicates that the melting temperature of Ag NP whose size was less than ~50 nm decreased nonlinearly with its size [2]. This effect is now coming into industrial use, as nanoparticles (NPs) have been widely studied as low temperature paste for application in microelectronics packing [3], and are paving the way to the application in flexible electronics.

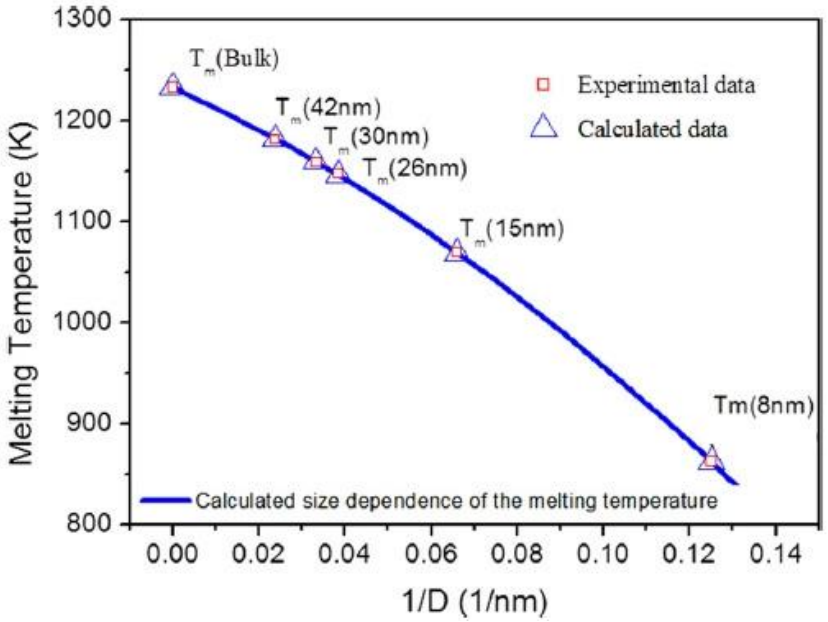

Fig.1-1, Size dependence of the melting temperature (T_m) of silica-encapsulated Ag NPs. The solid line is the fit of the calculated data with respect to the particle size (D, nm) using equation $T_m(K)=1233.65-1954.3/D-8100/D^2$. The figure is adapted from ref. [2].

Another important size-dependent property of the nanomaterials is the formation of localized surface plasmon (LSP), which is defined as the collective oscillation of free electrons near the surface of metallic nanomaterials. This can significantly enhance the localized electric field, forming hotspots in the nanomaterial and the surroundings especially when the frequency of the excitation light is in resonance with that of the LSP, facilitating the application in optical detections such as surface enhance Raman scattering (SERS), fluorescence, and thermal imaging [4, 5]. As the scanning electron microscope (SEM) images shown in Fig.1-2, the presence of Ag NPs on Si wafer or AAO substrate can significantly enhance the Raman signal of the methylene blue, compared to that of the pure Si wafer [6].

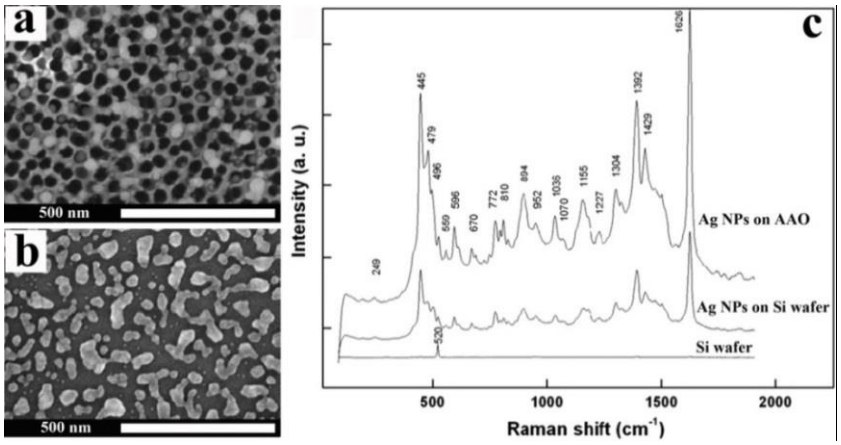

Fig.1-2, SEM images of morphology for Ag NPs deposited on different wafers and their SERS spectra. (a) Ag NPs on Si wafer; (b) Ag NPs on AAO substrate; (c) SERS spectra of methylene blue on three different substrates. The figure is adapted from ref. [6].

NPs also have many other size-dependent properties such as catalytic activity [7, 8]. This is beyond the scope of this work and will not be discussed here. Due to their unique chemical [9], electronic [10], magnetic [11] and optical [12] properties, nanomaterials, especially metallic nanomaterials have been of great interest to researchers for decades.

Recently, a major focus of research into nanomaterials has involved the directed interconnection of nanomaterial building blocks into nanodevices for applications such as bio-sensing [13], solar energy harvesting [14], and photothermal imaging [15]. The techniques which have involved interconnecting nanomaterials building blocks or the building blocks to substrate can be defined as nanojoining technology (or nanojoining in short) [16]. Nanojoining is now developing rapidly and is considered as a key technology to achieve industrial scale production of nanodevices or nano-systems. The principle of nanojoining is to join the nanomaterials by producing adhesive bonding through (bio)polymer molecules or by forming robust primary chemical bonds (metallic, ionic and covalent bonds) [16]. The former is usually obtained by utilizing chemical methods, while the latter is realized through physical methods.

1.2 Issues in Nanojoining

Before the commercial application of nanojoining technology, three major issues in nanojoining process development have to be solved. The first is how to position the nanomaterials and control the final structure of the joined nanomaterial; the second is how to avoid damage to the nanomaterial and the surrounding in the joining process; and the last one is how to produce robust joints and obtain stable performances of the joined structures. To solve these issues, many methods have been developed. For example, the electron beam lithography technique has been used to produce pre-joined nanomaterial to control the exact position of joint formation and the geometry of the final joined structure [17]. Adhesive bonding or cold welding (room temperature welding) has been employed to perform nanojoining without causing damage to the pre-joined nanomaterials [18]. The following sections outline some examples of nanojoining methods and summarize their limitations.

1.2.1 Nanojoining by chemical methods

In chemical methods, deoxyribonucleic acid (DNA) has been widely used to join nanomaterials, because of its good controllability on the final joined structures [19-21]. For example, gold (Au) NPs core-satellite structures [22] were produced through the hybridization of DNA which was bonded on the surface of Au NPs, as shown in Fig.1-3. Other polymer molecules such as poly(methyl methacrylate) (PMMA), and PEGMA (poly(ethylene glycol methacrylate)) were also studied [23, 24]. To obtain better control of the final joined structures, electric or magnetic fields can also be used to assist the joining process. As shown in Fig.1-4, ferromagnetic nanowires (NWs) can be joined and aligned along the direction of magnetic field [25].

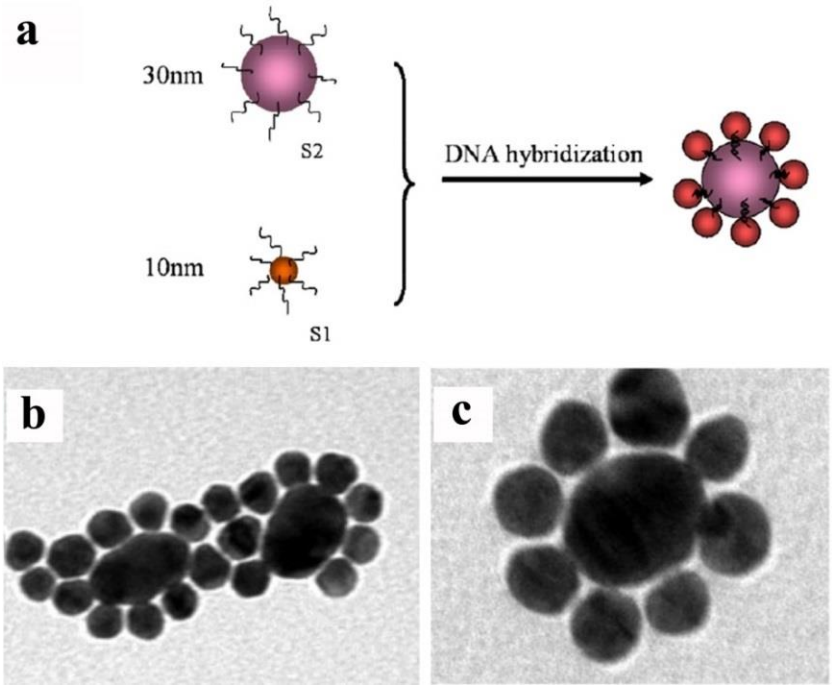

Fig.1-3, DNA assembled Au NPs core-satellite structures, (a) Illustration of the strategy to prepare core-satellite assemblies; (b, c) TEM images of the Au NPs core-satellite structures. The size of the core particles is ~ 30 nm while that of the satellite particles is ~ 10 nm. The figure is adapted from ref. [22].

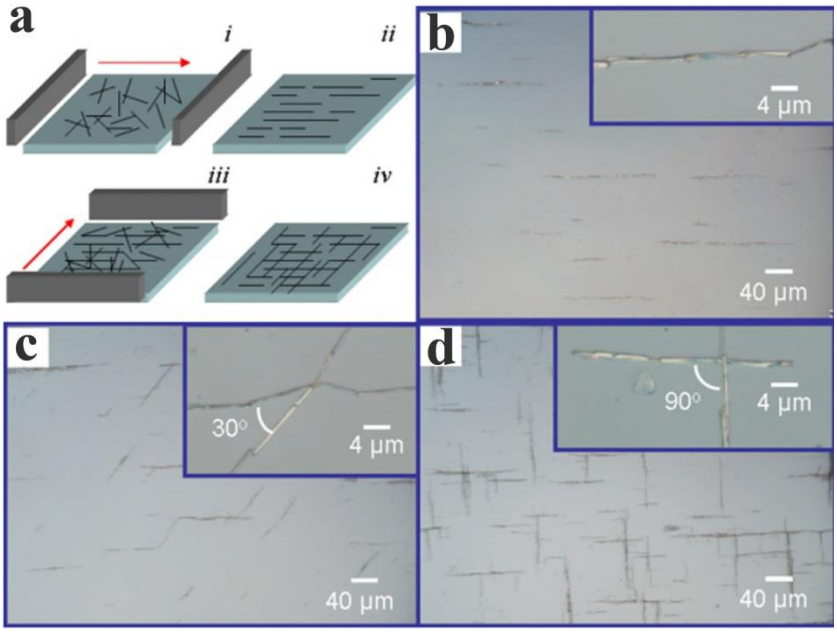

Fig.1-4. (a) Schematic illustrating the two-step process for sequential alignment: (*i*, *ii*) dispensing of the nanowire suspension and (*iii*, *iv*) alignment of the nanowires in an external magnetic field (red arrows). (b) The alignment of the nanowires in a single direction using a 760 G field. (c) Two-step alignment with the substrate shift of 30 º. (d) Two-step alignment with a substrate shift of 90 º. The figure is adapted from ref. [25].

By using chemical methods, nanomaterials can also be joined through the formation of primary chemical bonds. This is usually performed by cleaning off the protective polymer shell on the surface of nanomaterials which results in surface energy-driven mutual diffusion of the nanomaterials, which is known as room temperature welding or cold welding [26]. Directional joining of the nanomaterials can even be obtained if the protective polymers are selectively removed. As shown in Fig.1-5, Au nanorods (NRs) were welded end-to-end by selectively cleaning the cetyltrimethylammonium bromide (CTAB) coating from the ends of the NRs [27].

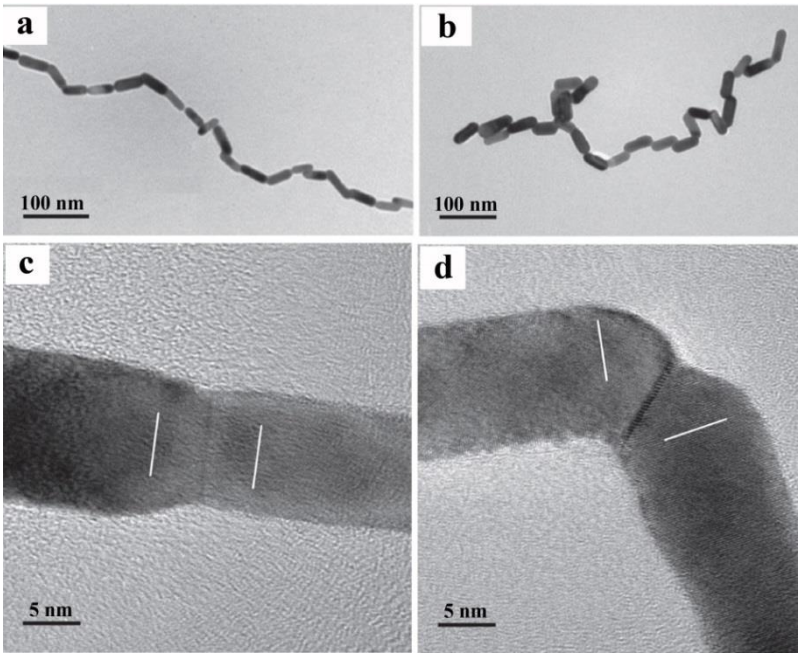

Fig.1-5, TEM images and High-resolution TEM (HRTEM) images of cold welded Au NRs. (a, b) TEM images of the Au NRs solution; (c, d) HRTEM of the NRs joints. (c) shows the perfect end-to-end welding while (d) represents the twined end-to-end welding. The figure is adapted from ref. [27].

1.2.2 Nanojoining by physical methods

Compared to chemical methods, physical methods for nanojoining are straightforward. They include the application of heat [3], force [28], radiation [29-31], soldering material [32], spark plasma [33, 34], and electron beam [35] to join the nanomaterial by producing robust primary chemical bonds. For example, Hu *et al*. [3] obtained Ag NPs networks by

sintering the Ag NPs film in furnace at temperature > 373 K. In the sintering process, softening or fusion of the nanomaterials takes place during their exposure to thermal heating, and then the nanomaterials are joined via solid state diffusion (low temperature heating) [36, 37] or viscous flow and solidification (high temperature heating) [38] at the interface. To accelerate the joining process and improve the joint strength in the thermal heating process, external pressure is usually applied [39], but the possible stress-induced damage to the substrate has to be monitored.

To obtain more precise fabrication, localized heating and joining are required. This can be done by combining the SEM equipment and localized electric thermal heating system. As shown in Fig.1-6, two slightly separated Pt submicron wires (~ 650 nm wide) were welded by employing an electro-thermal system to heat the wires up to their melting point [40]. Due to the higher resistance in the segment between the wires, the effective localized heating took place in the segment and resulted in the welding of the wires. Meanwhile, Xu *et al.* [35] demonstrated that localized welding of the crossed Au NWs could also be obtained by focusing high intensity electron beam (HIEB) in the overlap area of the NWs under TEM observation. However HIEB radiation induced destruction of the Au NWs and the carbon substrate probably limits its application for nanojoining. Using nanoscale solder is an alternative method to achieve localized nanojoining together with reduced damage of the nanomaterials. As shown in Fig.1-7, two Au NWs were joined together via the heated NW solder which diffused onto the junction; and the remaining nanowire solder was removed by using mechanical force after the joining process [32]. The possible limitations are the high cost of the soldering system and its low joining efficiency.

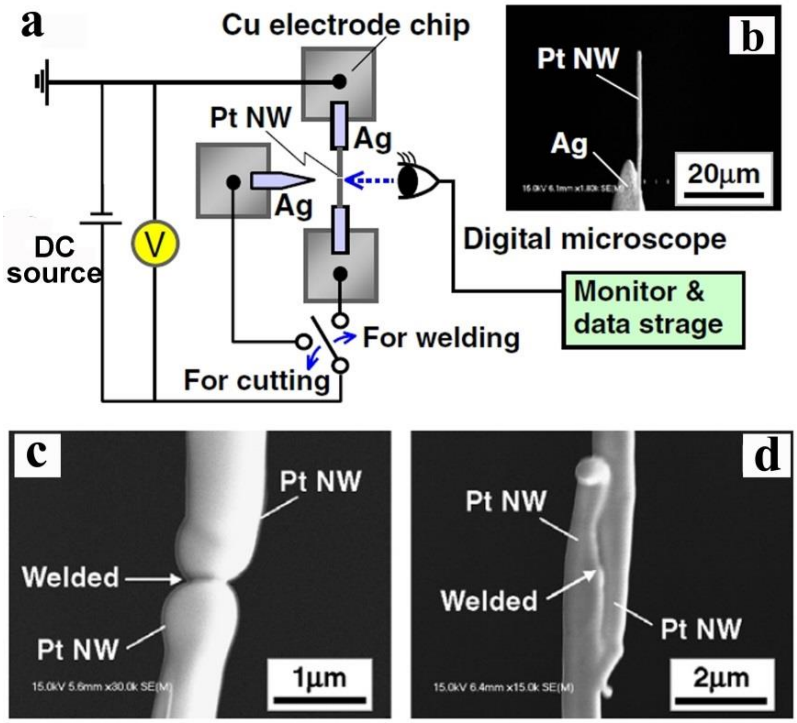

Fig.1-6, Joining of Pt NWs by joule heating. (a,b) Experimental setup for welding Pt nanowires by joule heating; (c) Joint morphology observation of straight welded Pt NWs; (d) Joint morphology of lap welded Pt NWs. The figure is adapted from ref. [40].

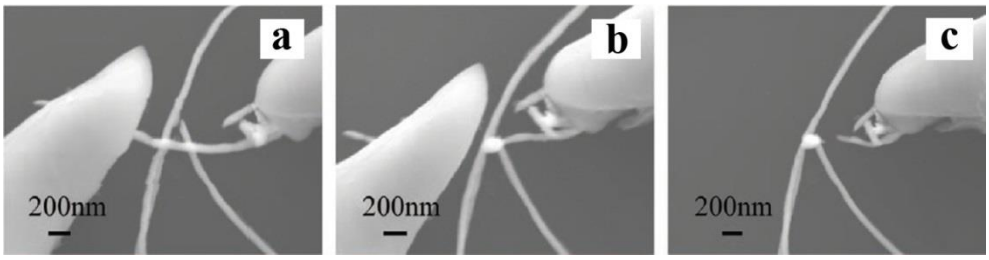

Fig.1-7, Nanosoldering 55 nm Au nanowires. (a) Softening of the solder nanowire and contact to the two Au nanowires to be welded; (b) Nanosoldering two nanowires together by a rectangular voltage pulse through the solder nanowire; (c) Mechanical removal of the solder nanowire, leaving miniaturized Chinese character. The figure is adapted from ref. [32].

Beside the physical methods mentioned above, laser nanojoining is also attracting great attention. For instance, Kim *et al*. [30] welded Au NPs in a diluted aqueous solution (9.3 nM) using a picosecond (ps) Nd:YAG laser. Liu *et al.* [31] achieved the brazing of Pt-Ag NPs by utilizing femtosecond (fs) laser irradiation. However the final joined structures obtained in these works were uncontrolled due to the random motion of the NPs in the aqueous solution. To obtain controllability, Mafun é *et al.* [41] selectively melted Pt

NPs by exciting their LSP resonance, and then soldered other un-melted Au NPs in the aqueous solution. Although there have been few further reports in this area, the idea of joining nanomaterial by controlling the LSP was developed. To completely eliminate the influence of the random motion of the nanomaterials in aqueous solution, nanomaterials are usually deposited on a substrate and then joined by laser radiation [29]. In that case, the final joined structure is determined by the deposition process.

In summary, in nanojoining processes, the balance between control of joined structure, damage to pre-joined nanomaterial and joining efficiency has to be achieved.

1.3 Research motivation and objectives

Fs laser possesses high intensity but causes small thermal damage; this makes it an ideal tool for precise fabrication of nanomaterials which are very sensitive to thermal effects. In addition, the high intensity of fs laser will produce strong plasmonic effects (arising from LSP) and facilitate the joining of nanomaterial by producing localized heating, near-field ablation and optical force. So, the combination of fs laser radiation and LSP-dependent plasmonic effects shows promising potential for the application in joining nanomaterial.

The goal of the present study is to explore an alternative LSP-assisted fs laser nanojoining technique to join/assemble nanomaterial building blocks in a non-destructive, efficient, and controllable way, which promises large scale production of micron/nanodevices. While the overall focus is on obtaining a fundamental understanding of fs laser nanojoining technique, the joining of larger (submicron scale) components is also considered because of the many applications of these elements in micron/nanodevices. Here, Ag submicron/nanomaterial is

chosen for this study because of its excellent plasmonic properties, and a program of experimental and theoretical work is carried out to accomplish the following:

1. Study the feasibility and mechanism of fs laser nanojoining of Ag nanomaterial in a controllable way (including control of the joined structure and laser radiation induced damage).

2. Investigate the influence of operation environment (aqueous solution, air, and vacuum) on fs laser nanojoining.

3. Identify the contribution of LSP in fs laser nanojoining processes.

1.4 Thesis organization

This thesis is organized as follows: Chapter 1 introduces nanomaterial and the development of nanojoining techniques. Chapter 2 revisits the fundamentals and experimental work of fs laser fabrication, and presents the background of LSP and its contribution to fs laser fabrication. Chapter 3 describes the fs laser system and experimental setup in this study. Chapter 4 presents the results and discussions of controlled joining of PVP coated Ag NPs in aqueous solution by fs laser irradiation. Chapter 5 explores the joining of PVP coated Ag NPs in air and vacuum based on the results of chapter 4, and compares it with the joining of bare Ag NPs in vacuum. Chapter 6 investigates the assisting effect of oxygen on the joining of bare Ag submicron/nanoparticles. Chapter 7 summarizes the work of fs laser nanojoining in chapters 4-6 and comes to some conclusions; while future work is also suggested.

Chapter 2 Literature review

2.1 Femtosecond laser

Laser is the acronym for "light amplification by stimulated emission of radiation", which is a device that produces monochromatic, coherent, and highly collimated beams of light. The schematic of the laser mechanism in a three-energy level system is shown in Fig.2-1. In this system, electrons at energy level E1 are first pumped (or excited) to energy level E3, and then they quickly decay to metastable energy level E2, releasing energy in form of heat. When the number of the electrons at E2 is much larger than that at E1, population inversion happens, and electrons at E2 decay to E1, emitting coherent light. According to the energy distribution over time, lasers can be divided into two types: continuous wave (CW) lasers whose output energy is constant over time, and pulsed lasers.

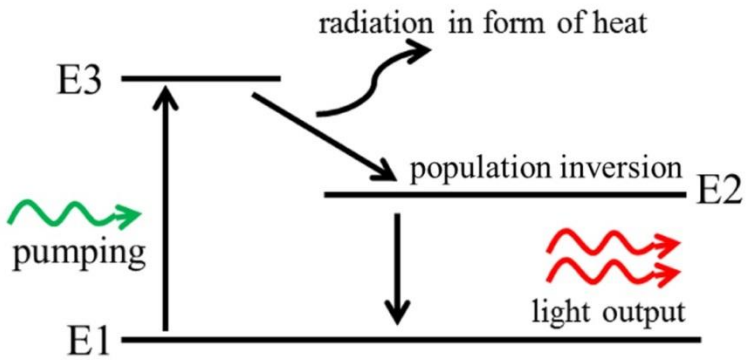

Fig.2-1, Schematic for light amplification by stimulated emission of radiation in a three energy levels (E1, E2 and E3) system

The fs laser is a pulsed laser with pulse duration ≤ 100 fs (10^{-13} s). Based on the selection of the gain medium in the laser, fs lasers can be divided into fs dye lasers where the dye is typically organic molecules in liquid solution, and fs solid-state lasers. More details about the fs laser, such as how it works, are presented in chapter 3. The fs laser, because of its ultrashort pulse duration, can achieve a very high intensity with a small pulse energy. This

makes fs laser radiation able to minimize its thermal effect, and promises many applications in precise material removal such as cutting and drilling. Recently, the fs laser has also shown the potential of joining nanomaterials. As Hu *et al*. reported [42], Au NPs have been joined by fs laser irradiation at intensity of ~10^{10} W/cm^2 without causing massive destruction of the NPs, which benefited from the limited thermal effect of fs laser radiation in its interaction with the irradiated material.

2.1.1 Fundamentals of fs laser-matter interaction

In the laser-matter interaction, the primary process is the excitation of electrons from their equilibrium states to some excited states by the absorption of photon energy through electron-photon coupling in the skin layer. This process happens roughly on a time scale of ~ 10^{-14} s. According to the definition of non-thermal and thermal processes, as shown in Fig.2-2 [43], the electron-photon coupling process is non-thermal.

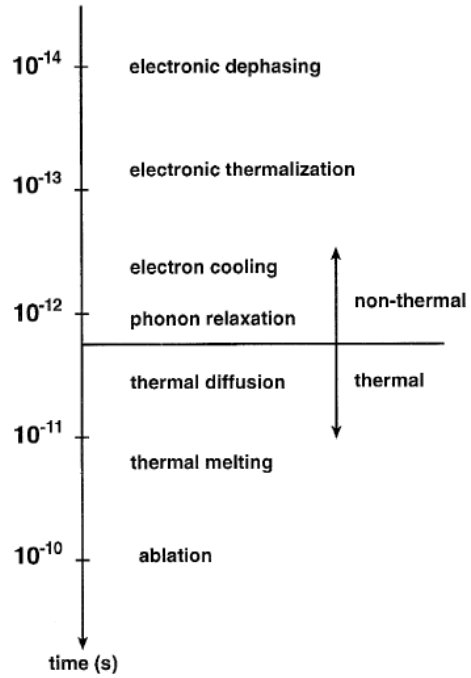

Fig.2-2, Time scale for various secondary processes after the primary electron excitation with laser radiation. This figure is adapted from ref. [43].

For the fs laser, because its pulse duration is less than 100 fs, the laser-material interaction in the pulse duration is non-thermal. After the pulse, thermal relaxation of the excited electrons through electron-phonon coupling happens in ~ 1 picosecond (ps, 10^{-12} s), followed by thermal diffusion via phonon-phonon coupling [43]. This distinguishes fs laser from conventional longer pulse (> 1 ps) lasers where both thermal relaxation of electrons and thermal diffusion take place during the pulse duration. In order to precisely describe fs laser-matter interaction, a two-temperature model is developed. Fig.2-3 shows a schematic for a 1D two-temperature model describing the fs laser-matter interaction process.

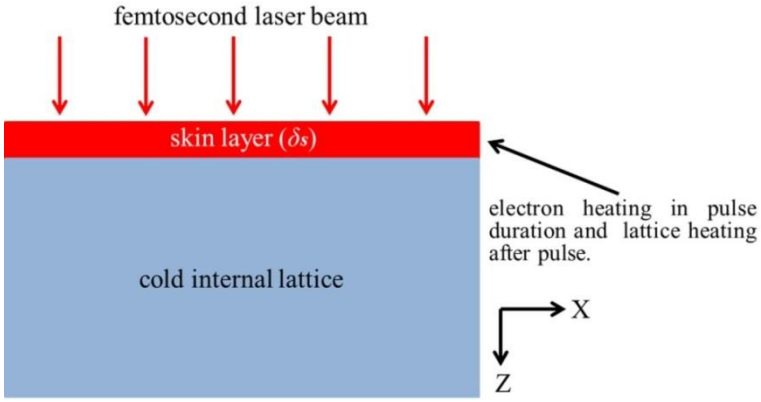

Fig.2-3, Schematic of two-temperature model for fs laser heating

In the two-temperature model [44], two equations (eqn.(2-1) and eqn.(2-2)) involve electron temperature (T_e) and lattice temperature (T_l) are written as below to describe the heating of electrons and lattice on different time scales in the skin layer (δ_s).

$$C_e \frac{\partial T_e}{\partial t} = k_e \frac{\eth T_e}{\eth Z} - \gamma[T_e - T_l] + S(Z,t), \quad (2\text{-}1)$$

$$C_l \frac{\partial T_l}{\partial t} = \gamma[T_e - T_l], \quad (2\text{-}2)$$

where C_e, C_l is the electron and lattice heat capacity (J • K^{-1} • m^{-2}), respectively; γ is the electron-lattice interaction factor (or electron-phonon coupling strength, W • K^{-1} • m^{-2}), k_e

is the electron thermal conductivity (W • K^{-1} • m^{-1}), and *S* represents the laser source term (W • m^{-2}). To understand these two equations, three characteristic times which include electron cooling time (τ_e), lattice heating time (τ_l), and laser pulse duration (τ_L) have to be considered. If $\tau_L << \tau_e$ ~10 ps, electron-phonon coupling is negligible in the laser pulse duration, or $\gamma \approx 0$. Then, eqn.(2-1) and eqn.(2-2) can be reduced to:

$$C_e \frac{\partial T_e}{\partial t} = k_e \frac{\eth T_e}{\eth Z} + S(Z,t) \, . \qquad (2\text{-}3)$$

Eqn.(2-3) shows that, in the laser radiation process, the lattice is cold when the electrons are heated up by photons. This is the case for the fs laser irradiation process.

If $\tau_L >> \tau_e$ ~10 ps, the electron and lattice have reached equilibrium in the pulse duration, which means $T_e = T_l$. Then, eqn.(2-1) and eqn.(2-2) is reduced to:

$$C_l \frac{\partial T_l}{\partial t} = k_l \frac{\eth T_l}{\eth Z} + S(Z,t) \, , \qquad (2\text{-}4)$$

where k_l is lattice thermal conductivity (in W • K^{-1} • m^{-1}). This case applies for nanosecond (ns), millisecond (ms) and most ps lasers.

It is noted in Fig.2-3 that, the two-temperature model is only used to describe the electron and lattice temperature condition in the skin layer of the irradiated target whose thickness is twice the optical penetration depth δ_p. The optical penetration depth δ_p is the depth at which the laser intensity inside the irradiated material falls to *1/e* of its original intensity, and it can be written as:

$$\delta_p = \frac{1}{\beta} \, , \qquad (2\text{-}5)$$

where $\beta = \frac{4\pi K}{\lambda}$ is the attenuation constant (or the absorption coefficient, m^{-1}). Here, λ is the wavelength of the laser, *K* is the imaginary part of the complex refractive index. Take

for instance a silver (Ag) slab which is irradiated by fs laser with wavelength of 800 nm as an example, K=5.29 [45] , so the thickness of the skin layer is $\delta_s=2\delta_p$=22 nm. The material beneath the skin layer may also be influenced by laser radiation. This depends on the thermal diffusion length in the laser pulse duration. The calculation of thermal diffusion length can be written:

$$L_{\text{diff}} = 2\sqrt{D\tau_L}\,, \tag{2-6}$$

where D is the thermal diffusivity (in unit of $m^2 \cdot s^{-1}$) and τ_L is the pulse duration as mentioned above. Take an Ag slab as an example, under ps laser (10 ps) and ns laser (10 ns) irradiation, the diffusion lengths are 80 nm and 2.6 μm, respectively. These values are close to or much larger than the size of Ag nanomaterial, suggesting that the irradiated Ag nanomaterials are almost in thermal equilibrium in exposure by ps or longer pulse duration lasers. While for laser (100 fs) radiation, even if considering the thermal diffusion (this is not the fact for fs laser radiation as discussed above), take D= 1.66 x 10^{-4} m^2/s [46], the diffusion length in 100 fs duration is only 8 nm. This indicates that compared to ps or longer pulse lasers, fs laser radiation is much more suitable for localized fabrication of nanomaterials. However it is noted that the excitation of LSP in plasmonic nanomaterials such as Ag, Au, and copper (Cu), will affect the electric field distribution (or direct the laser intensity distribution) in the nanomaterials in the fs laser irradiation process. This will bring some complexity to analyzing fs laser irradiated plasmonic nanomaterials.

2.1.2 Non-thermal and thermal phenomena in fs laser fabrication process

According to fs laser-matter interaction as discussed in section 2.1.1, the fs laser fabrication process can be divided into two stages: pre-thermal stage in the pulse duration and thermal

stage after the pulse. Below are some non-thermal and thermal phenomena which have been observed in these two stages.

2.1.2.1 Non-thermal phenomena

In the pre-thermal stage, two significant phenomena are the Coulomb explosion and field ion emission. Fig.2-4 shows the schematic for coulomb explosion of one cluster [47]. Under fs laser irradiation, electrons are excited and leave the clusters; with the increase of irradiation time, more electrons leave the cluster, and the screening effect of the electrons on the positively charged atomic cores become weaker. Then the positively charged atomic cores repel each other, resulting in the explosion of the cluster. It is noted that a Coulomb explosion usually takes place in dielectric materials, molecules and clusters.

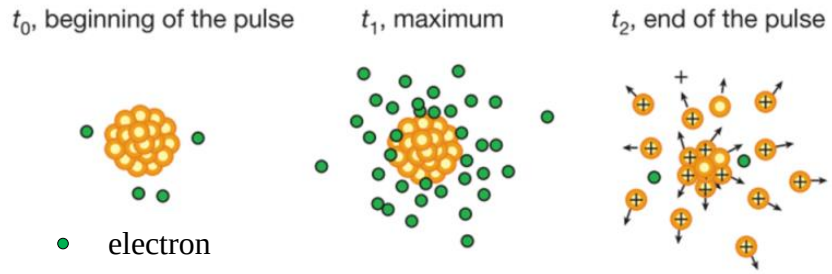

Fig.2-4, Schematic for Coulomb explosion in fs laser radiation process. The figure is adapted from ref. [47].

Fig.2-5 shows the schematic for fs laser-induced field ion emission. At the beginning, some electrons are excited out from the surface of fs laser irradiated material (Fig.2-5a). Then, an electrostatic field is built up between the excited electrons and the irradiated surface which is positively charged (Fig.2-5b). If this field together with the electric field of the incident light is strong enough, the positively charged ions in the irradiated surface will be pulled out, resulting in ion emission (Fig.2-5c).

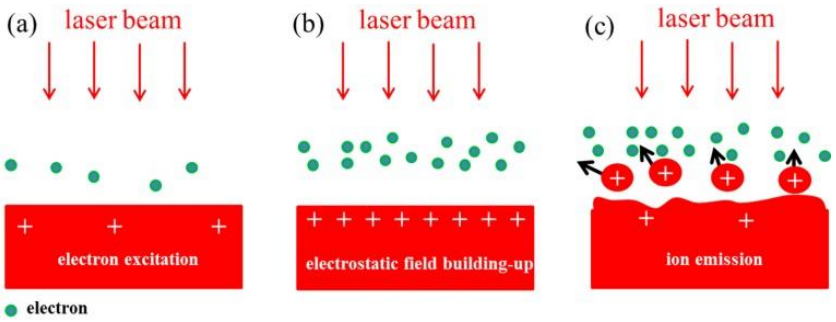

Fig.2-5, Schematic for fs laser induced field ion emission

2.1.2.2 Thermal phenomena

After Coulomb explosion and ion emission process in the pre-thermal stage, part of the excited electrons and emitted ions will recombine on the surface of the irradiated material, and transfer their energy into the irradiated material. Meanwhile, the electrons in the excited state will decay to equilibrium state. Both of these processes result in the thermal heating in fs laser irradiated material. As can be seen in Fig.2-6a, when fs laser with low pulse energy (130 nJ) was focused (the spot size was 6 μm) on an Au nanofilm (60 nm thickness) which was coated on the surface of quartz glass, some bumps in the film were generated in the irradiation area. When the fs laser pulse energy increased to 155 nJ (Fig.2-6b), a nanodroplet was generated in the center of the bump and tended to be ejected out of the film. The nanodroplet was then ejected out of the film, leaving a bulge in the film, when the fs laser pulse energy was further increased to 170 nJ (Fig.2-6c). The formation dynamic of this ejected droplet is described in Fig.2-6d. The Au film is quickly heated up by fs laser pulses, while the quartz substrate is almost cold due to its low thermal conductivity. Then the irradiated Au film tends to expand, but this expansion is constrained by the cold glass and the un-irradiated Au film, resulting in mechanical instability. Due to the low adhesion between Au and the glass substrate, the irradiated film detaches from the substrate and forms a protrusion. If the laser intensity is high, a spherical nanodroplet is

formed at the tip of the protrusion due to large surface tension, and the nanodroplet is then ejected out of the heated film because of Plateau-Rayleigh instability [48].

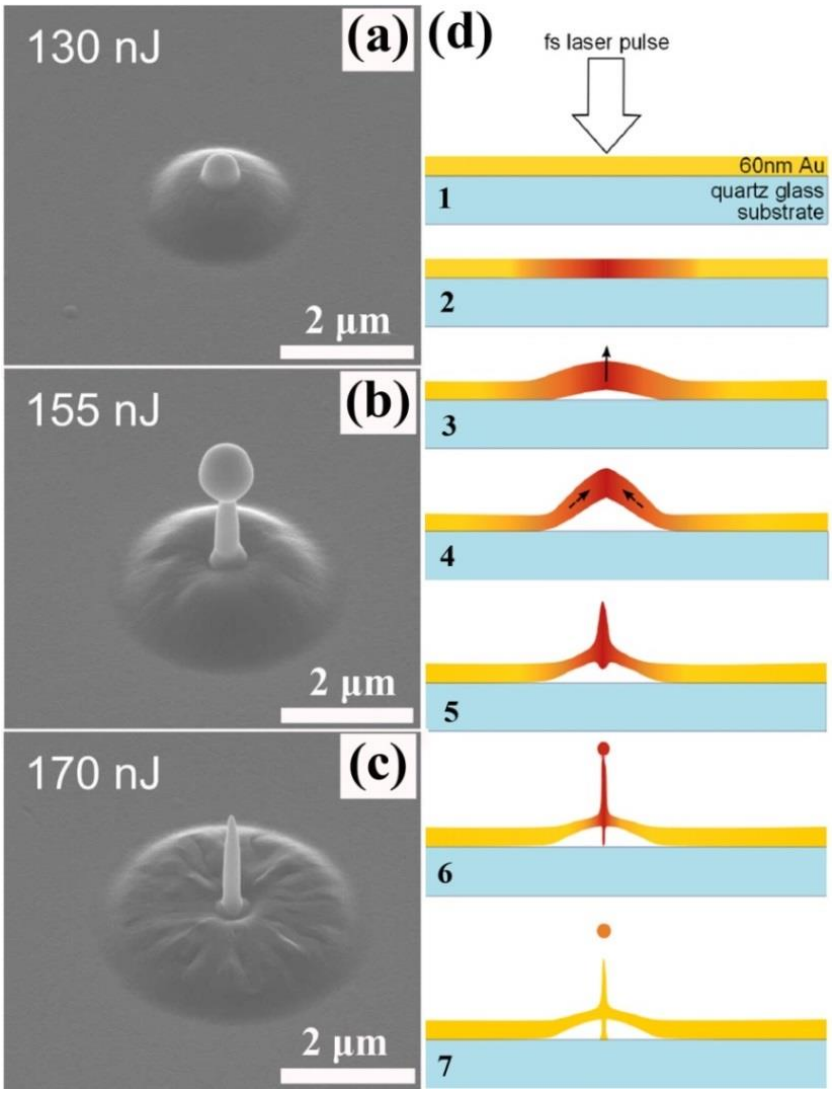

Fig.2-6, SEM images of the morphology for 60 nm thickness Au nanofilm on quartz glass substrate which were irradiated by fs laser with different pulse energies, the focus diameter of the beam is 6 µm. (a) 130 nJ, (b) 155 nJ, (c) 170 nJ, (d) Formation schematic of the nanodroplet. The figure is adapted from ref. [48]

The above discussion indicates that fs laser radiation will produce thermal heating after the pulse. This thermal effect is expected to be much smaller than that caused by longer pulse (ps, ns and ms) or CW lasers, if the same laser intensity is applied in the same area, because of lower energy input. This unique characteristic of producing limited thermal effect can be defined as the "non-thermal" characteristic of fs laser radiation.

2.1.3 Interaction of fs laser with nanomaterials

2.1.3.1 Extinction of fs laser radiation in nanomaterials

Compared to bulk material, the interaction of nanomaterials with fs laser radiation is much different, especially in the extinction of the incident laser energy. The extinction of fs laser radiation is comprised of two components: scattering and absorption.

For materials with different sizes, the scattering behaviors are different. This depends on the ratio of particle size (spherical particle) to laser wavelength:

$$A = \frac{2\pi r}{\lambda}, \tag{2-7}$$

where r (in unit of m) is the radius of the particle, λ is the wavelength of the incident laser (in unit of m). When $A > 1$, the scattering behavior of the particle is called Mie scattering; while Rayleigh scattering applies to the case of $A << 1$. The schematic for the particles' scattering behaviors is shown in Fig.2-7.

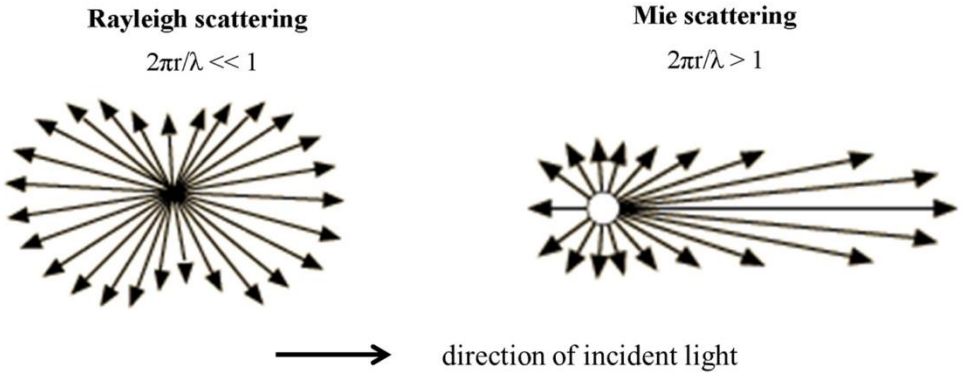

Fig.2-7, Schematic for particles' scattering behavior. This figure is modified from ref.[49].

For NPs, Rayleigh scattering dominates the scattering of incident laser. The extinction cross-section (σ_{ext}) is written as:

$$\sigma_{ext} = \sigma_{sca} + \sigma_{abs}, \tag{2-8}$$

where σ_{sca} and σ_{abs} are scattering and absorption cross-sections (in unit of m^2), respectively. The scattering cross-section is calculated via eqn.(2-9):

$$\sigma_{sca} = \frac{2\lambda^2}{3\pi}\left(\frac{2\pi r}{\lambda}\right)^6 \left|\frac{m^2-1}{m^2+2}\right|^2 , \quad (2\text{-}9)$$

where $m = n'\text{-}Ki$ is the complex refractive index and n' is the real part of the refractive index that control the refraction of light. The imaginary part is related to the absorption of light. The absorption cross-section σ_{abs} is calculated via eqn.(2-10):

$$\sigma_{abs} = -\frac{\lambda^2}{\pi}\left(\frac{2\pi r}{\lambda}\right)^3 I_m\left(\frac{m^2-1}{m^2+2}\right). \quad (2\text{-}10)$$

It is obvious that, for a dielectric particle (K=0), the contribution of absorption is identically zero, which means $\sigma_{ext} = \sigma_{sca}$. For an absorbing particle ($K \neq 0$), the contribution of scattering to the total extinction cross-section is negligible compared to absorption, so it is usually assumed that $\sigma_{ext} = \sigma_{abs}$.

Take 50 nm Ag NP as an example, $\sigma_{abs} = 7.5\text{x}10^{-18}$ m^2 when the NP is irradiated by 800 nm light. This cross-section can be smaller or larger than the geometrical cross-section (A^*) of Ag NPs. The ratio between the absorption cross-section and the geometrical cross-section is defined as the absorption efficiency (Q_{abs}) of the Ag NP. It can be written as:

$$\sigma_{abs} = Q_{abs}A^* . \quad (2\text{-}11)$$

For the case of 50 nm Ag NP which is irradiated by light with wavelength of 800 nm, σ_{abs} is much smaller than A^*, resulting in $Q_{abs} = 0.0038$.

2.1.3.2 Femtosecond laser radiation induced optical force

Optical force is the force exerted on the objects which are irradiated by light. It can be divided into two components, one is the scattering force and the other is the gradient force.

Scattering force points along the propagation direction of the incident light, it is expressed as [50]:

$$F_{scat} = n_m \frac{\langle S \rangle \sigma_{sca}}{c}, \qquad (2\text{-}12)$$

where n_m is the refractive index of the surrounding medium ‹*S*› is the time-averaged Poynting vector (which represents the directional energy flux density of an electromagnetic field in unit of W • m^{-2}), c = 3x10^8 m/s is the speed of light, σ_{sca} is the scattering cross-section of a Rayleigh sphere particle as calculated in eqn.(2-9).

Gradient force is the Lorentz force acting on the dipole which is induced by the optical electric field (E, V/m). It is proportional to the energy density gradient, and its direction is parallel to that of the energy density gradient. This force is given as [50]

$$F_{grad} = \frac{\alpha}{2} \nabla \langle E^2 \rangle, \qquad (2\text{-}13)$$

where α is the polarizability of the particle (in unit of m^3). Fig.2-8 shows the optical forces in laser irradiation process.

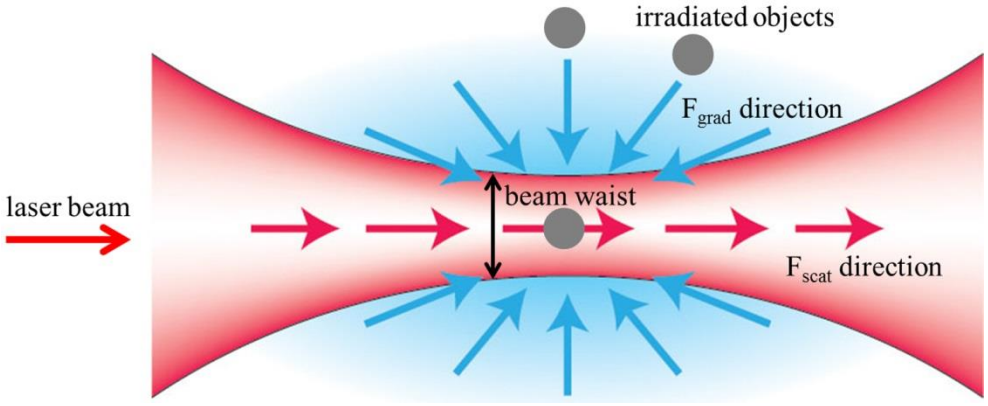

Fig.2-8, Schematic for optical forces in laser irradiation process. The figure is Modified from ref. [51]

2.2 Surface plasmon

In metallic material, when the free electrons in the metal are displaced from the atomic cores by the external electric field, the positively charged atomic cores will exert a

restoring force and pull the electrons back to their original positions. This collective oscillation of electrons in the metal is plasmon and it occurs at the plasma frequency [52]:

$$\omega_p = \sqrt{\frac{n_0 e^2}{\varepsilon_o m_0}}, \qquad (2\text{-}14)$$

where n_0 is the conduction electrons density, e = 1.6x10^{-19} C is the electron charge, ε_0 = 8.85x10^{-12} F • m^{-1} is the permittivity of the vacuum, and m_0 is the effective electron mass (in unit of kg). Surface plasmons are then defined as the plasmon which is confined near the surface of the metal. The schematic for the spatial distribution of a surface plasmon which is excited at the dielectric-metal surface is shown in Fig.2-9 [53].

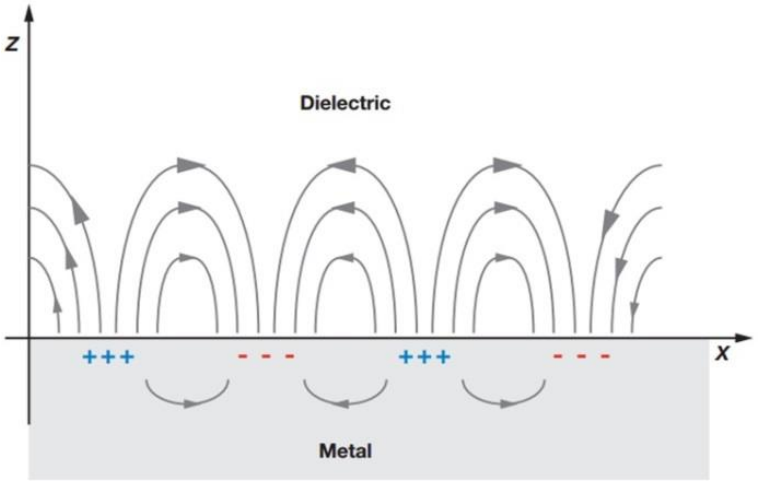

Fig.2-9, Schematic for the excitation of surface plasmon at the dielectric-metal interface. The arrows show the electric field direction. The figure is adapted from ref. [53] .

The boundary condition for the excitation of surface plasmon is that the component of the electric and magnetic fields must be continuous at the interface. This can be written mathematically as [54]:

$$\frac{\varepsilon_1}{k_1^*} + \frac{\varepsilon_2}{k_2^*} = 0, \qquad (2\text{-}15)$$

where ε_1 is the dielectric function of metal, ε_2 is the dielectric function of the dielectric material, k_1^* and k_2^* are the wave numbers (in unit of m^{-1}) of the electromagnetic waves in the metal and dielectric material, respectively.

The condition for the excitation of surface plasmon of metal sphere is [54]:

$$l\varepsilon_1 + (l+1)\varepsilon_2 = 0,\ l=1, 2, \ldots, \quad (2\text{-}16)$$

where l is the mode number of surface plasmon. For the case of a Drude metal sphere (which is a sphere consisting of metallic ions with fixed position and free valence electrons) in vacuum, the frequency of surface plasmon (ω_l) can be written as [54]:

$$\omega_l = \omega_p\sqrt{\frac{l}{2l+1}}. \quad (2\text{-}17)$$

For spherical NP, it can be completely polarized by the light and forms a dipole, and the electric field inside the NP becomes uniform. The surface plasmon mode in the NP is the simplest dipolar mode, which means l=1 in eqn.(2-16). Then the frequency of the localized surface plasmon (ω_{LSP}) in the spherical NP is:

$$\omega_{LSP} = \omega_p/\sqrt{3}. \quad (2\text{-}18)$$

It is noted that the above equations of calculating the surface plasmon are only for estimation of the surface plasmon frequencies under ideal condition. For some noble metals (e.g. Au, Ag, Cu), the electric interband transition have also to be considered, extensive discussions about surface plasmon can be found in ref.[54].

2.2.1 Material and geometry dependent surface plasmon property

Usually, surface plasmon only exists in metallic materials which have free electrons, such as Ag, Au, Cu, and Al. In some semiconductor materials such as Si and carbon nanotube (CNT), surface plasmon is also reported [55, 56]. As shown in Fig.2-10 [57], the

wavelength of the surface plasmon in different metallic NPs ranges from approximately 200 nm to 650 nm. Among these materials, Ag NPs with size of 10 nm show much better surface plasmon property which is reflected in the much higher extinction cross-section (4080 nm^2) at the resonant wavelength, compared to other metallic NPs of the same size.

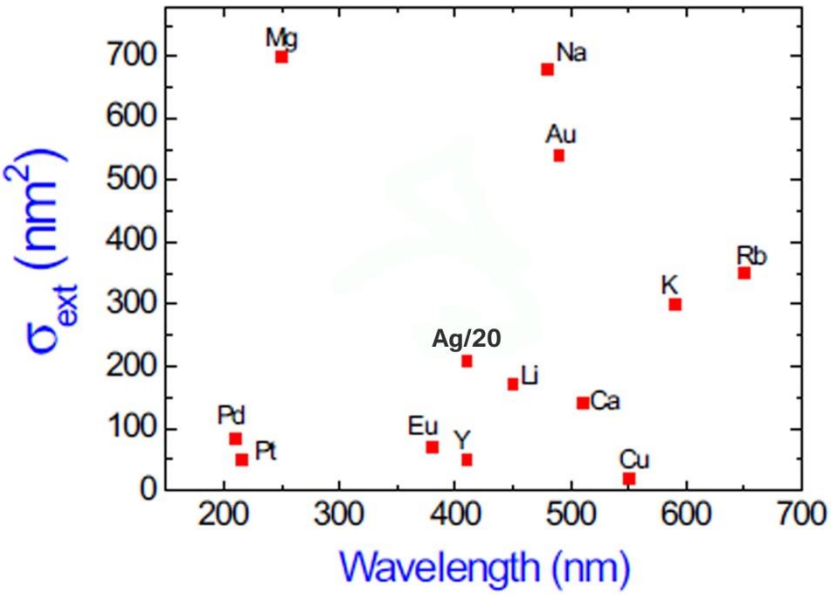

Fig.2-10, Resonance wavelength and extinction cross section for metallic NPs with 10 nm size in air. The extinction cross-section of Ag has been divided by 20 for a better presentation (the real value is 4080 nm^2). The figure is adapted from ref. [57].

Fig.2-10 also shows that the wavelength of surface plasmon presented here is only for 10 nm spherical particles. By varying the size and shape of the nanomaterial, the wavelength of surface plasmon can be changed. Fig.2-11a shows the UV and visible (UV-VIS) absorbance spectra of Ag NPs with different particle sizes in the aqueous solution [58], in these spectra the location of the absorption band corresponds to the resonance wavelength [59]. It can be seen that with the decrease of the particle size, the resonance wavelength shifted to shorter-wavelength side (blue shift). It should be noted that resonance wavelength shift is also highly affected by the matrix where the NPs are

embedded. As shown in Fig.2-11b, when the resonance wavelength of the bare Ag NP was measured in inert He gas, it shifted to longer-wavelength side (red shift) with the decrease of particle size (~20-100 nm) [60].

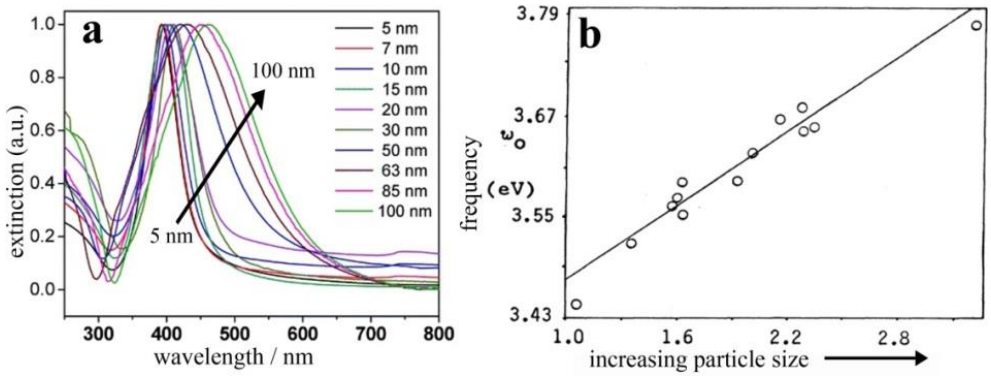

Fig.2-11, Dependence of resonance wavelength (or frequency which is inversely proportional to the wavelength) on particle size. (a) resonance wavelength of Ag NPs in aqueous solution; (b) resonance frequency of Ag NPs in He gas. Figures a and b are adapted from ref. [58] and ref. [60], respectively.

Beside spherical NPs, similar size-dependent surface plasmon property is also observed in nanomaterials with different shapes [61-63], e.g. nanowire, nanoprism, and nanocube. Compared to spherical NPs, nanomaterials with different shapes possess more complicated surface plasmon property due to the excitation of multipolar modes of surface plasmon [64, 65]. This is reflected in the scattering spectra of Ag nanomaterial with different shapes, as shown in Fig.2-12 where the wavelength of the scattering light is equivalent to the resonance wavelength of the surface plasmon.

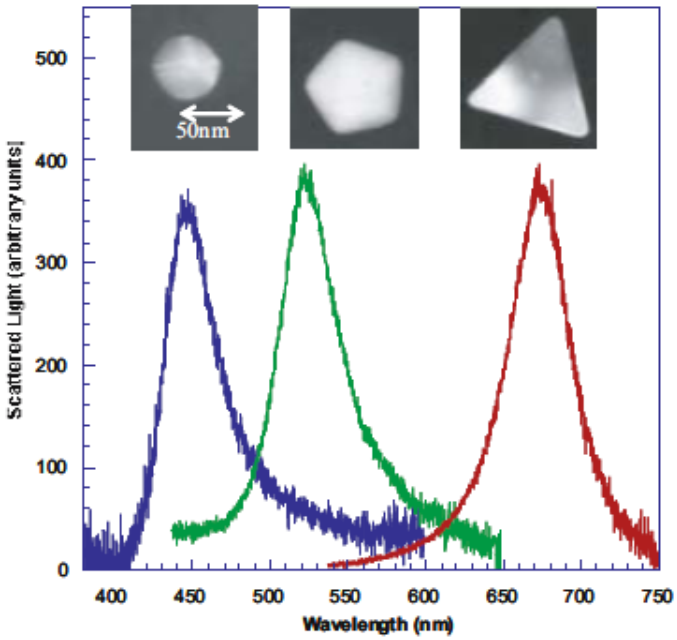

Fig.2-12, Scattering spectra for single silver nanomaterials of different shapes which were obtained in dark-field configuration. The figure is adapted from ref. [64].

2.2.2 LSP-induced electric field enhancement

LSP is known as the surface plasmon confined near the surface of the nanomaterial with size comparable to or smaller than the wavelength of light used to excite the plasmon. Fig.2-13a shows the schematic for the excitation of LSP in the nanomaterial (metallic nanosphere is taken as an example) [53]. It shows that when the nanosphere is irradiated by a polarized light, its electrons and positively charged atoms cores are separated, forming a dipole along the electric field direction of the light and resulting in a locally enhanced electric field. With the change of the electric field direction, the electrons move back and forth, forming LSP. As shown in Fig.2-13b, the electric field distribution on the surface of a 50 nm Ag NP which is irradiated by 800 nm wavelength light is always parallel to the electric field direction of the incident light, and the square field strength is enhanced by approximately 11 times (indicated by E_1^2/E_0^2, where E_1 and E_0 are the electric field of the light after and before LSP induced enhancement).

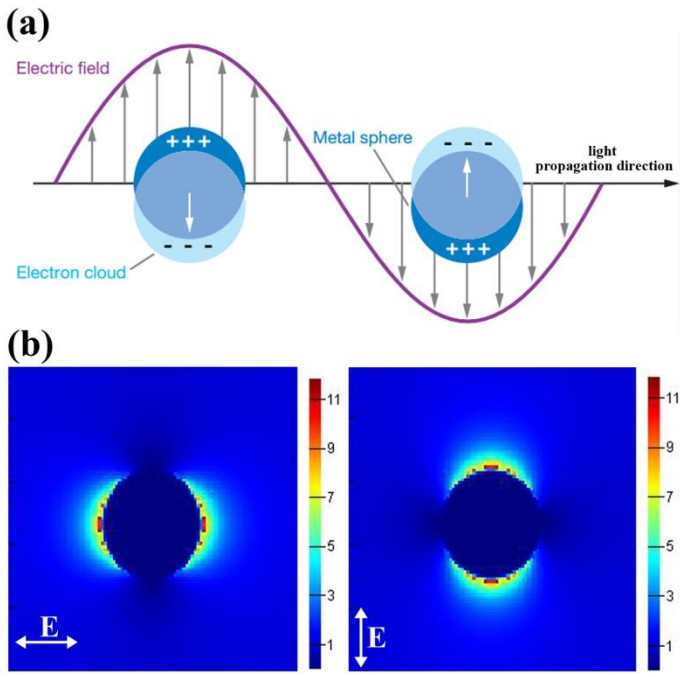

Fig.2-13, (a) Schematic for the excitation of LSP, (b) LSP induced square electric field enhancement (E^2/E_0^2) in 50 nm Ag NPs. The double-ends arrows show the electric field direction of the incident light. Figure (a) is adapted from ref. [53].

2.2.3 LSP-dependent fs laser fabrication

Since LSP can enhance the local electric field on the surface of a nanomaterial, it will favor electric field strength dependent effects such as, heating, near field ablation, optical force and dissociation. These dependences will be more significant if fs laser radiation and LSP is combined, due to the high intensity of the fs laser pulse. This facilitates the controllability of fs laser fabrication by controlling the LSP. The sections below summarize four LSP-dependent fabrication methods with fs laser radiation.

2.2.3.1 LSP-enhanced heating

The excitation of LSP enhances the local electric field near the surface of the nanomaterial. This consequently increases the absorption of laser pulse energy within enhancement region and results in improved local heating. As reported by Liu *et al.* [66], Ag NWs which were exposed to fs laser radiation at fluence approximately 110 mJ/cm^2 melted into

spherical particles from the ends of the NWs or the hotspot areas where the electric field was enhanced due to the excitation of LSP. The molten spheres then detached from the NW, and the new hotspots were generated which were located between the sphere particle and the remaining Ag NW, causing the further melting of the wire (Fig.2-14). By controlling the nanomaterial's structure and laser irradiation condition, even lower fluence fs laser pulses could cause the melting of the nanomaterials. For instance, Valev *et al.* [67] observed the ejection of molten nanojets from the hotspots in the G-shape Au nanostructure which was irradiated by fs laser at fluence > 63 mJ/cm^2 (Fig.2-15). Link's study [68] indicated that when LSP was coupled to the incident fs laser, Au NWs could be selectively melted from the ends at fluence as low as 2 mJ/cm^2. The observed LSP-dependent melting phenomena suggest that it can be used as an effective tool to join nanomaterial, because the melting of nanomaterials can accelerate the interaction between them.

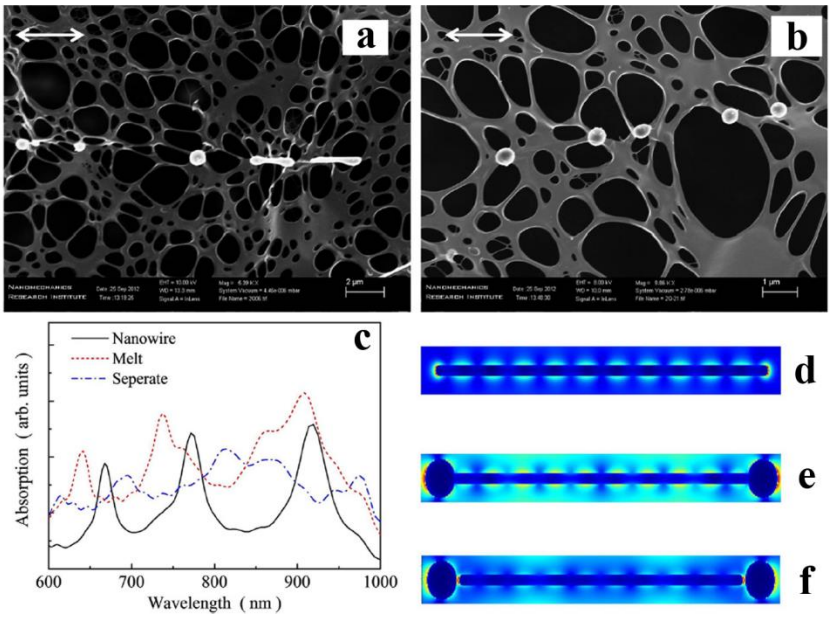

Fig.2-14, Breakdown of Ag nanowire after fs laser irradiation, Laser polarization is parallel to the long axis of the Ag NW. (a) and (b) After laser-induced melting and formation of separated NPs and nanobars; (c) Absorption spectra as calculated from FDTD simulation; (d) Electric field |E| distribution calculated by FDTD; (e) |E| distribution when the Ag NW has melted at both ends; (f) |E| distribution when particles have been separated from the ends of the NW. The arrows indicate the polarization direction. The figure is adapted from ref. [66].

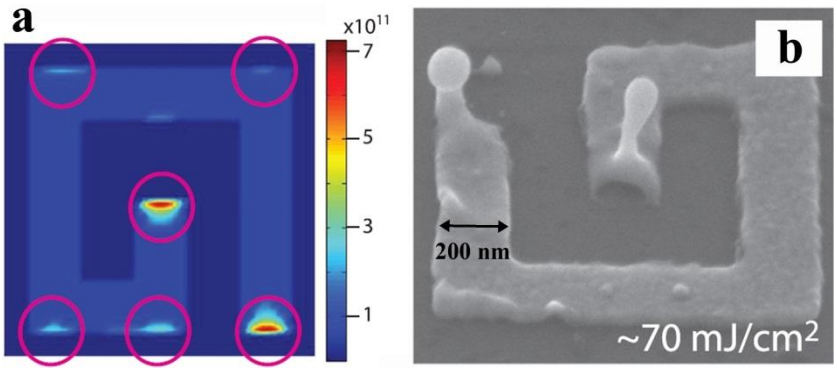

Fig.2-15, Simulated distribution of the resulting hotspots (marked as circles) in the G-shape Au plasmonic structure (a), and SEM image of the nanojet (b) in G-shaped nanostructure after irradiation by a fs laser. The figure is adapted from ref. [69].

2.2.3.2 LSP-enhanced optical trapping

As discussed in section 2.1.3.2, optical gradient force can attract nearby nanomaterials to the area where the laser intensity (or electric field) is higher. This provides a potential tool to bring nanomaterials close together to encourage joining. Excitation of LSP can enhance the electric field near the surface of nanomaterial, and then increase the electric field gradient to the surrounding medium. It suggests that LSP can be used to strengthen the optical trapping capacity of the incident laser. This is demonstrated in theoretical works. Xu *et al.* calculated the forces exerted on Ag NPs (with radius r = 45 nm) in dimer structure with gap distance of 1 nm; and the calculation indicated that the direction of the optical gradient force exerted on the NPs pointed towards the other particle in the dimer. The enhanced field between the NPs were also noticed to be able to trap the molecules nearby [70]. LSP enhanced attraction to NPs via optical gradient force is also demonstrated by experimental observations. As shown in Fig.2-16, when the polystyrene (PS) micro-bead moved close to the Au disc which was irradiated by linearly polarized laser at intensity 2.5×10^6 W/m^2, the bead was trapped by the disc due to the enhanced optical gradient force [71] from the disc. Similarly, when the Au bowtie was immersed into the Ag NPs aqueous

solution and was irradiated by a 75 μW fs laser, Ag NPs could be attracted and joined to the Au bowtie [17].

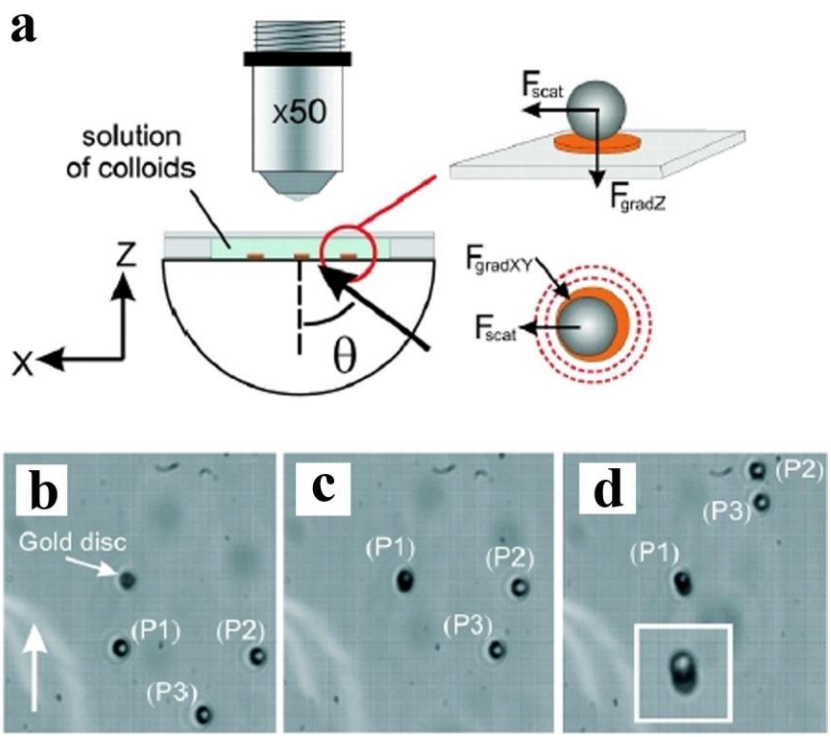

Fig.2-16, Optical trapping of PS beam by Au disc. (a) Sketch of the configuration for optical trapping; (b)–(d) Chronological frame sequence show the trapping of a 4.88 μm, PS bead at a 4.8 μm Au disc. (P1), (P2), and (P3) locate three different beads, while the vertical arrow points along the incident in-plane k vector. The incident angle θ= 68 ° and laser polarization is p polarization. A close up of the trapped bead (P1) is shown in inset of (d). The figure is adapted from ref. [71].

2.2.3.3 LSP-enhanced near field ablation

Laser ablation is usually considered to be the opposite of laser joining. However, if the location and volume of the laser induced ablation can be controlled, joining of nanomaterials could occur via the accumulation of the material which is ablated by laser radiation. This is similar to spark plasma sintering (SPS) of nanomaterials. In the SPS process [72], after the excitation of pulsed current, ions (or vaporized material) are firstly emitted from the nanomaterial, then the ions solidify in between the adjacent nanomaterials and weld them together.

Recently, it has been reported that Au NPs (as the circles in Fig.2-17 indicate) could be ablated by a 100 fs laser at very low fluence in the range of 9~15 mJ/cm^2, and the ablated material would fly out in the direction of laser polarization (Figs.2-17a, b and d). This directional ablation is attributed to ion emission under the effect of LSP-enhanced local electric field [73], facilitating the collective deposition of ablated material in between the NPs and the formation of joint. In that work, LSP-enhanced ablation was confined in the surface of the irradiated Au NPs and the main structure of the NPs was near-intact after fs laser irradiation. This suggests that LSP enhanced ablation can be used for nanojoining without causing significant damage to pre-joined nanomaterials. Fig.2-17c also shows that non-directional ablation of the Au NPs took place when the pulse duration of fs laser was stretched to 970 fs. This implies that, except longer pulse lasers, it is only feasible for fs laser radiation to achieve directional near field ablation and near-intact joining of the irradiated NPs.

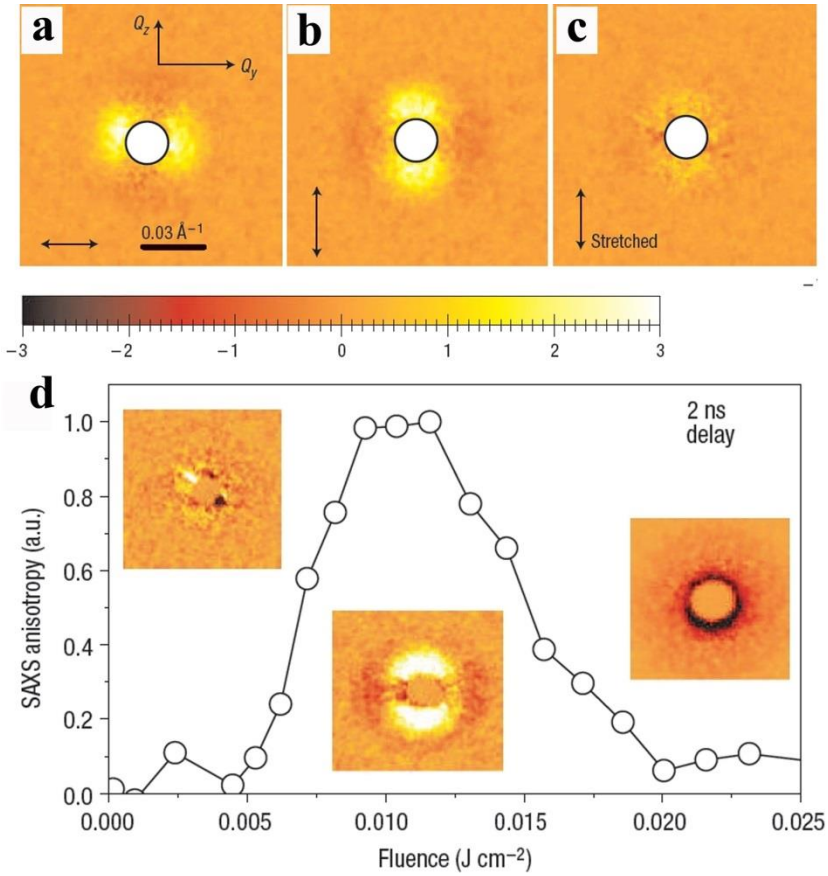

Fig.2-17, Small-angle X-ray scattering (SAXS) patterns of fs irradiated 10 nm Au NP as observed for a 1 μs delay. The x-ray beam and laser beams are propagating in the x direction. (a) 100 fs pulses of 0.0135 J/cm^2, laser polarization is horizontal, and the circle shows the position of NP; (b) the same, but laser polarization is vertical; (c) the same, but polarization is vertical and the pulse is 970 fs; (a-c) show the difference photosignal ΔS (Q_y,Q_z) on the CCD detector in a false colour plot and the central circle marks the shadowed region from the beam block. Detailed information can be found in ref. [73]; (d) the anisotropy of the SAXS patterns as a function of laser fluence as observed for a delay of 2 ns. The figure is adapted from ref. [73].

2.2.3.4 LSP enhanced dissociation

Aside from the above LSP-dependent effects, LSP can also enhance the dissociation of molecules which are adsorbed on the surface of metallic NPs. This is performed by breaking the bonds under the impact of emitted electrons/ions from the surface of the irradiated NPs. As shown in Fig.2-18 [74], plasmon excitation in Au NP causes the emission of an electron from the surface, and this electron impacts the H-H bond in the adsorbed hydrogen molecule (H_2), resulting in its dissociation and the generation of atomic hydrogen (H).

This effect is very important for joining NPs which are produced by chemical synthesis methods, since those are usually coated with polymer shell to prevent agglomeration. The dissociation of the polymer shell and the generation of dissociated product will then highly influence the joining behavior of the NPs. This should be carefully considered when polymer coated NPs are used as pre-joined nanomaterial.

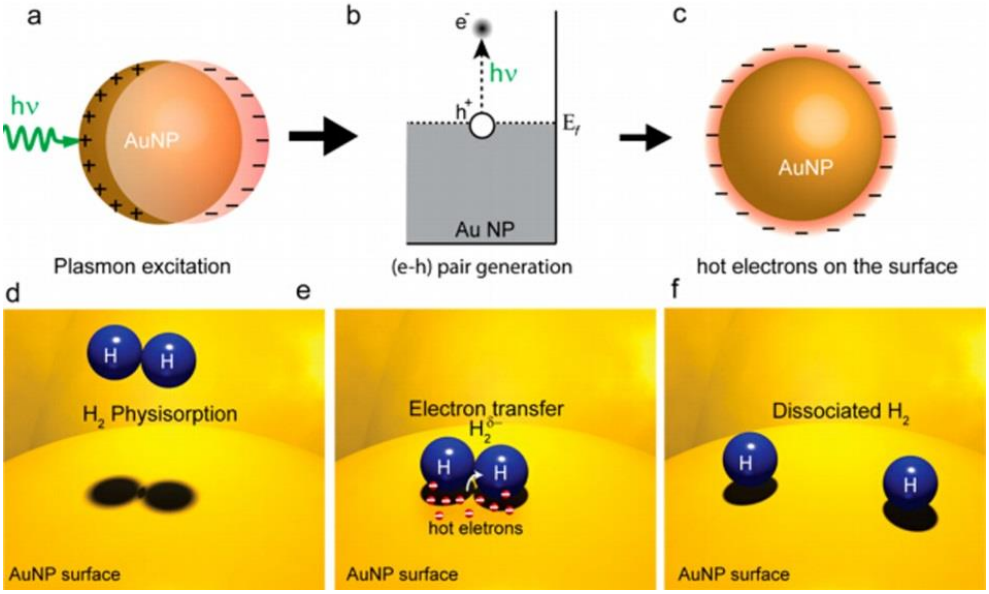

Fig.2-18, Schematics of plasmon-induced hot electron generation on Au NP and the dissociation of absorbed H_2 on the surface. (a) plasmon excitation; (b) electron-hole pair generation; (c) hot electrons on the surface; (d) H_2 Physisorption; (e) electron transfer from the surface of NP to H_2; (f) dissociated H_2. This figure is adapted from ref. [74].

Chapter 3 Equipment and Experimental Setup

3.1 Overview of experimental setup

The present study involving fs laser nanojoining includes three different processing environments (aqueous solution, air, and vacuum) by utilizing a fs laser fabrication stage. This fabrication stage consists of the fs laser system and an operation stage, as shown in Fig.3-1. The fs laser system (Legend Elite, Coherent Inc.) is left as a factory setup and kept unchanged. The factory parameters of the output laser beam are: 35 fs pulse duration, 800 nm wavelength, 1 kHz repetition and S polarization. The mode of the beam is TEM_{00} Gaussian beam with $M^2<1.3$.

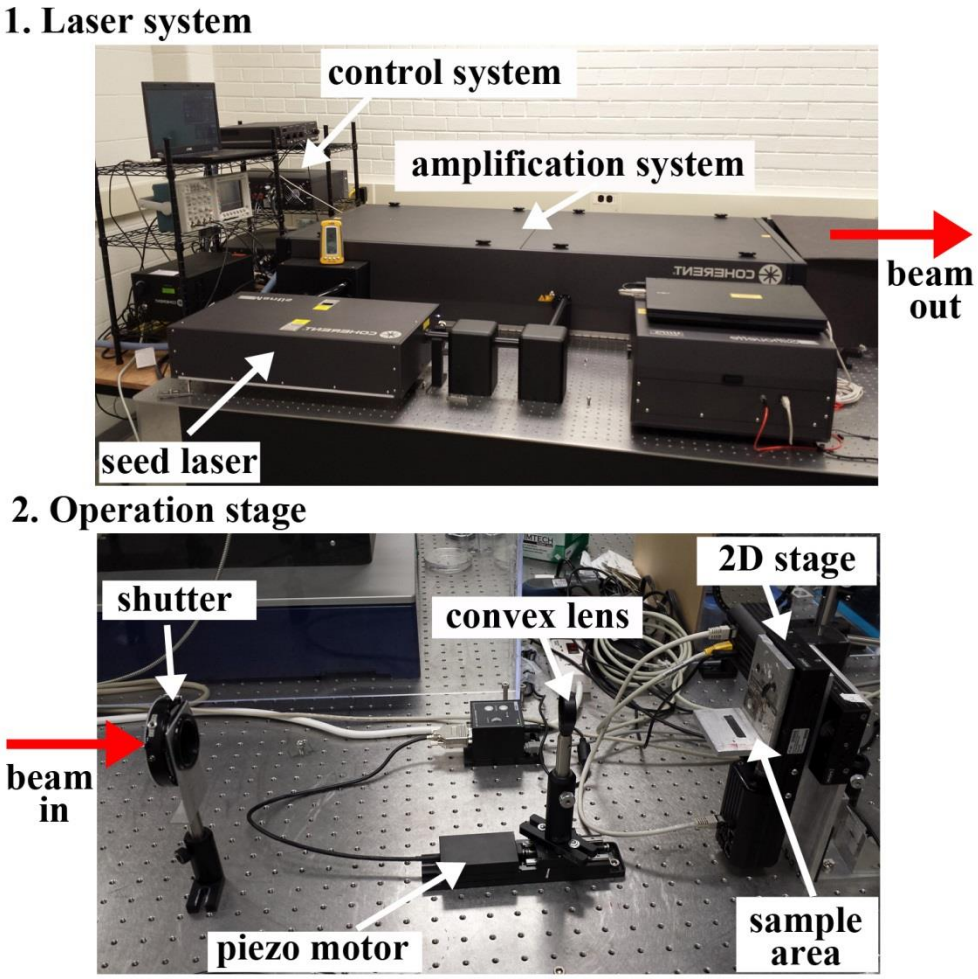

Fig.3-1, Setup of the fs laser fabrication stage which includes laser system (1) and operation stage (2).

The setup of the operation stage for the experimental research in aqueous solution and air is shown in the lower image of Fig.3-1. This stage consists of a shutter (used to control the number of laser pulses), convex lens, piezo motor (TPZ001,Thorlab Inc., used to control the spot size by controlling the distance betweem the convex lens and the sample), and a 2D stage (PI Micro Co., used to provide the support of the pre-irradiated samples and control their locations). For the experimental research in vacuum environment, a vacuum operation stage is also designed, as shown in Fig.3-2. It consists of a vacuum chamber for experimental operation, a vacuum gauge (IGM401 Hornet, Instrutech Inc.) for pressure measurement, a Turbo pump (Turbo V-551 Navigator, Agilent) which is connected to a dry mechanical pump (TS-300, Agilent), and some optical components including convex lenses and reflecting mirrors. In all the experiments, the intensity of the laser beam is adjusted by utilizing neutral density filters (Thorlabs Inc.) and the power of the laser beam is measured by a power meter (S314C, Thorlabs Inc.) with resolution of 1 mW.

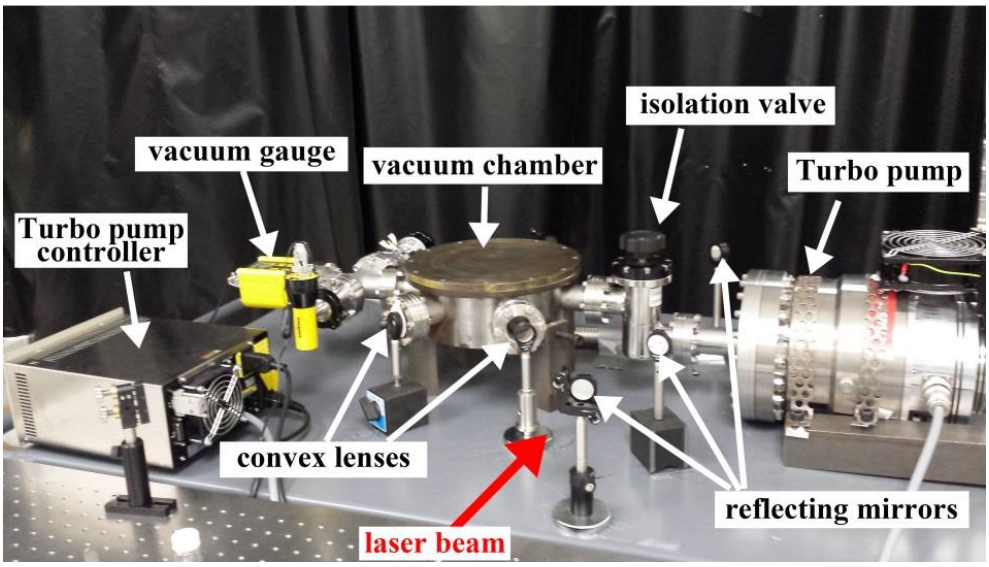

Fig.3-2, Setup of vacuum operation stage.

3.2 Femtosecond laser system

Fig.3-3 shows the schematic for the fs laser system, which consists of three main parts including seed laser, high power pump laser and amplifier. The seed laser, Mantis-5, is comprised of a pumped semiconductor laser and Titanium:sapphire ($Ti:Al_2O_3$) oscillator. When the continuous wave (CW) green light (532 nm) from the semiconductor laser shines into the $Ti:Al_2O_3$ crystal in the oscillator, a CW light with a wavelength of 800 nm is emitted. Then by employing Kerr lens mode-locking (KLM) technique and negative dispersion mirrors, fs laser pulses with 800 nm wavelength, 5 fs pulse duration, and 80 MHz repetition rate are generated.

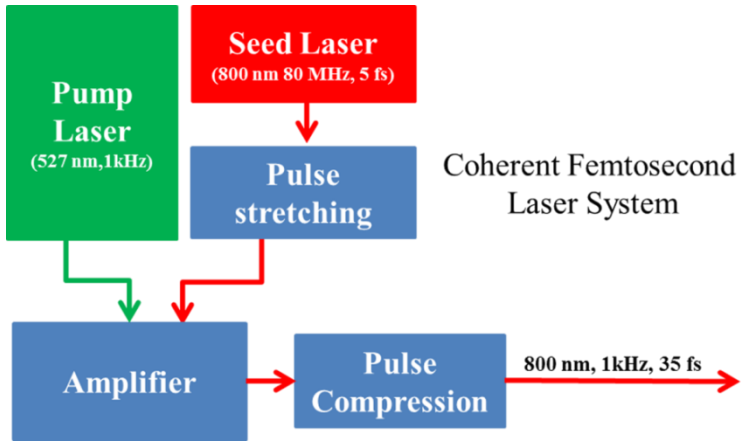

Fig.3-3, Schematic for the fs laser system (Legend Elite, Coherent Inc.).

KLM is a technique of passive mode locking a laser, using an artificial saturable absorber based on the Kerr effect. The schematic of Kerr effect is shown in Fig.3-4; it indicates that when the intensity of the light is high enough, self-focusing of the light will happen due to the change of the refraction index in the optical Kerr medium. So, when the light which consists of several modes with different intensities passes through the Kerr medium, self-focusing only happens in modes with high intensity. If an aperture is put in front of the

Kerr medium, as shown in Fig.3-4, only high intensity modes will be selected as the output light source.

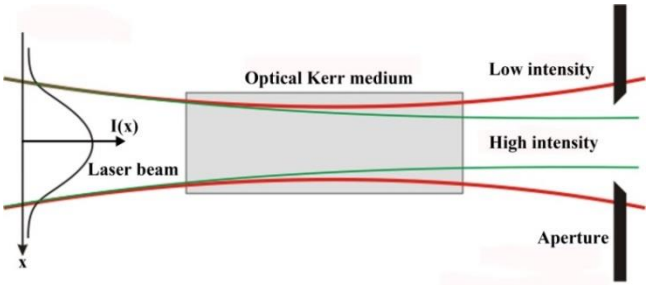

Fig.3-4, Principle of the Kerr effect.

In the Mantis system (seed laser) here, many modes exist in the emitted CW 800 nm wavelength light. By changing the length of the cavity which the Ti:Al_2O_3 crystal is located in-between, some of these modes will constructively interfere with each other, and the intensity of the mode after interference is enlarged. As shown in Fig.3-5, after mode-locking, six modes in the CW light are forced in phase and amplified, and they contribute the bandwidth of the laser pulse. Once the intensity of this pulse is sufficiently high, Kerr effect induced self-focusing happens; this pulse then becomes the dominant pulse and forms a mode-locked output.

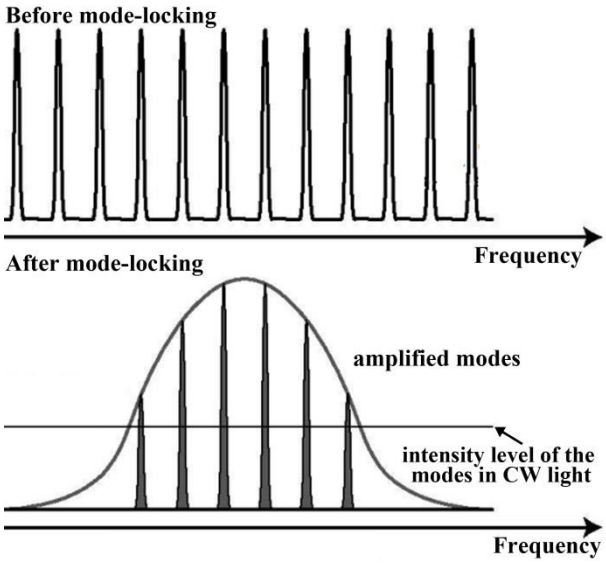

Fig.3-5, Schematic for mode-locking. This figure is modified from ref.[75].

The output of mode-locked fs laser pulses are stretched by diffraction gratings, before it goes into the amplifier, in order to avoid self-focusing induced damage to the mirrors and cavities in the amplifier. The schematic for pulse stretching is shown in Fig.3-6a. When the laser pulse passes through the diffraction grating, the short wavelength (blue) component travels a longer distance than the long wavelength (red) component. The result is that long wavelength component exits the pulse stretcher first, and the pulse is temporally stretched.

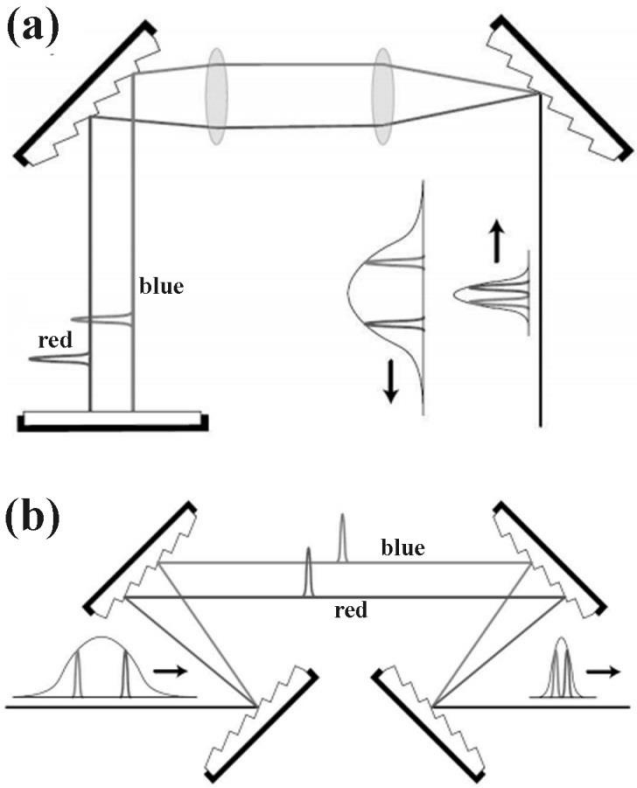

Fig.3-6, Schematic for pulse stretching (a) and pulse compression (b). This figure is modified from ref.[75].

The Q-switched high power neodymium-doped yttrium lithium fluoride (Nd:YLF) pump laser produces laser pulses with a wavelength of 532 nm and pulse duration ~ 150 ns. Its output power is 45 W and the repetition rate is 1 kHz. This high power laser then interferences with that of the seed laser in the cavity of the amplifier, and amplifies the seed laser's output. The wavelength of the output light from the amplifier is 800 nm, and

the repetition rate is 1 kHz. This output light is then compressed to a pulse duration of approximately 35 fs through the compressor which also consists of diffraction gratings; and the total average output power is ~ 7 W. In the compressor, the pulse compression process is the reverse process of pulse stretching, as shown in Fig.3-6b. Fig.3-7 shows the typical measured pulse shape and pulse duration of the output laser beam by using a Silhouette pulse shaper (Coherent Inc.); the results indicate that the central wavelength of the laser beam is 799.7 nm and the bandwidth is 25.7 nm which corresponds to a pulse duration of 33.8 fs.

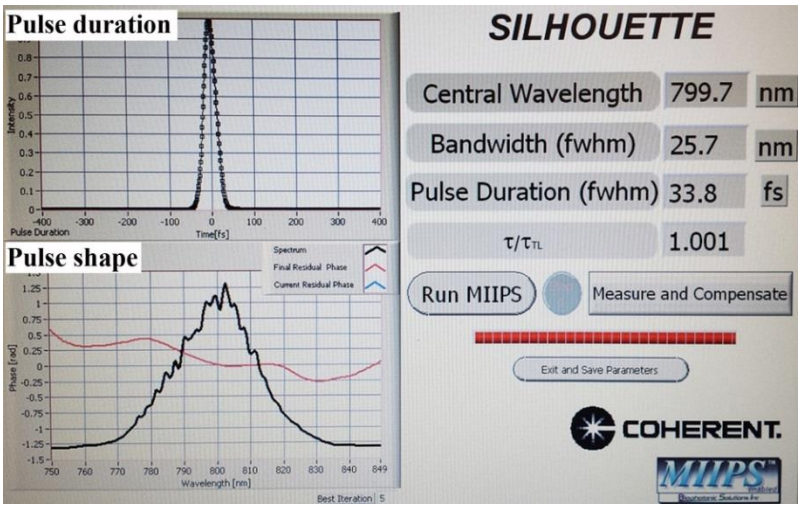

Fig.3-7, Measurement of laser pulse shape and corresponding pulse duration.

The pulse duration is measured by utilizing autocorrelation measurement technique. This technique is based on the relationship between the bandwidth and pulse duration (τ_L) which can be written as [75]:

$$\tau_L = K' \frac{{\lambda_0}^2}{\Delta\lambda \cdot c}, \qquad (3\text{-}1)$$

where K'=0.441 is known as the "time-bandwidth product" of the pulse and is a constant for a Gaussian beam, λ_0 is the central wavelength (in unit of m), $\Delta\lambda$ is the measured

bandwidth (in units of m) at full-width at half maximum (FWHM). The pulse duration of the seed laser, which is ~ 5 fs, is estimated as well by measuring the bandwidth.

3.3 Equipment for morphology and spectrum characterization

The SEM images of the morphology for the NPs in chapter 4 were taken by utilizing a SEM LEO 1550 (Watlab, University of Waterloo), and the images in other chapters were taken by a SEM LEO 1530 (Nanomechanics Research Institute, University of Waterloo). The TEM and high resolution TEM (HRTEM) images of the morphology for the Ag particles were taken by a JEOL-2010F (Canadian Centre for Electron Microscopy, McMaster University). The AFM images of the particles' morphology were taken in a near-field scanning optical microscope (NSOM) (XE-NSOM Park Systems, Centre for Advanced Materials Joining, University of Waterloo).

The optical spectra in chapters 4 and 5 were recorded by a UV-VIS-NIR spectrometer UV-2501PC (Shimadzu) with wavelength in range of 190-1100 nm, with a resolution of 0.1 nm and accuracy of $\pm$0.3 nm. The Raman spectra in chapter 4 were obtained by utilizing Raman spectrometer (RM100, Renishaw) which is equipped with reflected light microscopy and two excitation lasers of different wavelengths (488 nm and 633 nm).

3.4 Chemical synthesis of Ag NPs

Silver NPs with average size 50 nm are synthesized by a seed method where Ag NPs with size around 5-10 nm are used as seed for the growth of larger size NPs. The detailed procedures for the synthesis of seeds and large size NPs are shown below.

3.4.1 Synthesis of seed NPs

Silver nitrate ($AgNO_3$, Alfa Aesar) aqueous solution (0.5 ml, 59 mM) and 1 ml sodium citrate ($Na_3C_6H_5O_7$, Alfa Aesar) aqueous solution (34 mM) are mixed with 100 ml deionized water in a beaker, and then the beaker is put in ice water mixture to maintain the temperature at 0 ℃. The mixed solution is then stirred and 0.5 ml 20 mM sodium borohydride ($NaBH_4$, Sigma-Aldrich) aqueous solution is added drop by drop in 10 min. The color of the final seed NPs solution is bright yellow, indicating that the size of these NPs is around 5-10 nm. The morphology of the seed NPs is shown in Fig.3-8.

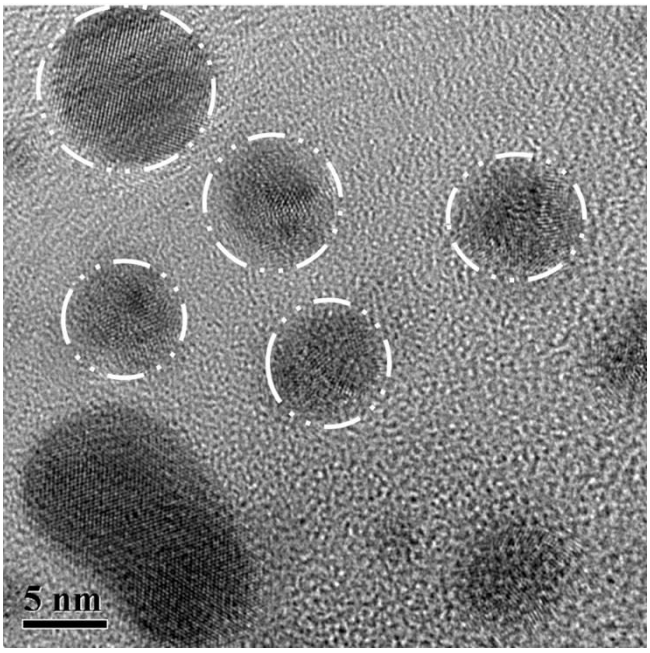

Fig.3-8, TEM image of the morphology for Ag seed NPs as indicated by the dashed rings.

3.4.2 Preparation of 50 nm Ag NPs

Ag NPs were prepared following the method reported by Peng *et al.*[29]. Sodium citrate aqueous solution (12 ml 200 mM) was added to 200 ml deionized water with vigorous stirring, followed by adding 2 ml 20 mM polyvinylpyrrolidone (PVP, $(C_6H_9NO)_n$, K25 with molecular weight 24000, Alfa Aesar) aqueous solution, 2 ml 120 mM $[Ag(NH_3)_2]^+$ aqueous solution which was made by adding ammonium hydroxide aqueous solution

(approximately 30 vol%, Fisher Scientific) into $AgNO_3$ aqueous solution, and 0.4 ml 1 mM Ag seed aqueous solution. Then, 10 ml 10 mM ascorbic acid ($C_6H_8O_6$, Alfa Aesar) aqueous solution was added drop by drop in 30 min. The concentration of the resulting Ag NP aqueous solution is ~ 1.2 mM. Fig.3-9 shows the typical UV-VIS absorbance spectrum of the Ag NPs aqueous solution, the band of the peak is located at ~ 430 nm which is corresponding to particle size ~ 50 nm. The average particle size is 50 ± 10 nm based on 200 measurements. Fig.3-10a shows the SEM image of morphology for the NPs in aqueous solution with concentration of 0.2 mM, which indicates that the NPs were well dispersed. The TEM observation of the NPs is shown in the inset image of Fig.3-10a, and it shows that the NPs had irregular shapes. Further HRTEM analysis of the NPs indicates that the thickness of the PVP coating was ~ 2 nm (Fig.3-10b, based on 10 measurements).

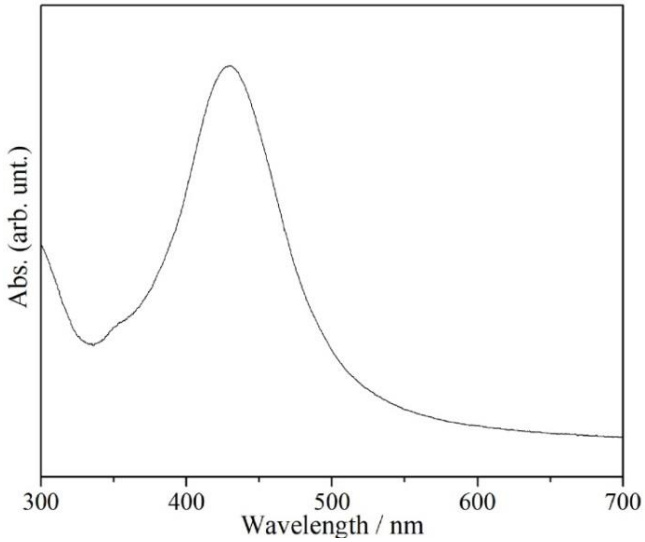

Fig.3-9, Typical UV-VIS spectrum of Ag NPs aqueous solution.

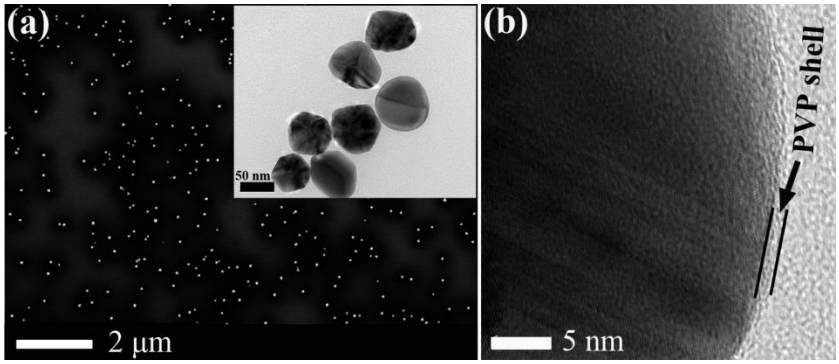

Fig.3-10, SEM and HRTEM images of the morphology for NPs in 0.2 mM solution. (a) SEM and TEM (the inset image) observation; (b) HRTEM observation of the surface of Ag NP.

3.5 Preparation of Ag NPs film

The prepared Ag NPs aqueous solution described in section 3.3 was centrifuged at speed 3000 r/min for 60min and re-dispersed into deionized water to eliminate the residual Ag seeds, and other ions in the solution. Ag NPs films with NPs embedded in the PVP matrix were obtained by immersing clean Si wafers (as received, <100> N-type, WRS Materials) into the re-dispersed Ag NPs solution and keeping them in a dry environment (humidity $\leq$ 35%) to let the water evaporate, as shown in Fig.3-11a. Fig.3-11b shows the SEM image of the morphology for the Ag NPs film. It indicates that the film consisted of a single-layer of NPs at the edge and multiple-layers of NPs in the center. The AFM measurement (Fig.3-11c) showed that the maximum number of NPs layers in the center was ~ 6 (obtained by dividing the particle size 50 nm by the measured height ~ 300 nm of the film). Ag NPs films on silica glass were also prepared using a similar method and then used for UV-VIS absorbance spectrum investigation.

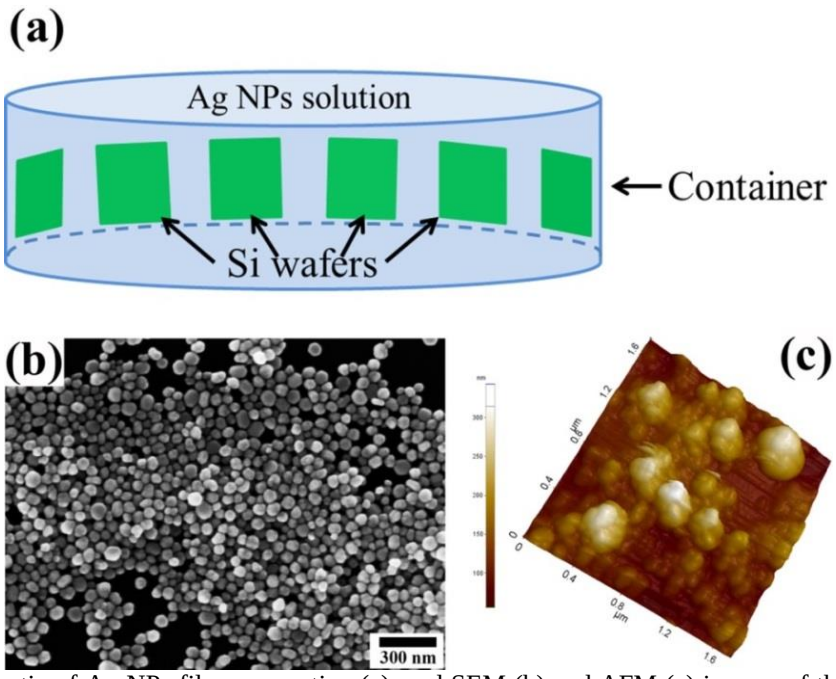

Fig.3-11, Schematic of Ag NPs film preparation (a), and SEM (b) and AFM (c) images of the surface of the NPs film.

3.6 Deposition of Ag particles on silicon wafers

Ag particles were deposited on the Si wafers by fs laser ablation of an Ag target (99.99%, Kurt J. Lesker) in a vacuum at a base pressure of 10^{-6} Torr. The schematic setup for fs laser deposition is shown in Fig.3-12. The fluence used to ablate the Ag target was ~ 1.4 J/cm^2 and ablation proceeded for 10 sec. The particles landed with their flat surface in contact with the Si substrate. The particle shape is similar to an elliptic cylinder (demonstrated later in chapter 5). Fig.3-13a and 13b shows the morphology of the particles; it was found that some donut-like particles were present in the deposited particles, suggesting the ablated material from the target were in a softened or even molten state prior to sticking the substrate. The aspect ratio of the particles is 1.08 ± 0.06 based on 200 measurements and the diameter/height ratio was 2.8 ± 0.6 based on 45 measurements. Size distribution analysis based on 200 measurements showed that the size of the particles ranged from 50 nm to 600 nm (Fig.3-13b). Here, particles with size less than 50 nm were

not counted since it is difficult to distinguish the morphology change of those particles before and after laser radiation.

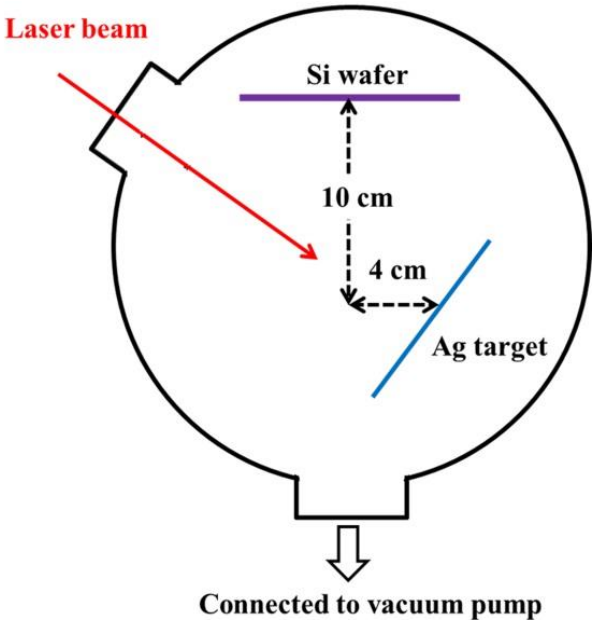

Fig.3-12, The schematic setup of fs laser deposition system.

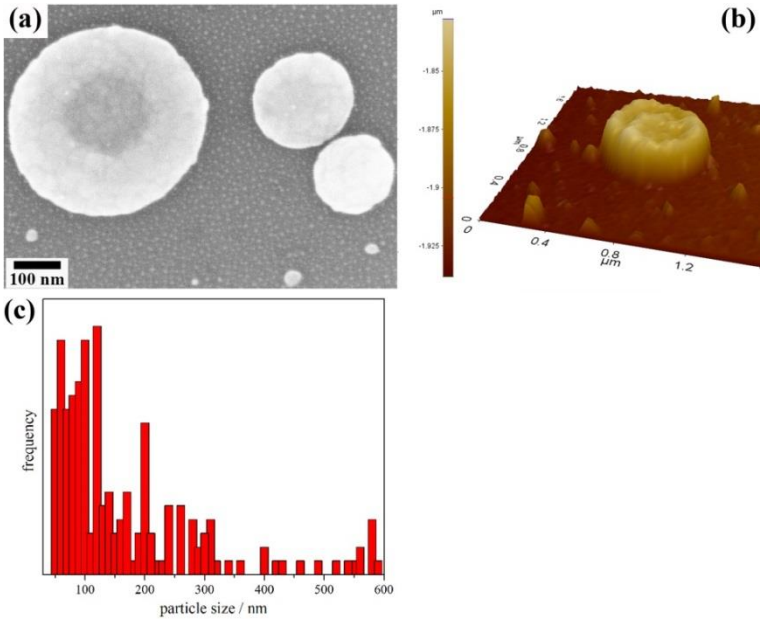

Fig.3-13, SEM image (a) and AFM image (b) of the morphology, and size distribution (c) of deposited Ag particles.

Chapter 4 Controlled Joining of Silver Nanoparticles in Aqueous Solution by Femtosecond Laser Irradiation

4.1 Introduction

With recent development and research in plasmonics, the surface plasmon property of NPs has been extensively studied. A major focus of research into surface plasmon has involved the directed assembly of NPs structures for applications ranging from bio-sensing [76], to solar energy harvesting [14], and to photothermal imaging [15]. As discussed in Chapter 1, a variety of methods have been utilized to fabricate NPs structures. For example, Yao *et al.*[22] and Gandra *et al.*[77] produced Au NPs with core-satellite structures using DNA and p-aminothiophenol as molecular linkages. However, chemical fabrication processes are frequently complicated and time-consuming. Alternative techniques such as those incorporating electric/magnetic field induced dipole-dipole interactions [78-80] are faster and simpler and have been widely studied, but the use of inter-NP polymer linkages can introduce inconsistency in the plasmonic properties of the resulting structures [81].

Recently, laser assembled NPs structures have attracted much attention because the laser method is straightforward and readily implemented. It has been demonstrated that NPs can be manipulated by using laser-induced optical forces, and that robust joining of NPs is facilitated by the optical electric field which is concentrated near hotspots between nearby NPs [82-84]. However, when a CW laser or conventional (ps, ns, and ms) pulsed laser is used, the low laser intensities required to avoid thermal damage in the NP structures [85] result in optical forces that are weaker than those arising from van der Waals interactions [86]. Under these conditions, the resulting NPs structures are poorly constrained. Fs laser

radiation is a promising alternative for the fabrication of NPs structures, as high peak intensities (usually 10^{14}-10^{15} W/cm^2) are known to induce strong optical forces on NPs. Meanwhile, the limited thermal damage associated with fs laser pulse interactions with materials facilitates the fabrication of NPs structures having different geometries that can be tailored to optimize tunable plasmon properties [87].

As metallic NPs are usually prepared in solution by chemical synthesis methods, fs laser radiation is studied here to join Ag NPs in an aqueous solution. To obtain controlled joining of Ag NPs in aqueous solution, two technical issues have to be overcome. One is the random motion of the NPs which makes controlled joining of NPs difficult. The other is the polymer shell on the surface which is usually used to control the geometry of the NPs and protect them from aggregation. The presence of polymer coatings will prevent the formation of a robust metallic bond between the NPs. These two issues can be solved by utilizing high intensity laser radiation, because the polymer will decompose under that condition while the laser induced optical gradient force can dominate the motion of the NPs over the Brownian motion and turbulent motion due to fs laser induced heating of the aqueous solution or ablation of the irradiated NPs[17, 86]. It is noted that a high intensity (or high fluence) fs laser radiation may cause damage to the NPs. As Hu *et al.* [42] reported, fragmentation of NPs dominated at intensity > 10^{14} W/cm^2 while joining of NPs was produced in intensity range of 10^{10}-10^{14} W/cm^2. In this section, joining of Ag NPs by utilizing both high fluence and low fluence fs laser radiation is studied, in order to develop a systematic understanding of fs laser nanojoining techniques at different intensity levels.

4.2 Experimental and simulation setup

Two laser fluence ranges (> 1.8 J/cm^2, and < 380 μJ/cm^2) were selected to investigate the joining behavior of Ag NPs in aqueous solution. Intermediate fluence fs laser radiation was not studied due to facility limitation, and it is expected to be the combined effect of high fluence and low fluence fs laser radiation. In high fluence range (> 1.8 J/cm^2), the prepared Ag NPs solution as mention in chapter 3 was diluted with deionized water to ~ 0.01 and 0.05 and 0.2 mM before laser radiation. Samples of 5 ml of these diluted Ag NPs solutions were then placed into individual quartz cells (3 mm x 2mm x 1 mm) and irradiated with focused (spot size ~10 μm) S polarized fs laser pulses for various exposure times. Pulse energies of 85, 200 and 500 μJ were obtained by attenuating the beam with neutral density filters. SEM and TEM were used to analyze the particle morphology. The transmittance of the irradiated samples was characterized using UV-VIS-NIR spectroscopy. SERS enhancement of the obtained sub-micron plasmonic structures which were deposited on clean Si substrates was evaluated using 10^{-3} M adenine solution as analyte [88]. Raman signals from six spots of the sub-micron structures were collected for analysis. The SERS detection limit was also evaluated by reducing the concentration of adenine solution to 10^{-5}, 10^{-7} and 10^{-9} M. The wavelength of the laser for excitation of SERS spectra was 633 nm. FDTD software (Lumerical Inc.) was used to model the distribution of hotspots in representative sub-micron structures. The light source is total field scattering field (TFSF) plane wave with wavelength of 800 nm, and the same setup is applied to the FDTD simulations of Chapters 5-6.

In low fluence range (< 380 μJ/cm^2), the prepared Ag NPs solution as described in chapter 3 was diluted to ~ 0.2 mM, and 5 ml of this dilute solution was placed into a quartz cell

and irradiated for 20 min. Pulse fluences of 95, 200 and 380 μJ/cm^2 were obtained by attenuating the beam with neutral density filters. SEM and TEM were used to analyze NPs morphology. Raman spectra of pure PVP and PVP coated Ag NPs before and after irradiation were obtained after deposition on cleaned Si substrates; while a 10^{-3} M adenine solution was used to evaluate SERS enhancement by Ag NPs before and after irradiation. The wavelength of the exciting laser for Raman and for excitation of SERS spectra was 488 nm.

4.3 Control of the geometry of joined NPs by high fluence fs laser radiation

4.3.1 Effect of laser fluence

Fig.4-1 shows SEM images of the products extracted from the 0.01 mM Ag NPs solution after irradiation at different fs laser pulse fluences. It is evident that Ag sub-micron structures were generated following 60 min of laser irradiation (Figs.4-1a, 1c and 1e). These sub-micron structures were not present in the original Ag NPs solution as shown in Fig.3-9. SEM images at higher magnification (Figs.4-1b, 1d and 1f) indicated that the surfaces of these sub-micron structures were decorated by smaller Ag NPs (HRTEM images are shown later) and that the shape of the sub-micron structures depended on the laser pulse fluence.

Fig.4-1b shows that ellipsoidal sub-micron structures were formed after irradiation at pulse fluence ~1.8 J/cm^2, while cubic sub-micron structures (Fig.4-1d) and other structures with highly organized features (Fig.4-1f) were produced at pulse fluences of ~4.2 and 10.5 J/cm^2, respectively. This suggests that the morphology of the sub-micron structures can be tailored. In this context, the modification of NP shapes has been shown to be useful in obtaining tunable plasmonic properties [87]. It should be noted that sub-micron structures

with some of these characteristics were also observed in the NP solutions irradiated at different fluences. This is probably due to the random motion of the NPs and the non-uniform spatial distribution of laser intensity in the solution during irradiation.

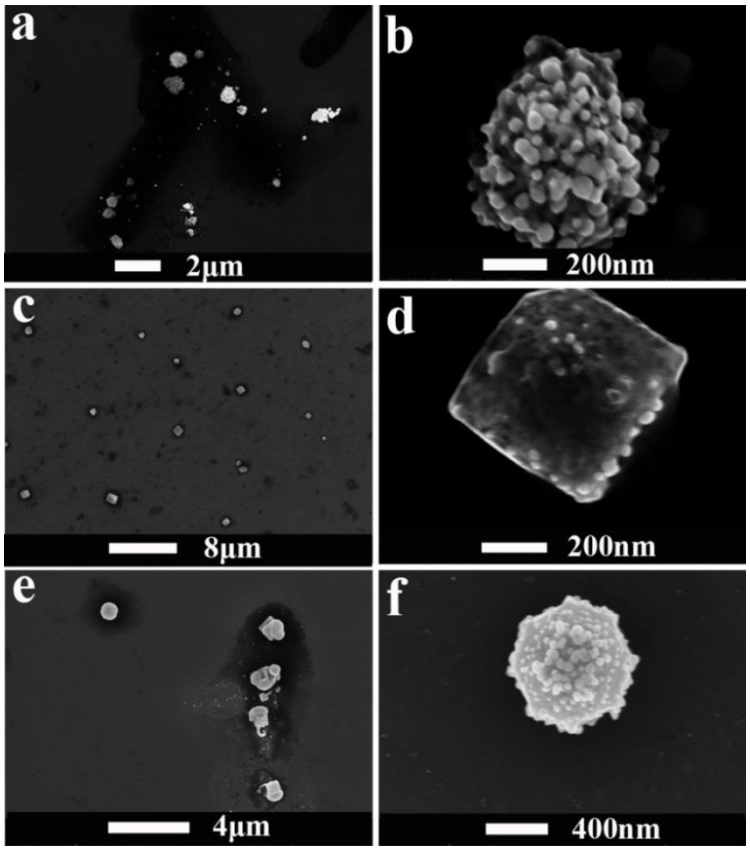

Fig.4-1, SEM images of sub-micron structures extracted from 0.01 mM Ag NP solutions which were irradiated by fs laser under different irradiation parameters. (a, b) 1.8 J/cm^2 for 60 min; (c, d) 4.2 J/cm^2 for 60 min; (e, f) 10.5 J/cm^2 for 60 min.

4.3.2 Effect of concentration

The concentration of Ag NPs in solution was then increased to 0.05 mM and 0.2 mM in order to produce a higher abundance of sub-micron structures using this technique. With the same irradiation conditions as at lower concentration, sub-micron structures with similar morphology were obtained in a 0.05 mM Ag NPs solution (Fig.4-2), while the size and shape of the sub-micron structures were more uniform. Figs.4-2a and 2b show that Ag sub-micron structures with diameters of 450±130 nm together with individual NPs were

obtained after laser radiation at a pulse fluence of approximately 1.8 J/cm^2. The diameter of the sub-micron structures increased to 710±140 nm when the pulse fluence was increased to ~ 4.2 J/cm^2, and some NPs were still found in the surrounding medium (Fig.4-2c and2d). A further increase in the pulse fluence to ~ 10.5 J/cm^2 resulted in the transformation and enhanced joining of NPs and sub-micron particles into large micron structures with diameters of 1480±300 nm (Figs.4-2e and 2f), as well as a small number of sub-micron structures with diameters of 620±100 nm (Fig.4-2g).

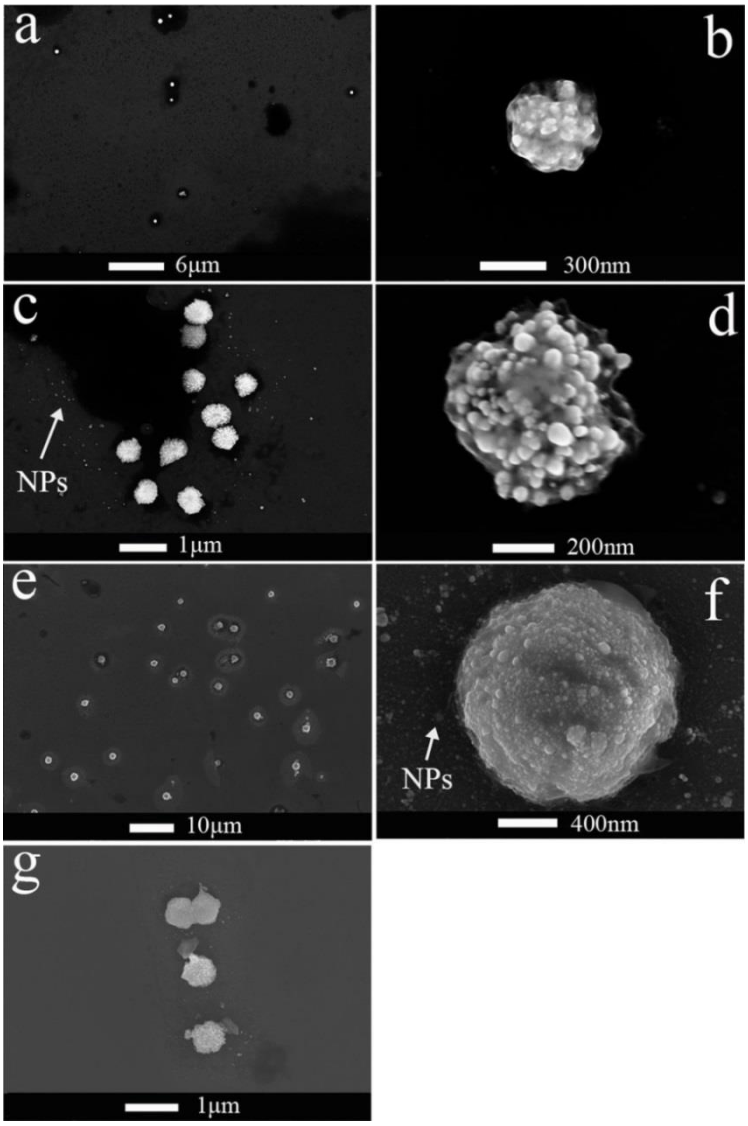

Fig.4-2, SEM images of sub-micron and micron structures extracted from the 0.05 mM Ag NP solutions which were irradiated by fs laser under different irradiation parameters. (a, b) 1.8 J/cm^2 for 60 min; (c, d) 4.2 J/cm^2 for 60 min; (e, f, g) 10.5 J/cm^2 for 60 min.

Similar sub-micron structures could still be obtained when the concentration of the Ag NPs solution was increased to 0.2 mM. However, much of the residual original Ag NPs were present in the solutions which were irradiated at fluences ~ 1.8 and 4.2 J/cm^2 for 60 min, due to the incomplete interaction among the NPs. At a fluence of approximately 1.8 J/cm^2, the size of the ellipsoidal sub-micron structure was ~ 200 nm (Figs.4-3a and 3b). When the fluence increased to 4.2 J/cm^2, cubic sub-micron structure (Fig.4-3c) with edge length of ~500 nm generated beside ellipsoidal structure (the inset of Fig.4-3c) which is similar to those obtained in solution with concentration of 0.01 mM. The magnified image of the cubic sub-micron structure clearly shows that it was porous and formed via the joining of NPs (Fig.4-3d). When the fluence was further increased to ~10.5 J/cm^2, clusters of spherical sub-micron structures or other shaped structures were produced (Figs.4-3e, 3f). This can be attributed to fs laser induced joining which resulted from LSP-induced electric field enhancement. As reported, under fs laser irradiation, Ag sub-micron particles could be attracted and joined to the Au bowtie structures where the LSP produced an electric field enhancement and exerted an attractive force on the nearby NPs [17].

It should be noted that there were also some NPs with size of ~ 5-100 nm surrounding the sub-micron and micron-sized structures (Fig.4-2f and Fig.4-3f), which was demonstrated later by the TEM observation. These NPs were likely produced by the ablation of sub-micron and micron-sized structures or they might be remnants of the original NPs in the solution. Again, all the sub-micron and micron-sized structures were also decorated by smaller NPs (Figs.4-2 and 4-3).

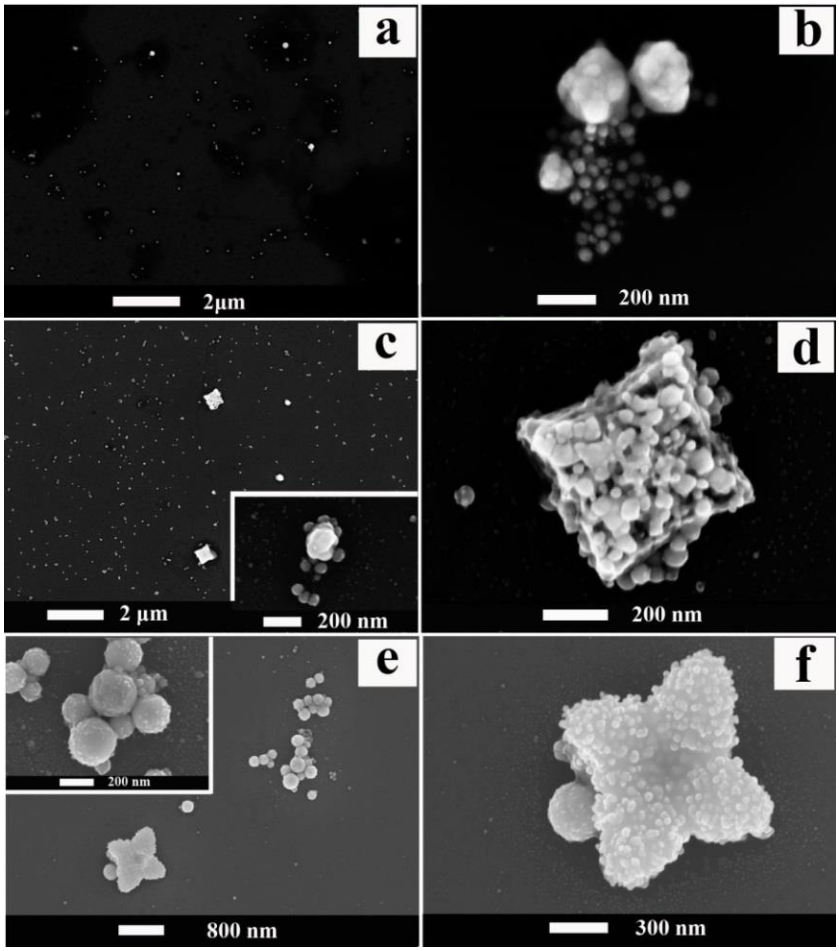

Fig.4-3, SEM images of sub-micron structures extracted from 0.2 mM Ag NP solutions which were irradiated by fs laser irradiation at different fluences for 60 min. (a, b) 1.8 J/cm^2; (c, d) 4.2 J/cm^2, the inset in c shows the magnified SEM image of the ellipsoidal structure; (e, f) 10.5 J/cm^2, the inset in (e) shows the magnified SEM image of joined sub-micron structures.

4.3.3 Effect of laser irradiation time

To understand how the sub-micron and micron-sized structures were produced by fs laser joining, a 0.05 mM aqueous solution of Ag NPs was irradiated at a pulse fluence of approximately 10.5 J/cm^2 for different times. Figs.4-4a, 4b and 4c show the morphology of the particles/structures in the solution before and after laser irradiation. It can be seen that, before irradiation, some Ag NPs were linked in networks as a result of inter-particle agglomeration (Fig.4-4a), which could be due to van der Waals force, electrostatic interaction or chemical effects [89]. After 20 min irradiation, the number of Ag NPs

networks was reduced and some sub-micron particle-like structures with variable diameters began to appear (Fig.4-4b). The inset in Fig.4-4b shows the morphology of the large structures, and indicates that these sub-micron structures (290±100 nm) were covered with many NPs as observed in the structures shown in Figs.4-2 and 4-3. It is believed that these NPs decorated sub-micron structures will favor the plasmonic enhancement [88]. When the irradiation time was increased to 40 min (Fig.4-4c), Ag NPs were transformed into large well dispersed sub-micron structures with diameters of 160±50 nm. The size reduction of sub-micron structures from 290±100 nm to 160±50 nm is attributed to the densification of the NPs structures due to local heating at the hotspots [66] after long irradiation times. After a further increase in the irradiation time to 60 min, the 160 nm sub-micron structures were no longer observed, and the ~1480 nm diameter micron structures were generated (Figs.4-2f). These micron structures with diameters of approximately 1480 nm could then be attributed to fs laser induced joining of the 160 nm sub-micron structures as mentioned above.

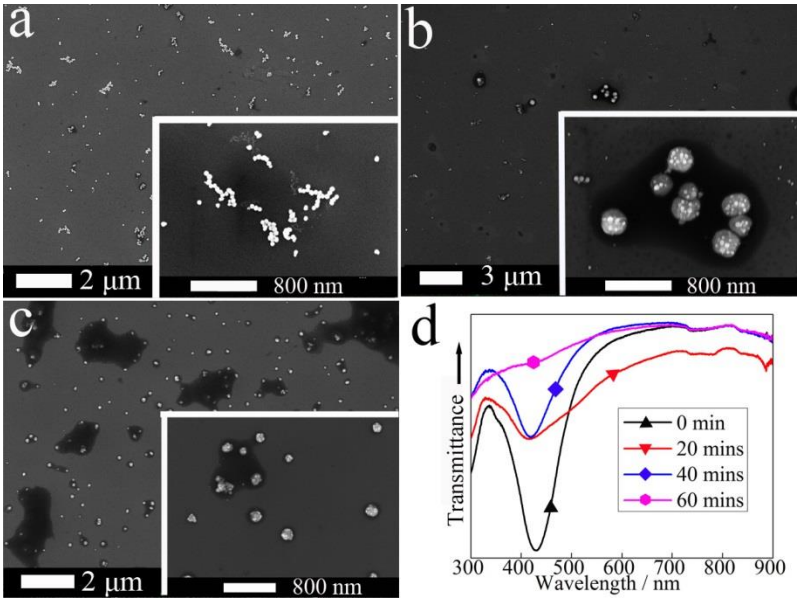

Fig.4-4, SEM morphologies and transmittance spectra of samples after irradiation at a pulse fluence of 10.5 J/cm^2 for different times. (a) 0 min; (b) 20 min; (c) 40 min; (d) transmittance spectra after different irradiation times.

As discussed above, NPs could be attracted and joined together because of the enhanced optical force and heat generation at the hotspots [66, 70]. The diameters of the sub-micron structures would increase as more NPs were attracted and joined to the existing sub-micron structures. In addition, it is apparent that even sub-micron structures could also be combined, resulting in the size increase of the structures. On the other hand, further sintering among NPs and sub-micron structures due to hotspots-enhanced heating may reduce their diameters. Therefore, the final observed diameters reflect the interplay between these two factors, which may explain why the diameters of the sub-micron structures at 40 min are smaller than those at 20 min.

Transmittance spectra (Fig.4-4d) of the NPs solution before and after irradiation provided more evidence about the formation of sub-micron/micron structures during fs laser irradiation. These spectra show that the transmittance of the original NPs (50 ± 10 nm) was reduced at 430 nm, due to excitation of the plasmon resonance which enhances the scattering and absorption of incident light [59]. After 20 min of irradiation, the transmittance at 430 nm increased. This is associated with a reduction in the concentration of the original NPs. The transmittance of the solution between 550-900 nm decreased after 20 min irradiation, following the formation of larger particles that scatter and absorb laser radiation efficiently over this wavelength range [90]. This is consistent with the SEM observations in Fig.4-4b, and the observation of a scattering peak at 880 nm indicates that large particles/structures were present in the irradiated solution [91]. With an increase in the irradiation time to 40 min, the transmittance between 550 and 900 nm was increased while that at 430 nm was almost unchanged. This is probably due to the growth of NPs together with the densification of 290 ± 100 nm sub-micron structures into 160 ± 50 nm sub-

micron structures with resonance wavelengths in the near infrared. After a further increase in irradiation time to 60 min, the resonance peak at 430 nm disappeared and no other resonance peaks could be seen in the spectrum, suggesting that most of the NPs have become incorporated into the sub-micron and micron sized structures. It is noted that although the fs laser pulses were sufficiently intense to fragment NPs [66, 68, 92], no blue shift in the NP resonance was observed here. This is in contrast to the previous research reports [66, 68, 92]. It can be attributed to the fact that only a small number of NPs were fragmented while the products of this fragmentation had a wide size distribution which broadens the plasmon resonance.

4.3.4 Investigation of joining mechanism

Based on the above discussion, the formation of sub-micron structures is attributed to the joining of NPs. In these kinds of joined NPs structures or sub-micron structures, the surface plasmon becomes localized, forming hotspots adjacent to the joined NPs or sub-micron structure. These hotspots produce two effects: one is to produce local heating [66], which accelerate the joining of NPs; the other is to increase the electric field gradient between hotspots and the surrounding medium, which enhances the attraction to the nearby NPs via enhanced optical gradient force [70]. These two effects will facilitate further joining of NPs, implying that the joining of NPs into the above observed sub-micron or micron structures was in response to the development of hotspots.

To investigate the possibility, a 3D FDTD simulation was performed to identify the development of the hotspots. In the simulation, for simplification, individual NPs in the aggregates were assumed to be 50 nm in diameter, and the bold red lines in Fig.4-5 traced the outlines of the NPs (cross-section view). The simulation began with two welded NPs

(which is relatively easy to obtain) with a certain overlap distance (surface to surface distance) *d* which is defined in Fig.4-5a. As shown in Fig.4-5b, the initial overlap distance *d* between welded NPs was very small (~ 2 nm, measured from the NPs solution which were irradiated by fs laser at fluence 10.5 J/cm^2 for 30 sec).

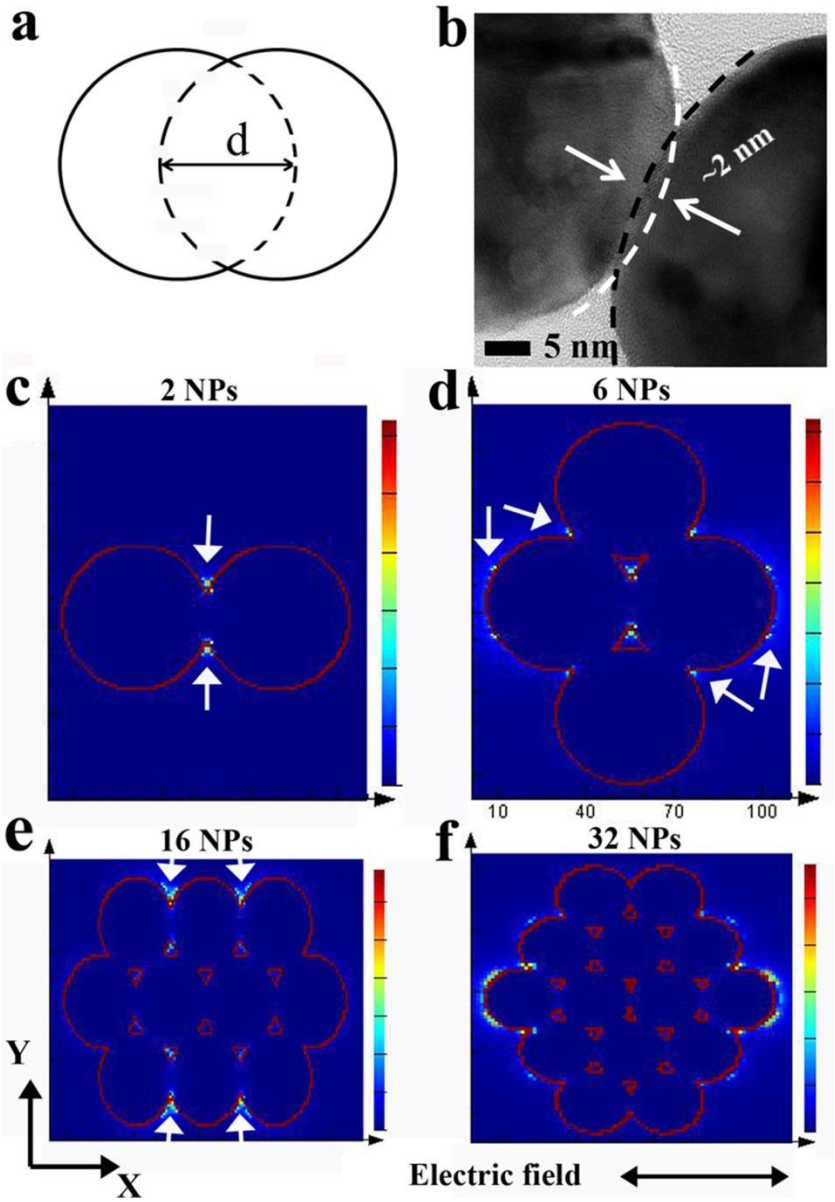

Fig.4-5, FDTD simulation of electric field distribution in welded NPs structures. (a) Definition of overlap distance d; (b) measured overlap distance; (c, d, e, f) electric field distribution in structures containing 2, 6, 16 and 32 NPs, respectively. The arrows in the images show the locations of the hotspots in the structures. The incident laser is perpendicular to the XY plane. The double ends arrow indicates the laser polarization direction.

After laser irradiation with polarization parallel to the X axis of the welded structure, the locations of the hotspots in the welded structure were identified (as shown by the arrows in Fig.4-5c). By introducing additional NPs into the hotspots where the electric field was enhanced, the distribution of the hotspots in the resulting larger welded NPs structures could be identified (Fig.4-5d). With further continuous placement of NPs in hotspots, larger sized or even the final welded NPs structures could be modeled (Figs.4-5e and 5f). It is clear that when the overlap distance was fixed to 2 nm, a 3D welded NPs structure was developed by continuously introducing additional NPs into the hotspots (Fig.4-5f). Similar structure development (in two dimensions) was also observed in the simulations where one additional NP was introduced to the hotspots each time or the simulation started from three welded NPs in a row followed by introducing one additional NP each time. As shown in Fig.4-5f, the 3D structure (containing 32 NPs) had a diameter of ~250 nm. This is close to the observed 290 nm diameter of the structure which was obtained after fs laser irradiation at fluence ~10.5 J/cm^2 for 20 min. Then no NPs were further introduced in the structures, and the absorption spectra of the present structures were modeled.

The simulation results (Fig.4-6) show that with the increase of the number of NPs in the structure, the absorption at wavelength of 800 nm increased. When the number of the NPs in the structure increased to 32 (the diameter of the structure was ~ 250 nm), an absorption peak at 816 nm appeared. This is consistent with the UV-VIS spectra of the fs laser irradiated solution at fluence 10.5 J/cm^2 for 20 min, where the average diameter of the obtained sub-micron structure in the irradiated solution was 290 nm. This implies that the 290 nm sub-micron structure could be formed by hotspots-directed joining of Ag NPs. In addition, because the absorption wavelength of the structure was close to that of the

incident laser beam, significant absorption of the laser energy would happen in the welded structure due to the excitation of surface plasmon resonance (SPR) [66] and consequently result in the heating and compaction of the welded structure. This is probably the cause for the observed size reduction of sub-micron structure from 290 nm to 160 nm, when the irradiation time increased from 20 min to 40 min at fluence 10.5 J/cm^2.

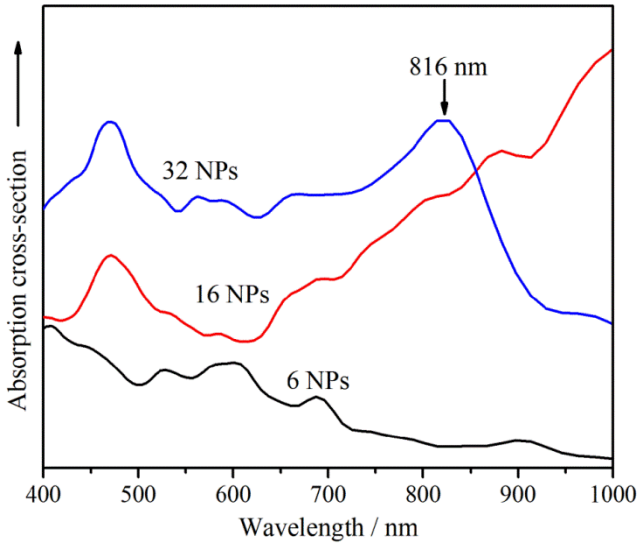

Fig.4-6, Calculated absorption cross section in the structures containing different numbers of Ag NPs.

It is noted that the FDTD simulation cannot perfectly mimic fs laser joining due to the irregular NP geometry, complex irradiation environment in the aqueous solution and the dynamic evolution of the geometry of the welded NPs structure during the whole joining process. Further studies are still needed to better understand LSP induced joining of NPs via an enhanced laser-induced optical gradient force.

The above analyses suggest that the generation and growth of sub-micron structures in the irradiated Ag NPs solutions can be associated with joining of particles induced by fs laser pulses. A schematic tracing of a possible formation sequence of sub-micron or micron sized structures is shown in Fig.4-7 where, for simplification, all the NPs are represented as

spherical particles. The initial process involves fragmentation of the original Ag NPs under fs laser irradiation. This results in the creation of many smaller NPs (5-20 nm in this study). Together with fragmentation, laser irradiation promotes the joining of smaller NPs and the original particles under the effect of optical gradient force. It is found that the hotspots generated in the joined NPs initiate local heating and the growth of NPs. Following this stage, laser induced joining and growth dominates, and the joined NPs structures continue to increase in size resulting in the formation of larger size structures with different shapes. This is balanced to some extent by laser ablation which tends to fragment the structures and change their shapes. The resulting size distribution and shape of the structures in solution is then likely determined by an evolutionary sequence in which the surviving structures in solution have a combination of size and geometry that minimizes coupling to the incident radiation field.

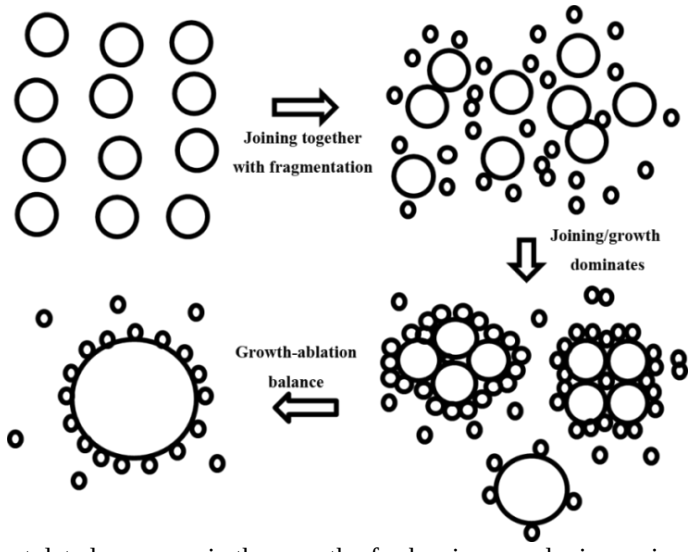

Fig.4-7, Postulated sequence in the growth of sub-micron and micron size structures.

4.3.5 Structure and SERS investigation

The sub-micron structures were further studied by using TEM, and their surface plasmon properties were also evaluated using SERS detection. Fig.4-8 shows the TEM images of

the sub-micron structures which were obtained by fs laser irradiation at a pulse fluence ~10.5 J/cm^2 for 40 min. It can be seen that many Ag NPs (50±10 nm) and smaller ones (5-20 nm in diameter, may be produced by laser induced fragmentation from the original 50 nm NPs) were collected on the surface and became joined to the larger (160±50 nm) core particle, forming a core-satellite structure. These sub-micron structures further combined in some cases to form even more complex-shaped structures (Fig.4-8a). The core-satellite NP structures have been reported to possess high SERS enhancement factors [77], implying that these complex-shaped structures in this work could be used for SERS detection.

HRTEM analysis shows that Ag NP (label ① in Fig.4-8b) has been welded to the core particle with the Ag(111) lattice planes aligned. This NP-core particle weld morphology would enable the generation of hotspots in the neck area, resulting in plasmonic enhancement. Bonding of tiny NPs to core particles via a thin layer of amorphous carbon (α-C) (this is demonstrated in the following section 4.4, and it is indicated by dashed lines in Fig.4-8b) was also observed. This bond configuration has also been demonstrated to be beneficial for the enhancement of SERS [93]. It is noted that the sub-micron structures or NPs were covered by α-C. This may influence the densification of the joined NPs or sub-micron structures arising from enhanced heating-induced sintering, but could improve their resistance to photochemical damage [94]. The SERS enhancement properties of these complex-shaped structures may also be fairly reproducible due to the narrow size distribution (5-20 nm) of the attached smaller size NPs (Fig.4-8b) and the robust NP-core weld strength.

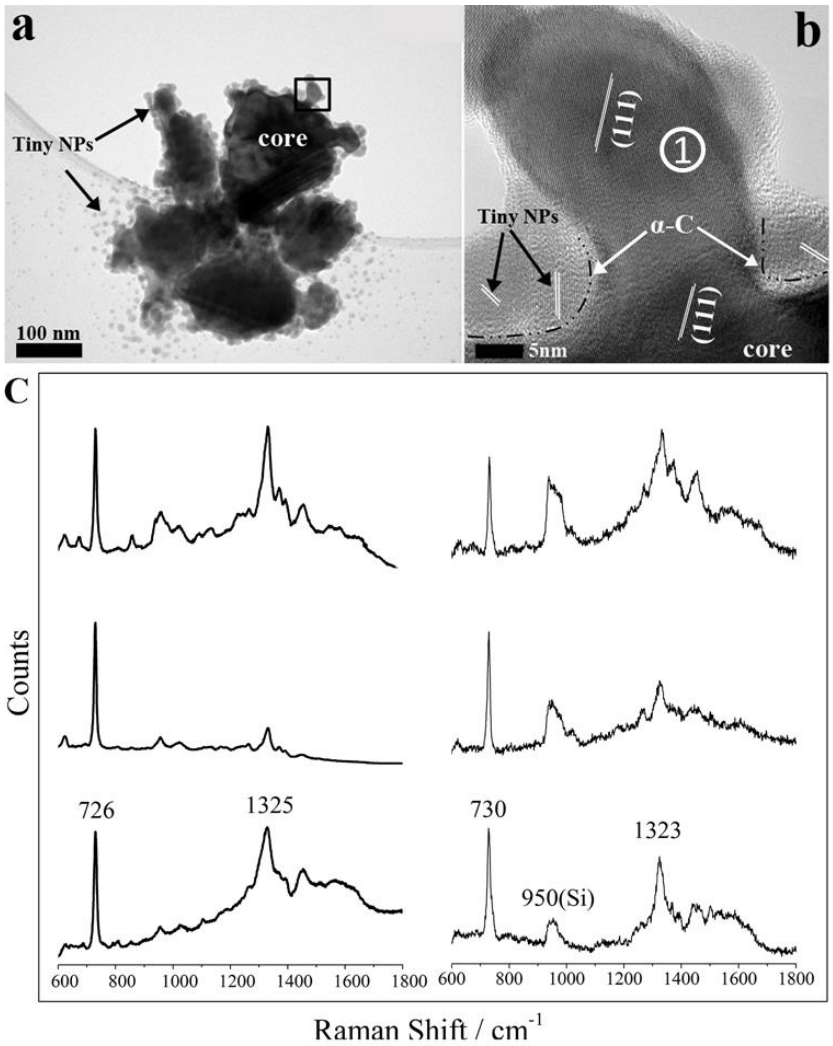

Fig.4-8, TEM observation and SERS analyses of the submicron structures extracted from NPs solution which were irradiated at a fluence of 10.5 J/cm^2 for 40 min. (a) TEM image of the morphology for sub-micron structures; (b) is taken from the square area in (a), the dash lines in (b) show the positions of amorphous carbon (α-C); (c) SERS results from 6 sub-micron structures spots (Raman spot size is ~ 1 μm) in the sample irradiated at fluence ~10.5 J/cm^2 for 40 min; the analyte molecule is adenine.

The SERS analyses of the sub-micron structures on the wafer (the data were collected from six spots) are shown in Fig.4-8c, and the sharp characteristic peaks of adenine [95, 96] at ~726 and 1325 cm^{-1} in the six spectra indicate that these sub-micron structures could produce high SERS enhancement and possess good reproducibility. Meanwhile, as the Raman laser spot size is ~ 1 μm, the number of sub-micron structures in the spot is very small, less than 6 as shown in Fig.4-8c. This suggests that these sub-micron structures

possess the potential for single particle SERS enhancement as required for ultra-sensitive bio-sensing [97].

To assess this possibility, SERS spectra were obtained for individual Ag particle structures with sizes ~ 160 nm for a range of low concentration adenine solutions. Fig.4-9 shows that when the concentration of adenine solution was decreased from 10^{-5} to 10^{-7} and then to 10^{-9} M, the diagnostic peak of adenine at ~1319 cm^{-1} gradually became undetectable. However, the spectral feature at ~735 cm^{-1} was observed although it became broader and its intensity relative to the Si peak 951 cm^{-1} decreased. This suggests that the sub-micron Ag NP structures produced using fs laser radiation contain a range of bonding sites having different enhancement characteristics. The activity of individual sites for SERS enhancement is reflected in the changes in the SERS spectra in Fig.4-9 as the concentration of adenine is reduced. This observation indicates that sub-micron Ag composite structures may exhibit useful properties for the detection of low concentrations of bio-molecules in solution.

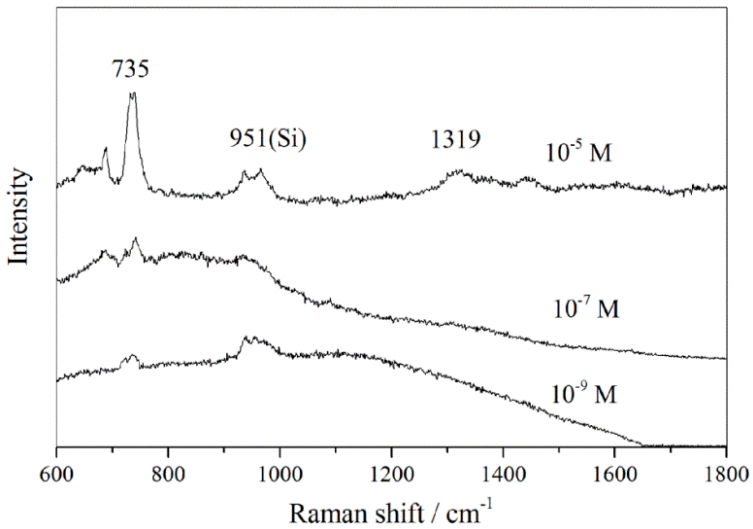

Fig.4-9, SERS spectra obtained from single ~ 160 nm Ag structures for different concentrations (10^{-5}, 10^{-7}, and 10^{-9} M) of adenine solutions.

4.4 Control of joint morphology by low fluence laser radiation

As reported in section 4.3, fs laser irradiation at high fluence possesses the ability of controlling the geometry of the welded NPs. However, high fluence fs laser radiation causes serious damage to the irradiated Ag NPs, this will limit its application in fabricating geometry sensitive plasmonic structures which were obtained by joining NPs. It is also found in numerical simulations that welded NPs are still not the most efficient structures for LSP enhancement [98]. These calculations indicate that dimers with a narrow inter-particle gap (~ 0.5 nm) are capable of producing the highest local electromagnetic field enhancements.

It is noted that Ag NPs which are prepared by chemical synthesis method as mentioned in chapter 3 are coated with a PVP protective layer; it is possible to obtain the Ag NPs dimers with narrow inter-particle gap by tailoring the thickness of PVP protective layer. Low fluence fs laser radiation is an interesting choice for this application, because it has been employed to modify the polymers and causes limited thermal damage to the irradiated Ag NPs. In addition, LSP in Ag NPs may also facilitate the fs laser fabrication process through LSP induced hot electrons emission which has been reported to dissociate molecules adsorbed on the surface of Au NPs [74]. The work of this section is to explore this feasibility of obtaining Ag NPs dimers with small separation distance by using fs laser radiation at low fluence (< 380 $\mu J/cm^2$) which can avoid the damage to the irradiated Ag NPs, and investigate the corresponding mechanism.

4.4.1 Morphology study of irradiated Ag NPs

Fig.4-10 shows TEM and HRTEM images of the morphology for Ag NPs after irradiation for 20 min at different fluences. It can be seen that fs laser radiation resulted in the

formation of Ag NP networks (Figs.4-10a, 10c and 10e), but that the shape of individual particles was not significantly affected by this process. Figs.4-10a and 10b show that after irradiation at a fluence of approximately 95 μJ/cm^2, Ag NPs were separated by a ~ 0.5 nm narrow gap and they appear to be bonded by a carbonaceous shell (demonstrated by Raman scattering analysis later). When the fluence increased to ~ 200 and 380 μJ/cm^2 (Figs.4-10c and 10e), part of the inter-particle gaps was replaced by necks.

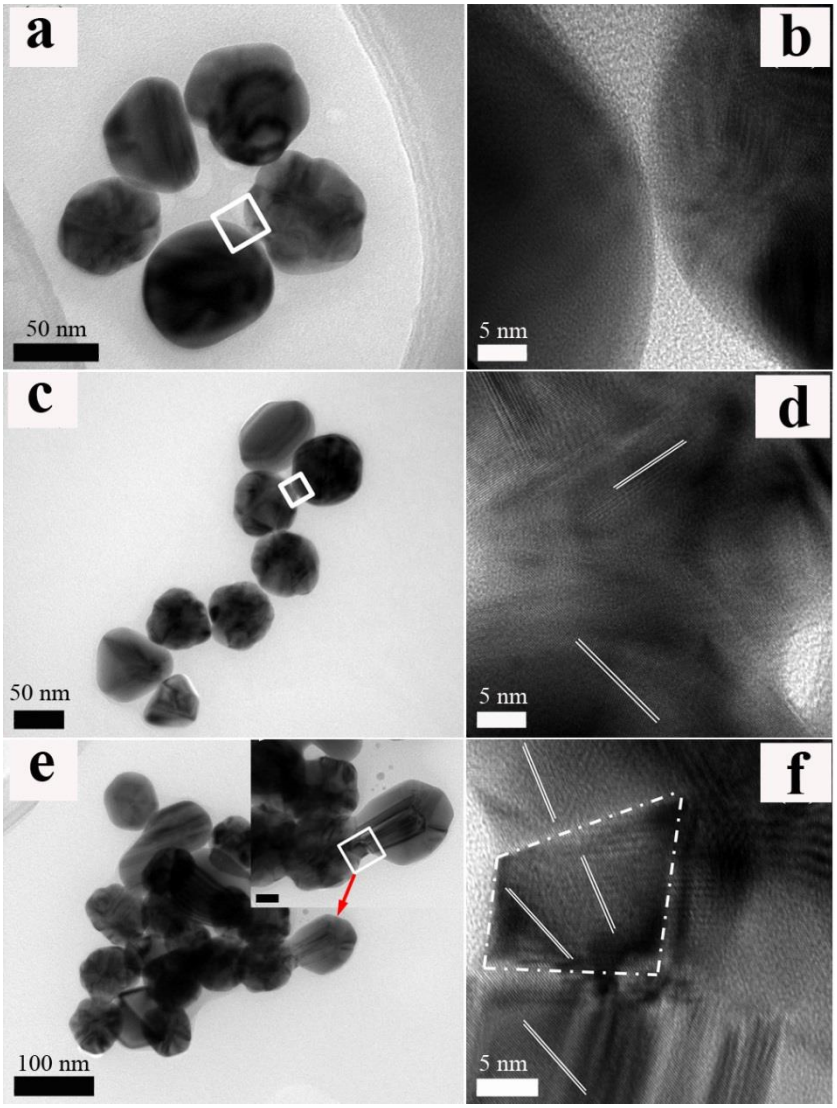

Fig.4-10, TEM (left) and HRTEM (right) images of Ag NPs irradiated by fs laser with different pulse fluence for 20 min. (a, b) 90 μJ/ cm^2; (c, d) 200 μJ/ cm^2; (e, f) 380 μJ/ cm^2. The scale in the inset figure is 20 nm.

HRTEM images show that these necks were metallic, acting as bridges between individual Ag NPs, and widen as the fluence increased (Figs.4-10d and 10f). The mechanisms of the coalescence between NPs, e.g., on how the neck layers form and how the coalescing atomic planes align to those of the NPs, have been discussed extensively in the literature [36, 99]. It appears in this work, that neck layers can form (see the dashed region in Fig.4-10f) where part of the planes are aligned almost parallel to those in the above NP while the others are parallel to those in the bottom NP. The formation mechanism of this configuration, which has not been reported in literature, needs further studies. It is clear from the above observations that the separation between Ag NPs (i.e., inter-particle distance) can be controlled by adjusting laser fluence, and that laser irradiation of NPs in solution may be a useful technique for tailoring the properties of Ag NP networks.

4.4.2 Investigation of joining mechanism

To understand how the Ag NPs were bonded by carbonaceous shells, the generation of carbonaceous shell is first discussed. Fig.4-11 shows the Raman spectra of Ag NPs before and after fs laser irradiation, which were obtained after deposition on a clean Si substrate. The Raman spectrum of a sample prepared from NPs prior to irradiation is shown in Fig.4-11a. Spectral features at 1202, 1235, 1495, and 1605 cm^{-1} are indicative of the presence of PVP [100] which forms a coating on each NP. After irradiation at a fluence ~95 $\mu J/cm^2$ (Fig.4-11b) for 20 min, peaks associated with the stretching vibration of sp^2 bonded carbon (the "G" peak) appeared at 1552 cm^{-1} together with bands at 1153, 1277 and 1458 cm^{-1} attributable to trans-polyacetylene chains [101-104]. These spectral features indicate that α-C:H was created from the irradiation of the PVP which was coated on the surface of Ag NPs. The Raman spectra in Figs.4-11c and 11d show that the G peak shifted

to 1572 and 1578 cm^{-1} while another feature "D" peak arising from sp^2-bonded carbon in defect sites in amorphous carbon (α-C) appeared at 1346 and 1348 cm^{-1} in samples irradiated at fluences of 200 and 380 $\mu J/cm^2$, respectively. The amplitude ratio of the D and G peaks (I_D/I_G) was also found to increase with fluence, indicating that the C/H ratio and structural order were enhanced in α-C:H under these conditions [105].

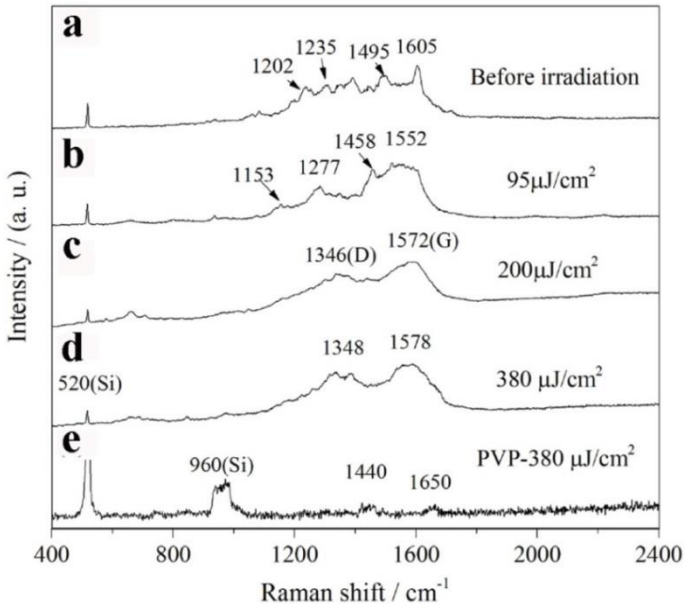

Fig.4-11, Raman spectra of Ag NPs and PVP in aqueous solution before and after irradiation with fs laser pulses. (a) NPs before irradiation; (b) NPs after irradiation at 95 $\mu J/cm^2$; (c) NPs after irradiation at 200 $\mu J/cm^2$; (d) NPs after irradiation at 380 $\mu J/cm^2$; (e) pure PVP solution after irradiation at 380 $\mu J/cm^2$.

Since PVP is only weakly absorbing at 800 nm, it is unlikely that PVP can be decomposed by direct fs laser irradiation in an aqueous solution at low fluence. The Raman spectrum of an aqueous solution of PVP after irradiation at fluence ~380 $\mu J/cm^2$ can be seen in Fig.4-11e and is characterized by the C=O, C-N stretching bands [106] of the PVP molecule. No spectral features of α-C:H or α-C were detected, indicating that PVP in aqueous solution was not decomposed under direct fs laser irradiation at low fluence conditions. Therefore, the formation of α-C:H and α-C may be due to the thermal decomposition of PVP at the surface of Ag NPs as reported previously [107].

To understand the mechanism for the thermal decomposition of PVP on the surface of Ag NPs, Raman spectra for Ag NPs extracted from aqueous PVP solution after these have been heated for 3 min in air at various temperatures (Fig.4-12) were obtained. Spectral features at 1613 and 1510 cm^{-1} after heating to 200 ℃ (Fig.4-12a) indicates that PVP was still present on the surface of Ag NPs, but peaks at 1288, 1350 and 1549 cm^{-1} show that some PVP had decomposed into α-C:H [101-104]. After heating to 300 ℃ (Fig.4-12b), residual PVP was completely converted to α-C:H. A further increase in heating temperature to 400 and 500 ℃ converted α-C:H into α-C and led to the appearance of D and G bands at 1353 and 1566 cm^{-1} (Figs.4-12c and 12d). As expected, the I_D/I_G ratio increased when the heating temperature increased from 400 to 500 ℃. These results indicate that temperatures in excess of ~200 ℃ are required to thermally decompose PVP adsorbed on the surface of Ag NPs.

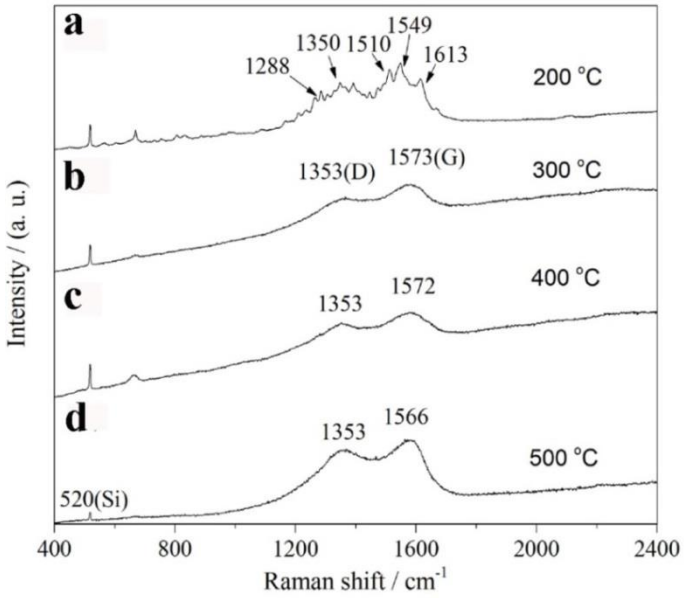

Fig.4-12, Raman spectra of Ag NPs heated to different temperatures in air: (a) 200 ℃; (b) 300 ℃; (c) 400 ℃; and (d) 500 ℃.

To see if this temperature rise, ΔT, is consistent with irradiation conditions, ΔT can be estimated from the energy, E, absorbed during the laser pulse

$$E = \pi F Q_{abs} r^2 = \frac{4}{3}\pi\rho C \Delta T r^3 \qquad (4\text{-}1)$$

where Q_{abs} is the particle absorption efficiency, F (J/m^2) is the pulse fluence, r (m) is the equivalent radius of the NP, ρ is the density of Ag=1.05x10^4 kg/m^3, and C=230 J/(kg • ℃) is the heat capacity of Ag. Since $r << \lambda$ and laser fluence is low, Q_{abs} can be calculated using the Rayleigh approximation [108]

$$Q_{abs} = -\left(\frac{8\pi r}{\lambda}\right) I_m\left[\frac{\left(m^2-1\right)}{\left(m^2+2\right)}\right], \qquad (4\text{-}2)$$

where $m = n' - Ki$ = 0.144 – 5.29i is the complex refractive index for Ag [45] at λ=800 nm. Then, taking r=2.5x10^{-8} m as a representative radius for the Ag NPs in our samples, Q_{abs}=0.0038. Fig.4-10c shows that localized fusion between adjacent Ag NPs was produced at F = 2 J/m^2 but ΔT calculated from eqn. (4-1) predicts that the temperature rise is << 1 ℃ under these conditions. This implies that thermal heating is not the cause of the observed decomposition of PVP and welding between Ag NPs at fluences between 200 and 380 μJ / cm^2.

Then, the role of LSP induced hot electrons emission from the Ag NPs on the decomposition of PVP is investigated. As known, the localization and enhancement of the electric field at the interface between NPs due to LSP results in hotspots and then enhances electron or ion emissions from the NPs [73]; and this likely occurs under the conditions of the present experiments. Electrons/ions emitted from the surfaces in the hotpots area give rise to two primary effects: the first is to initiate the decomposition or dissociation of PVP and the conversion of this material to α-C:H and α-C [74], while the second effect will be to produce a softening of the lattice at the Ag surface.

Fig.4-13 shows the structure of PVP and the bond energies for certain bonds in PVP [109]. It indicates that the bond energy of the C-N bond has the lowest value, suggesting that it is easier for the C-N bond to be dissociated under the impact of electrons/ions which were emitted from the surface of irradiated Ag NPs. The dissociation of C-Ns bond will then result in the formation of trans-polyacetylene chain. This is consistent with the Raman spectra result (Fig.4-11) which shows the existence of α-C:H and α-C [110], and it mimics the effects of thermal heating including spallation [111, 112] of this layer. It therefore appears that modification of the structure of PVP by impact of electrons/ions is responsible for the similarities between Raman spectra of laser processed and thermally heated material as shown in Fig.4-11 and 4-12.

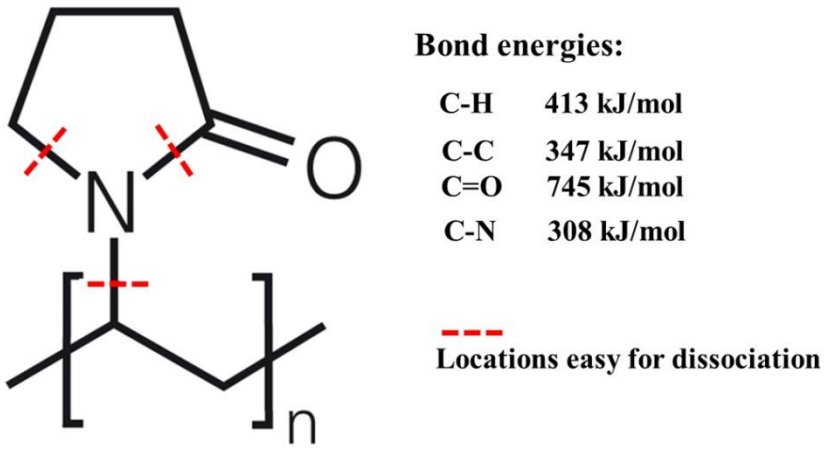

Fig.4-13, Structure of PVP and the bond energies for certain bonds in PVP. The red bar indicates the location which is easy for dissociation.

The produced α-C:H was then coated to the surface of Ag NPs. Because α-C:H is hydrophobic, Ag NPs coated with this material tended to aggregate to form networks. A reduction in surface energy, as well as plasmonic interactions [70] would also favor network formation. After network formation, hotspots arising from LSP at the interface were generated between adjacent NPs. This enhanced the overall emission of electrons or

ions and leaded to a reduction in volume or elimination of α-C:H or α-C on the surface of NPs, facilitating the welding and formation of metallic necks between adjacent NPs. It should be pointed out that direct heating of α-C:H or α-C layers can also occur via Ohmic heating induced by the electric field of the incident light wave [69]. At low fluence, impact of electrons or ions and Ohmic heating effects are minimized, and Ag NPs are connected by α-C:H bridges (see Figs.4-10a, and 10b). Welding of Ag NPs at fluences between 200 and 380 $\mu J/cm^2$ is then accompanied by a reduction in the volume of the α-C:H shells as these are removed by electron/ion impact. It is reasonable to expect that all the α-C:H bridges can be replaced by the necks at fluences between 200 and 380 $\mu J/cm^2$ if the irradiation time is sufficiently long. The above analyses suggest that the contact geometry between adjacent Ag NPs can be manipulated by controlling the laser fluence.

4.4.3 SERS investigation

SERS spectra of adenine absorbed on Ag NP deposits after irradiation were obtained, as shown in Fig.4-14, to evaluate the LSP induced electric field enhancement in samples prepared at different fluence levels. In previous studies, it has been shown that the Raman peaks of adenine at 730 and 1327 cm^{-1} are diagnostic of the SERS enhancement effect [42, 95, 96] and that the bands of adenine were significantly enhanced in SERS spectra of welded Ag NPs [95]. In addition, Ag NPs joined through highly conjugated carbon chains exhibit a 10x larger Raman enhancement than single NPs [93]. The spectra in Fig.4-14 indicate that a narrow gap mediated by the presence of an extremely thin α-C:H film (~ 0.5 nm thickness), gives even higher SERS enhancement than that occurring in welded NPs. This is consistent with the results of calculations showing that the enhancement cross-section in dimers is largest when the gap between NPs is reduced to 0.4~1 nm, and

reducing the gap to zero results in a nonlinear reduction of the plasmon-induced field enhancement due to the neutralization of charge density on opposite sides of the gap in response to an induced current flow [98].

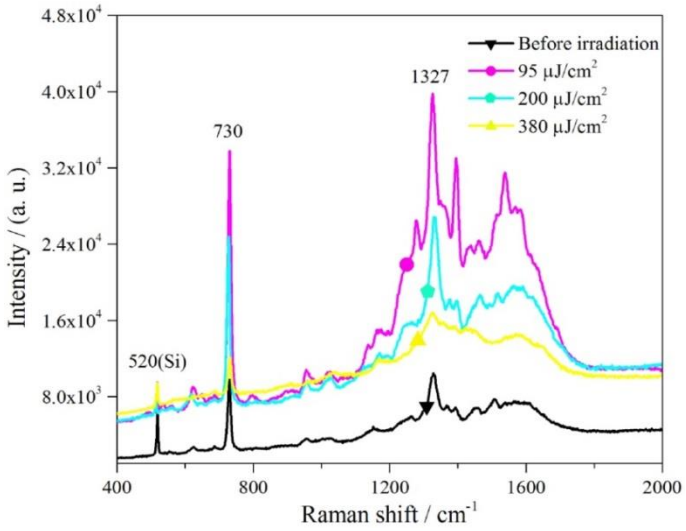

Fig.4-14, SERS spectra of adenine solution (1 mM) absorbed on the surface of Ag NPs.

The role of the α-C:H film in producing enhancement of the SERS signal is probably twofold: the first effect is to separate the Ag NPs by a small amount, while a secondary effect may be the facilitation of active adsorption sites at the surface of Ag NPs. It is also worth noting that, in addition to strong SERS enhancement, the formation of carbon shells on the surface of NPs may inhibit metal-molecule interactions and reduce sensitivity of NPs to photochemical damage [94]. As a result, the presence of α-C:H bridges between Ag NPs, and the fact that the properties of such systems can be tailored through exposure to fs laser pulses, opens up many new possibilities for the application of these materials in nano-structured SERS devices.

4.5 Summary and concluding remarks

Under high fluence fs laser irradiation, it is shown here that complex-shaped core-satellite sub-micron and micron-sized structures can be synthesised by focusing a high intensity fs

laser beam into an aqueous solution of Ag NPs. By adjusting the concentration of NPs in the solution (0.01-0.05 mM), the irradiation time (20-60 min), and the laser fluence (1.8-10.5 J/cm^2), it is feasible to control the sizes and shape of the resulting structures. For example, at a pulse fluence of 10.5 J/cm^2, well dispersed 160 nm and 1480 nm particles were produced in the 0.05 mM solution after 40 and 60 min of irradiation, respectively. These complex plasmonic structures have potential applications as single particle detectors for biomolecules at low concentration. SEM and UV spectra analysis together with the FDTD simulation, suggest that the formation of submicron structure is directed by LSP-induced hotpots.

Under low fluence laser irradiation, it is found that, by adjusting the fs laser pulse fluence during irradiation of PVP coated Ag NPs in aqueous solution, it is feasible to control the separation and bonding within networks of Ag NPs. The primary effect at low fluence ($\approx$ 95 μJ/cm^2) is the generation of an α-C:H coating on individual Ag NPs as a result of the decomposition of adsorbed PVP. It is shown that the decomposition of PVP is due to the impact of electrons or ions emitted from the surface of the irradiated NPs. At higher fluences (typically between 200 and 380 μJ/cm^2), the effect of electron or ion impacts from the hotspots between the adjacent Ag NPs is large enough to remove some of the α-C:H layer and weaken the Ag lattice structure, producing local welding of the NPs. The narrowest gaps between separated Ag NPs (< 1 nm) are found in non-welded samples irradiated at low fluence. A SERS study of Raman spectra of adsorbed adenine indicates that Ag NPs joined by narrow α-C:H shell possess much higher SPR enhancements than welded or single NPs.

Chapter 5 Gathering and Joining of Silver Particles on Silicon Wafer by Femtosecond Laser Radiation

5.1 Introduction

In the process of joining or assembling nanomaterials into nanodevices, precise fabrication of the nanomaterial is usually required; that is because the properties of the nanodevices are very sensitive to in the nanomaterials' geometry [64] and their orientation. Localized fabrication is a promising way to achieve this goal. Recently, a variety of localized nanojoining methods including high energy electron beam radiation [35], ultrasonic nanowelding [28], and nanosoldering [32] have been developed. However, these techniques are limited by the high cost of high energy electron beam systems, the intrinsic complexity of the nanosoldering system and low fabrication efficiency.

The localization of LSP-induced effects such as enhancement of the optical gradient force [70] as well as site-specific heating [67] and ablation [73] can restrict the process area in nanomaterials, facilitating localized fabrication. The use of fs laser radiation is an ideal tool, because its "non-thermal" characteristic can produce highly localized structural transformations in nanomaterials as a result of strong plasmonic enhancement. Some efforts at controlling fs laser induced joining of Ag NPs in aqueous solution by controlling LSP enhanced optical gradient force have been discussed in chapter 4. However, there are still some difficulties in obtaining completely localized joining, due to the random motion of NPs in an aqueous solution. Limiting the NPs' random motion by depositing NPs on a substrate is then an alternative way; and the localized joining of NPs may be achieved by controlling another two LSP-induced effects including the localized heating and ablation/re-deposition.

Considering the fact that most NPs especially those with specific geometries are usually coated by polymer protective layers, and that these polymers on the surface of NPs will affect the joining process as reported in chapter 4, the feasibility and mechanism of locally joining both PVP-coated and bare Ag NPs by utilizing fs laser radiation are studied in this section.

5.2 Gathering of PVP coated Ag NPs

5.2.1 Experimental and simulation setup

The Ag NPs films, which were prepared by the method as described in chapter 3, were irradiated for up to 60 sec with fs laser pulses at average fluence ranging from ~ 3.6 mJ/cm^2 to 28.8 mJ/cm^2. The schematic for the experimental setup is shown in Fig.5-1. The morphology of the Ag NPs films before and after laser irradiation was characterized by SEM and TEM. FDTD software was used to simulate the distribution of hotspots in plasmonic Ag NPs structures during irradiation with 800 nm laser light.

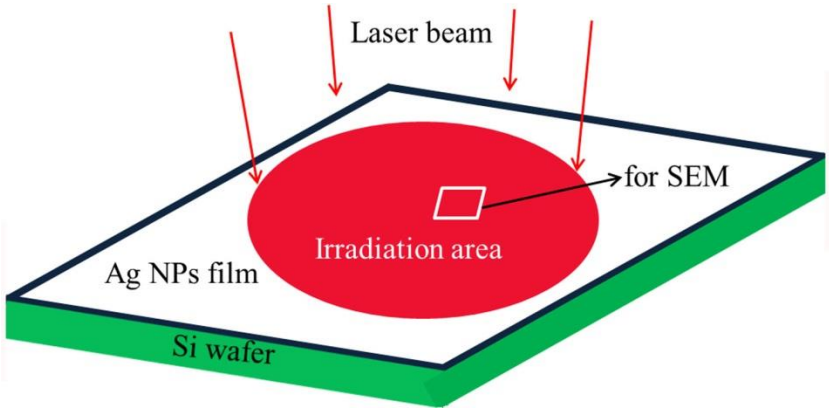

Fig.5-1, Schematic for the experimental configuration

5.2.2 Morphology study

The SEM images of the morphology for Ag NPs film before and after laser irradiation are shown in Fig.5-2. Due to the nature of the deposition process, these films had a non-

uniform thickness distribution. At their thickest point, the films contained ~ 6 layers of Ag NPs. Figs.5-2a and 2b show that, before irradiation, most of the individual NPs in these films had sizes between 20-80 nm with an average size of 50 nm. Individual NPs were irregularly shaped as shown in the inset in Fig.5-2a. After irradiation for 10 sec (10,000 pulses), at laser fluence ~7.2 mJ/cm^2 some spherical particles were generated, as indicated by the dashed circles in the inset image in Fig.5-2c. The size distribution of these newly formed spherical particles, measured over 300 particles, is given in Fig.5-2d. It can be seen that large spherical particles having diameters between 80-160 nm appeared after 10 sec laser irradiation. Particles in this size range were not present before irradiation. The generation of larger spherical particles suggests that fs laser irradiation under these conditions produce efficient heating which causes the melting and subsequent coalescence of the original Ag NPs. Molecular dynamic simulations and experimental observations of the solid-state sintering behavior of NPs has shown that sintered NPs will not grow into larger sphere-like structures until the sintering temperature approaches the melting point [113, 114]. No apparent change was observed in the morphology and size of these generated spherical particles, when the irradiation time was increased to 30 and 60 sec. As shown in Fig.5-3, the size of the large spherical particles was still in the 80-160 nm range after the NP film was irradiated at a fluence of ~ 7.2 mJ/cm^2 for 30 sec (Figs.5-3a and 3b) and 60 sec (Figs.5-3c and 3d). This indicates that the generation of spherical particles does not depend on the irradiation time and implies that other factors such as laser fluence and the localized structure in the NP film may dominate the interaction.

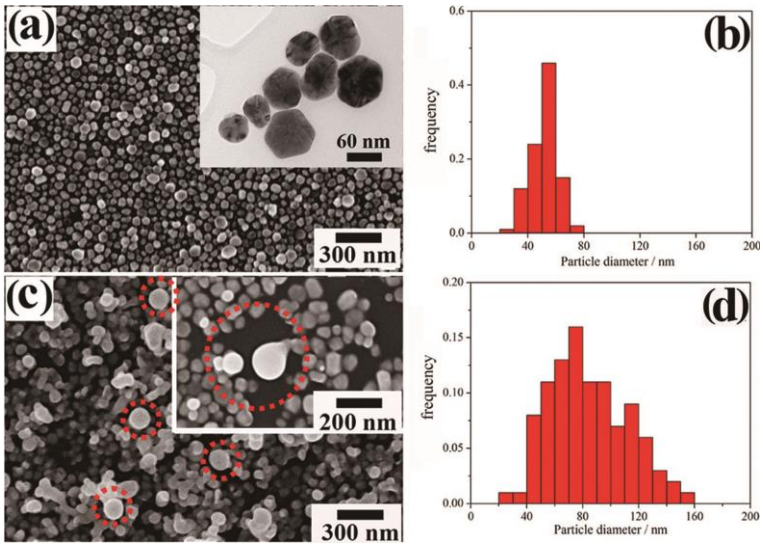

Fig.5-2, SEM and TEM images of morphology for Ag NPs films on a Si wafer before and after irradiation, (a) SEM image of NP film before irradiation, the inset TEM image shows the details of the NPs; (b) size distribution of the NPs in the film before irradiation; (c) SEM image of the NP film after irradiation at a fluence 7.2 mJ/cm^2 for 10 s (10.000 pulses), the inset image shows the formation of larger spherical nanoparticles; (d) size distribution of the larger spherical particles in the film after irradiation.

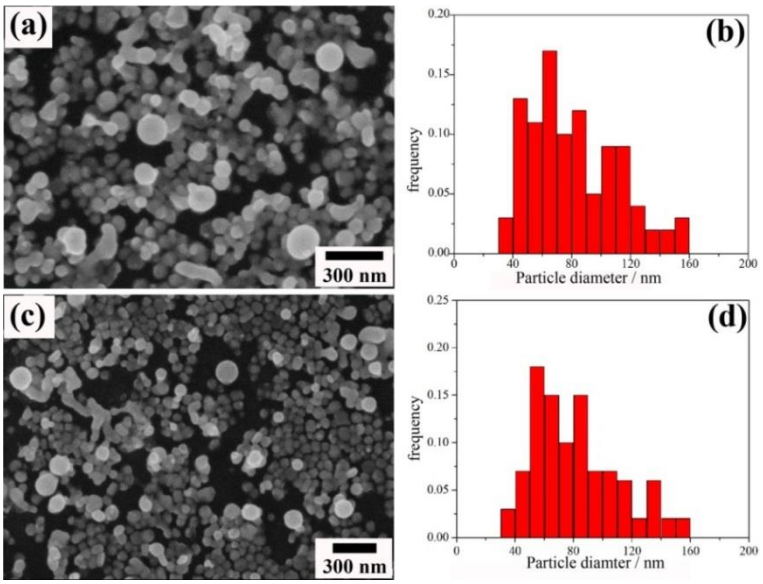

Fig.5-3, SEM morphology and size distribution of generated spherical particles in the NPs films where were irradiated by fs laser at fluence ~7.2 mJ/cm^2 for 30 and 60 sec. (a-b) 30 sec, (c-d) 60 sec.

Fig.5-4 shows SEM images of the morphology for Ag NPs in the film which was irradiated at different fluences for 10 sec. At 28.8 mJ/cm^2 (Fig.5-4a), the NPs in the irradiated film were melted and sintered due to the large energy input, and the Si wafer showed the development of small holes (see the arrows in Fig.5-4b). These holes were the result of

ablation. Since this fluence is much smaller than the damage threshold in Si (170 mJ/cm^2) irradiated with a 25 fs pulse [115], hole drilling in the Si wafer can be attributed to an enhancement in the local laser intensity as a result of multiple scattering [116]. At a laser fluence ~ 14.4 mJ/cm^2, spherical particles were also obtained and the size distribution of these spherical particles was almost the same as that in samples irradiated at a fluence approximately 7.2 mJ/cm^2. The only exception was that a few slightly larger (160-220 nm) particles were also generated (Figs.5-4c and 4d). When the laser fluence was decreased to 3.6 mJ/cm^2 (Fig.5-4e), modification was not evident in the irradiated NP films. These observations indicate that the generation of spherical particles is influenced by the laser fluence, but there is no direct correlation between laser fluence and the resulting size of the spherical particles.

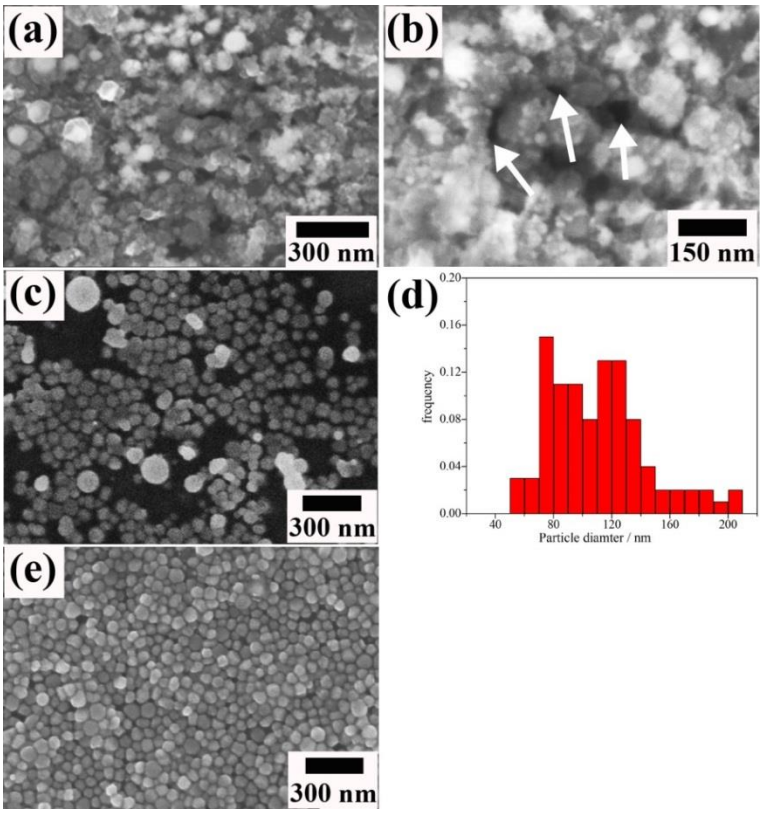

Fig.5-4, SEM images of the morphology and size distribution of generated spherical particles in the NPs films which were irradiated by fs laser at different fluences for 10 sec. (a-b) 28.8 mJ/cm^2, (c-d) 14.4 mJ/cm^2, (e) 3.6 mJ/cm^2.

5.2.3 Investigation of formation mechanism

To understand how these spherical particles with a particular size distribution were generated, Ag NPs films which were irradiated by fs laser at fluence 7.2 mJ/cm^2 were selected for further study. As discussed above, the formation of larger size spherical particles was caused by the melting and gathering of the irradiated Ag NPs. Here, enhancement in the local laser intensity due to multiple scattering, including speckle formation and sub-wavelength self-focusing [115], was first considered as the origin of efficient heat generation leading to the melting of Ag. This might be expected to be important in multiple-layer Ag NP films, and has been observed in previous studies and the present experiment (Fig.5-4b). For example, sub-wavelength self-focusing of an incident laser beam was observed at the bottom surface of a multiple layer ZnO NP film [115]. The laser intensity in the self-focused beam was enhanced by a factor of 2.5. In the present experiments, the enhancement factor was estimated to be ~ 6. This value was obtained from the ratio of the fluence (~28.8 mJ/cm^2) consistent with producing visible damage to the Si substrate in the present experiments to that reported as the damage threshold (170 mJ/cm^2) for irradiation of Si with a 25 fs pulse [115]. Based on this comparison, one can come to conclusion that sub-wavelength self-focusing is not the primary source of the efficient heating and melting of NPs found in the present experiments as discussed in section 4.4.

To minimize the influence of sub-wavelength self-focusing, and to investigate the underlying causes of efficient fs laser induced localized heating, single-layer Ag NPs films were prepared and irradiated under the same conditions. Fig.5-5 shows SEM images of the morphology for single-layer NPs films before and after 16 laser pulses, which was the

minimum number of overlapping pulses needed to produce an observable change in the single layer Ag NP film. These images show that larger spherical NPs can also be generated in single-layer NPs films after fs laser irradiation (as indicated by arrows in Fig.5-5b). This implies that multiple scattering induced sub-wavelength self-focusing was not the source of the efficient heating effect resulting in melting of the original NPs. SEM observations in the same area of the NPs film before (Fig.5-5a) and after (Fig.5-5b) fs laser irradiation showed that, a large spherical particle was created in the structure where 4 NPs were located (ring 1 in Figs.5-5a and 5b). This particle is shown in the inset image of Fig.5-5b. Removal of NPs from the PVP matrix leaved and outlined their original positions (eg. ring 2 in Fig.5-5b). The inset image in Fig.5-5b indicates that 3 of the 4 adjacent Ag NPs coalesced into a larger particle while the remaining NP was unaffected. This suggests that selective fs laser-induced heating of Ag NPs is concentrated in certain structures where the absorption of laser energy is enhanced, and that this heating occurs without apparent damage to the NPs surrounding these structures. It is consistent with the observation that spherical particles with diameters of ~ 76, 83 and 100 nm were located close to the structures in which 3, 4 and 7 NPs were absent after laser irradiation (dashed rings in Figs.5-5c, 5d and 5e, respectively). The number of Ag NPs removed was estimated from the SEM images (Fig.5-5). The area, S, of the removed structure is $S=(1/f)N\pi r^2$ where f is the filling factor for the NPs in the structure, N is the number of NPs, and r = 25 nm is the average NP radius. Volumes calculated for the resulting spherical particles correspond almost exactly to the sum of the volumes of the particles removed from the PVP matrix. The removal of Ag NPs is likely due to fs laser irradiation induced ablation of the NPs and/or the PVP shell around these particles [73, 117, 118]. It should be

noted that ions/electrons produced in the initial stages of the ablation process can increase the absorption of fs laser energy [119, 120], leading to enhanced heating of the NPs.

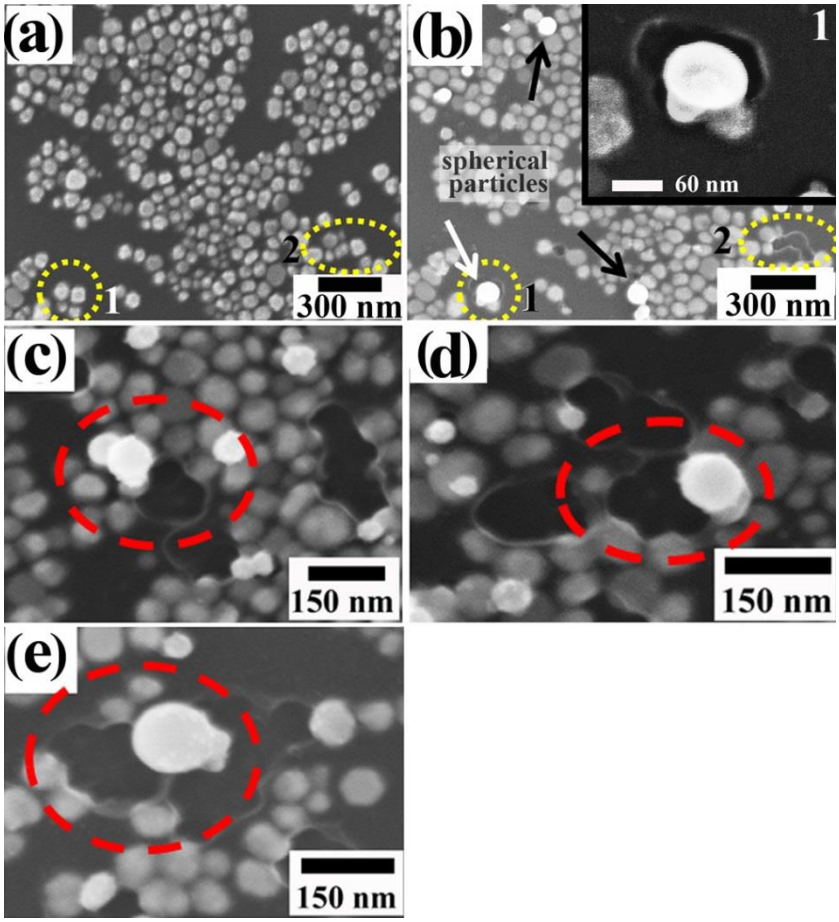

Fig.5-5, SEM images of the morphology for single layer NP films before and after irradiation with 16 fs laser pulses at 7.2 mJ/cm^2. (a) before irradiation; (b) after irradiation of film in (a). The arrows show the generation of spherical particles while the double-ended arrow in the inset image shows the direction of the laser polarization. The dashed rings 1 and 2 show the area where NPs were ejected, and the inset image shows a magnified view of the circular area 1; (c, d, e). spherical particles generated near NP assemblies containing 3, 4 and 7 NPs.

Another characteristic of the laser-matter interaction is that Ag NP dimers whose long axis was parallel to the direction of laser polarization (as indicated by the double ended arrows in Fig.5-6) tended to be removed from the PVP matrix. Individual isolated NPs were not removed under these conditions (Fig.5-5 and Fig.5-6). This effect and the dependence on laser polarization and local structure are similar to the polarization-dependent generation of

LSP-induced hotspots. This suggests that the efficient heating of NPs in these films can be attributed to LSP-induced hotspots.

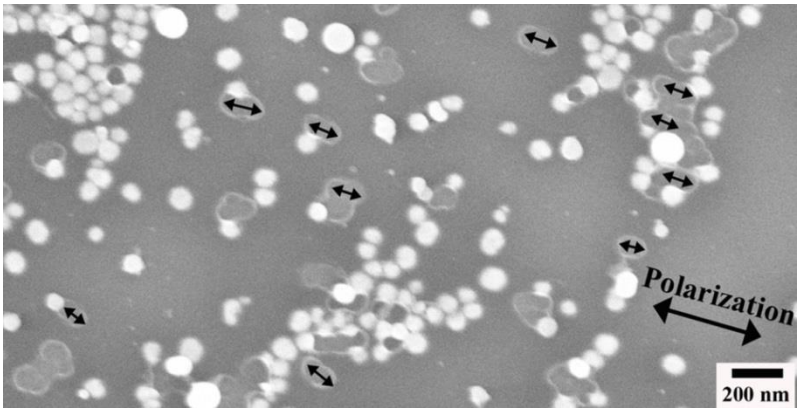

Fig.5-6, Laser polarization dependent ejection of NP dimers in a single layer NP film after irradiated by 16 fs laser pulses at a fuence of 7.2 mJ/cm^2. The double ended arrows show the long axis of the NP dimer.

FDTD simulations have been carried out to identify the location of hotspots in Ag NPs structures containing 2, 3, 4 and 7 NPs as indicated by the SEM observations (Fig.5-5), and to study the effect of LSP-induced hotspots on the heating of NPs and the formation of larger spherical particles in specific structures. Aggregates containing 5 and 6 NPs are not considered, because they are not close-packed structures and are rarely seen in the Ag NP films. A schematic for the simulation geometry is shown in Fig.5-7a, where Ag NPs are supported on a Si wafer with 2 nm thick oxide layer. For simplification, all the NPs were taken to be spherical with a diameter of 50 nm and the irradiation occurred in air. The gap distance between adjacent NPs was set to be 8(±2) nm which was an average value of gap distance from 200 measurements using SEM images. The distribution of hotspots in the XY plane at the half height of the NP was recorded in the simulations. Fig.5-7 shows the calculated hotspot distribution in a variety of structures. These are indicated by the bright red and yellow regions, while the bold dark red rings outline the NPs. It is evident (Fig.5-7b) that the maximum enhancement factor (E_1^2/E_0^2, ~10) in the hotspots in single

NPs occurs in the direction of the laser polarization. The same enhancement factor (~10) is seen in an Ag NPs dimer when the laser polarization is perpendicular to the long axis (Fig.5-7c). The low electric field enhancement in these hotspots is consistent with reduced laser induced heating and emission of electrons and ions from the NPs and the PVP shell, and with the observation that isolated single NPs or NPs dimers with their long axis perpendicular to the laser polarization direction were not removed from the irradiated PVP matrix (Fig.5-6).

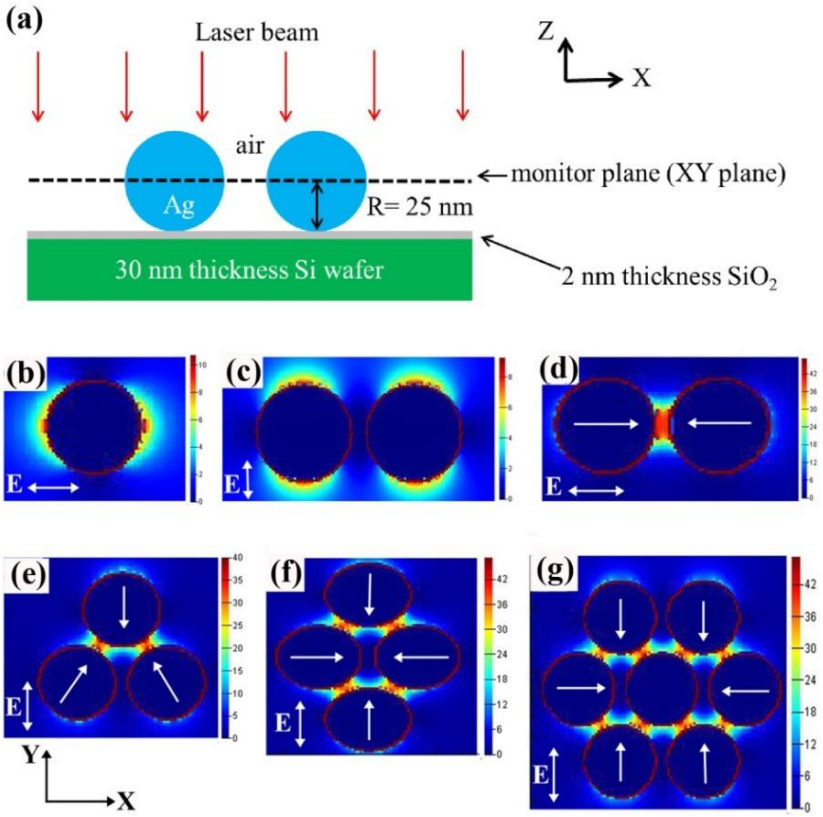

Fig.5-7, Simulated electric field distribution in Ag NPs structures assembled from 50 nm NPs. (a) Schematic of simulation setup, a dimer structure is taken as an example; (b-g) hotspots distribution in Ag NPs structures with different number of particles, the enhancement factor in the scale bar is defined as E_1^2/E_0^2. The hotspots are located in the bright red and blue area. The double-end arrows show the electric field direction of the incident laser. The single-end arrows show the proposed motion of NPs. The gap between the NPs is set to be the measured average distance of 8 nm.

These simulations indicate that the field enhancement factor (~ 40) is much greater in Ag NP dimers with their long axis parallel to the direction of laser polarization (Fig.5-7d). As

proposed by Xu *et al.* [70], the effect of this enhancement is to cause the NPs to move towards each other. The attractive force is shown with single ended arrows in Fig.5-7. This attraction facilitates the gathering of NPs and initiates the formation of larger spherical particles. The electric field enhancement and the proposed motion of the NPs in other structures are shown in Figs.5-7e, 7f and 7g.

To determine how the presence of hotspots may contribute to the efficient heating of NPs via enhanced laser energy absorption, the minimum absorption efficiency, Q_{abs}, that must be achieved to reach the melting temperature is estimated by using equations where $Q_{abs} = {E_{abs}}/{E_{inc}}$ and $E_{abs} = N\left[\frac{4}{3}\pi r^3 \rho(C\Delta T + H_m)\right]$. $E_{inc} = FS$ is the total laser energy incident on the structure, where F = 72 J/m^2 is the laser fluence and S is the effective absorption area of the structures as outlined in Fig.5-6. E_{abs} is the energy required to completely melt the Ag NPs in a structure containing N NPs, while r is the NP radius, ρ is the density, C is the heat capacity, V is volume and H_m is the latent heat of fusion. Taking r = 25 nm for an Ag NP, ρ=1.0x10^4 kg/m^3, C=230 J/(kg•℃) and H_m=1.05x10^5 J/kg, it is found that the minimum absorption efficiency, Q_{abs}, required to produce melting (ΔT=940 ℃) in these structures is > 0.7. The maximum temperature that the particle can reach is estimated to be 993 ℃ if all the incident laser radiation is absorbed. Depression of the melting temperature is not considered here because this is not significant for 50 nm Ag NPs [2, 121]. High absorption efficiencies (> 0.7) for NPs as calculated above are usually only obtained when the LSP of the structure is in resonance with the incident laser polarization and wavelength [5]. However, the measured absorption spectrum (Fig.5-8) clearly shows that no resonance occurs at 800 nm in the Ag NP structures at low incident

intensity. This is also supported by the calculated absorption spectrum based on the FDTD simulation (inset in Fig.5-8). Some differences between the experimental and calculated spectrum are observed at wavelengths near 550 nm. This difference likely arises because the NPs in the simulation were assumed to be spherical and embedded in air, while in reality the NPs are irregular and are coated with a ~2 nm thick PVP layer. The temperature rise in individual NPs is estimated in the usual way based on the measured absorbance (=0.1 at 800 nm wavelength). Then $0.1 = ln(I_0/I)$, where I_0 is the incident light intensity and I is the intensity of the light after passing through the NP film. The measurements show that the absorption efficiency is < 0.1 which is much smaller than the minimum absorption efficiency ~ 0.7 required to produce melting. As a result, the temperature rise of the NPs is < 140 ℃ which is much lower than the melting temperature of Ag. This shows that the observed efficient heating and melting of Ag NPs is not primarily due to the LSP resonance itself, but likely occurs because of enhanced absorption arising from increased excitation of ions and electrons produced from the decomposition of PVP or ionization of air on the surface of Ag NPs in the vicinity of hotspots as reported previously [119, 120, 122]. However, the generation of the LSPs is important in the initial stages of the laser NP interaction, as LSP induced hotspots act to facilitate and enhance coupling of fs radiation into these structures.

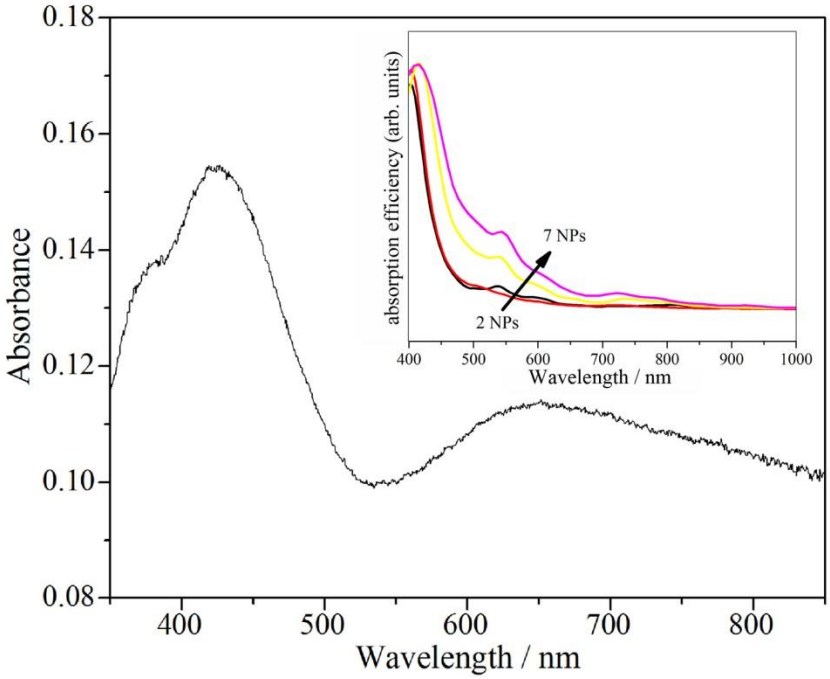

Fig.5-8, Absorbance spectra of Ag NPs film, the inset image is the calculated absorption cross-section of the structures containing 2, 3, 4, 7 NPs.

To investigate the possible contribution of PVP and air to the heating effect, the Ag NP film was irradiated by fs laser in a high vacuum (6.6 x 10^{-7} Torr). The results (Fig.5-9) show that larger size spherical particles could still be obtained and their size distribution (80-180 nm) did not evidently change compared to those irradiated in air. This suggests that the contribution of air to the enhanced heating is not the dominant factor under the present experiment condition. However, the role of PVP is still not clear, as there is still no effective way to prepare un-aggregated Ag NPs films by completely removing the PVP protective layer on the surface of Ag NPs. So in the following section, fs laser irradiated bare Ag particles which are produced by laser deposition in vacuum are studied. This will be helpful to identify the role of PVP in fs laser irradiation process.

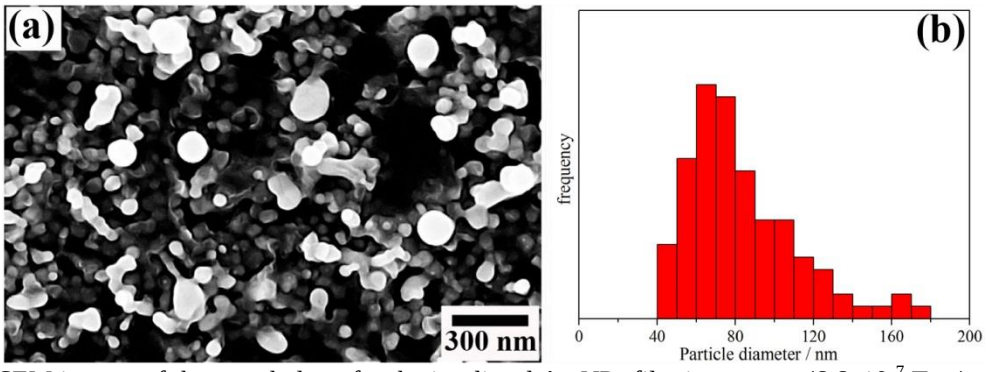

Fig.5-9, SEM images of the morphology for the irradiated Ag NPs film in vacuum ($6.6x10^{-7}$ Torr) at fluence 7.2 mJ/cm^2 for 10 sec (a), and size distribution of the generated spherical NPs after laser irradiation (b).

5.3 Localized joining of bare Ag Submicron/Nanoparticles

5.3.1 Experimental and simulation

Ag submicron/nanoparticles were deposited on a Si wafer by fs laser irradiation as described in chapter 3. After deposition, the Ag particles on the surface of Si were then irradiated using the same fs laser at fluences ~ 900 μJ/cm^2 or 1300 μJ/cm^2 for up to 90 sec. Both the ablation/deposition and irradiation/joining operations were carried out in vacuum at a base pressure of ~10^{-6} Torr. The morphology of selected Ag particles before and after laser irradiation was compared using SEM and high magnification images of welded structures were obtained using TEM. FDTD software was used to identify the electric field enhancement in the Ag particles which were irradiated by laser at 800 nm.

5.3.2 Joint morphology study

Fig.5-10 shows the SEM images of the morphology for deposited Ag submicron/nanoparticles before and after 50 sec laser irradiation at a fluence of approximately 900 μJ/cm^2. Comparison of these images shows that laser irradiation did not change the position of the deposited Ag particles, although the particles were slightly ablated (see the larger particle in the inset image of Fig.5-10b).

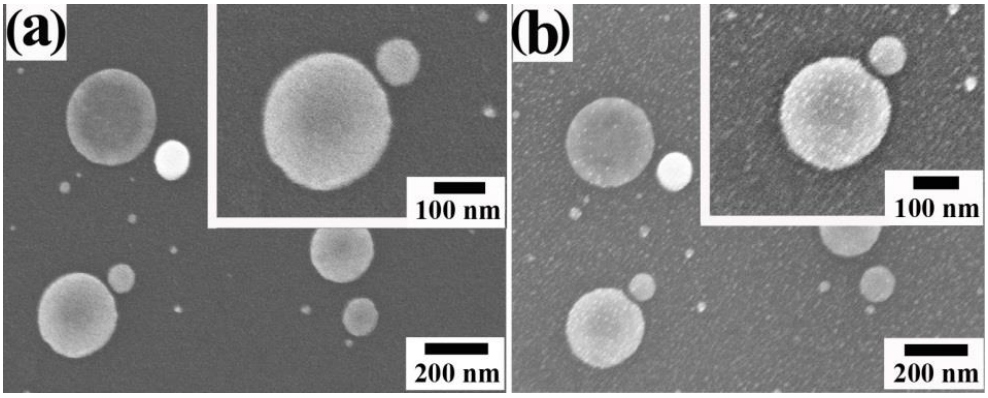

Fig.5-10, Scannng electron microscopy (SEM) images of the morphology of deposited Ag particles before and after fs laser irradiation at a fluence ~ 900 μJ/cm^2 for 50 sec. (a) before irradiation; (b) same area after irradiation. The inset images are magnified view.

Under the same irradiation conditions, some closely-spaced Ag particles (~ 30 nm separation) became welded together (Figs.5-11a and 11b); while there was no apparent damage to these particles apart from a slight change in morphology near the weld area. Since the particles did not move during the irradiation process, welding occurs as the result of material filling the small gap between the particles. This is shown in the inset images of Figs.5-11a and 11b where two separated particles were seen to be interconnected by filler material, forming dumbbell shaped structures. This filler material originated from ablated Ag material (the inset image of Fig.5-10b) due to LSP-induced hotspots in the vicinity of the gap between the particles, as reported in a previous study [123]. This ablation is clearly observed in the welded Ag particles (see the left particle in Figs.5-11c and 11d) when the samples were tilted by 75 ° for clearer observation. Figs.5-11c and 11d also show that the area below the weld did not contain filler material implying that the weld was formed by highly directional deposition of the ablated material. Similar welded NPs structures were also observed when the irradiation time changed to 10 sec or 90 sec, as shown in Fig.5-12.

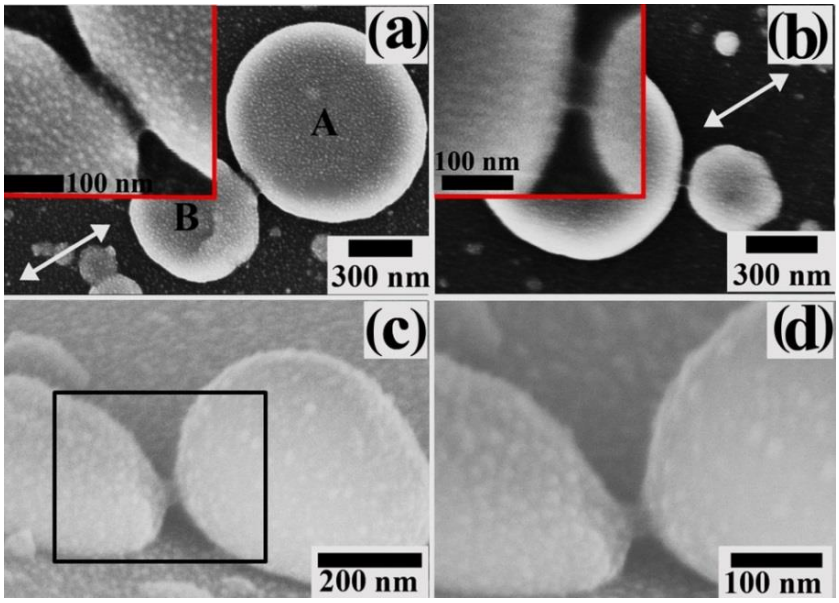

Fig.5-11, SEM images of the morphology of deposited Ag particles after fs laser irradiation at a fluence of ~ 900 mJ/cm^2 for 50 sec. (a-b) welded Ag particles afer irradiation, the double ended arrows show the direction of laser polarization, and the inset images show a magnified view of the joint; (c) view of welded Ag particles after tilting by 75 º; (d) magnified view of the square area in figure (c).

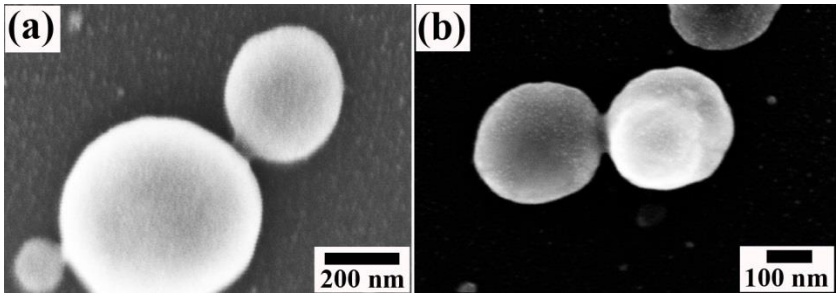

Fig.5-12, SEM images of the morphology for the NPs irradiated by fs laser at fluence 900 uJ/cm^2 for different time. (a) 10 sec, (b) 90 sec.

The cross-sectional morphology of welded Ag particles has been analyzed using TEM. Samples were prepared from selected pair of submicron particles (Fig.5-13a) by etching with a focused ion beam. It is evident that the bottom surface of the deposited Ag submicron particles pair has been flattened, forming disc-like structures with a diameter/height ratio of ~ 3.7 (Figs.5-13a and 13b). In some cases, the deposited Ag submicron particle could form donut structures, as shown in Fig.3-6a. This is similar to the structure obtained in splat cooling [124, 125], suggesting that Ag particles ablated from the

sputtering target were in a softened or molten state [124, 125] as they travelled at high speed prior to impacting on the Si wafer surface. As in splat cooling, quasi-liquid or liquid particles solidify immediately on reaching the surface of the Si wafer. Studies have shown that when Ag particles were deposited on a carbon film under the same conditions, and then irradiated with fs laser pulses with the same fluence (~2.7 mJ/cm^2), adsorbed particles were ejected from the surface due to the dewetting between Ag and carbon [126]. This was not seen when Ag particles were deposited on a Si wafer, implying that the Ag particles bonded to the Si wafer during deposition. HRTEM scans at the interface between the Ag particle and the Si wafer (Fig.5-13c) show that bonding occured in the contact area between the Ag particle and the ~ 3 nm thick amorphous native oxide (SiO_x) layer [127] on the surface of the Si wafer. HRTEM analysis also shows (Fig.5-13d) that the Ag(111) lattice planes in both particles were aligned across the junction.

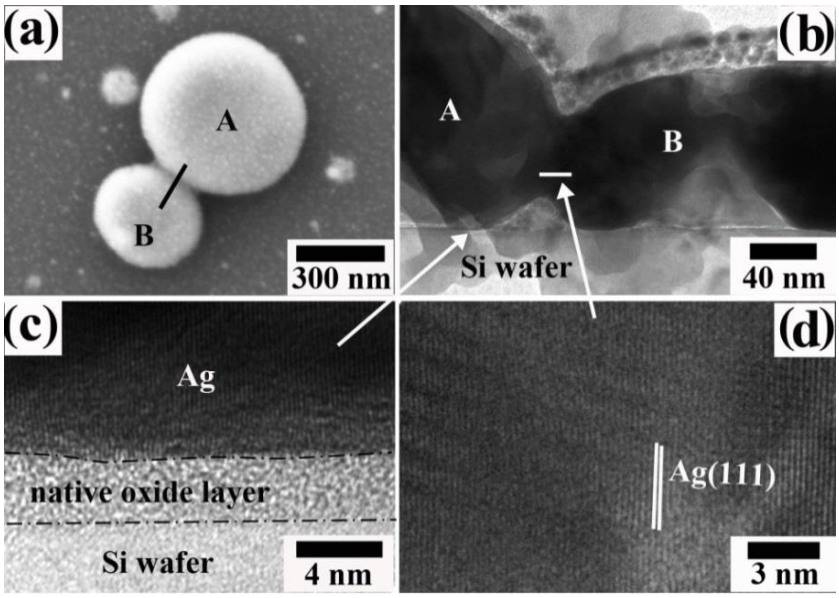

Fig.5-13, Morphology of a pair of welded Ag particles. (a) SEM images; (b) TEM image of the cross-sectional view of the Ag pair in (a) along the the black line; the small particles on the top of particles A and B are re-deposited material as a result of the TEM sample preparation process; (c) HRTEM image of the Ag-Si wafer interface; (d) HRTEM image of the weld between the two Ag particles. The arrows indicate the corresponding area of the HRTEM images in figure (b).

5.3.3 Investigation of joining mechanism

Figs.5-11a and 11d show that interconnection between the two particles was generated by the formation of a bridge comprising filler material from ablated submicron particles. This ablation can be attributed to LSP-induced hotspots which are accompanied by localized electron and ionic emission [73]. To investigate the possible contribution of this localized emission to the formation of the interconnection, FDTD calculations (Fig.5-14) have been used to simulate the hotspots distribution near and in between a pair of Ag submicron particles.

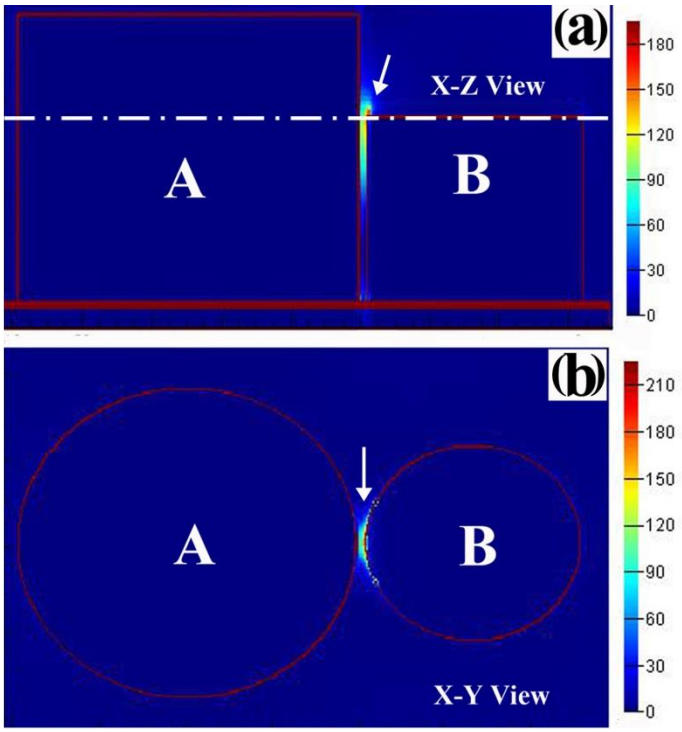

Fig.5-14, Simulated hotspots distribution in two adjacent Ag particles as observed in figure 2a. (a) view of the X-Z plane crossing the axes of the two particles; (b) view of the X-Y plane at the same height in particle B, as indicated by the dashed line in (a). The arrows show the locations of the hotspots, the enhancement factor in the scale bar is defined as E_1^2/E_0^2.

The two-particle structure shown in Fig.5-11a is selected as representative, and both particles A and B are assumed to be discs having a diameter/height ratio of 3.7. This geometry approximately relplicates that seen in the TEM scans. The incident laser beam

with a wavelength of 800 nm is normal to the Si wafer which supports particles A and B, and the angle between the laser polarization and the axis of the particle pair is the same as that in the experiment. The simulation results show that a hotspot with an electric field enhancement factor (E_1^2/E_0^2) ~ 180 appeared between the two discs (Figs.5-14a and 14b) close to the top edge of the lower disc (Fig.5-14a). This simulation is in good agreement with the experimental observations (Fig.5-11), implying that LSP-induced hotspots facilicate the interconnection of pairs of Ag particles.

Extensive studies have shown that the generation of hotspots arising from LSP produced localized ablation and electron/ion emission from the particles, and that the material ablated from the particles re-deposited near the ablated surface within the hotspots [126]. This re-deposition of ablated material can gradually reduce the gap distance between the particles resulting in the formation of an interconnecting link. In the present case, the electic field enhancement factor is ~ 13.4 giving a root square enhancement factor of ~ 180, corresponding to the presence of a local electric field E of $5x10^9$ V/m near the surface of the Ag particle. This field is close to the measured threshold for field ion emission [127], suggesting that ions can be emitted from the Ag particles under the effect of LSP-induced hotspots. These ions then contribute to the formation of an interconnection between the particles and facilitate the welding process.

The laser fluence was then increased to ~ 1300 $\mu J/cm^2$ in order to mimic the enhancement that occurs in LSP-induced hotspots, and identify the contribution of enhanced ablation (ionic emission) at hotspots to the joining of particles. Fig.5-15a shows the SEM images of the morphology for freshly deposited Ag submicron/nanoparticles. These images reveal that the surface of these particles was almost smooth prior to irradiation. Particles labeled

1 and 2 are seen to be closely separated. After these particles were irradiated for 50 sec by fs laser pulses at a fluence of 1300 $\mu J/cm^2$ (Fig.5-15b), the particle morphology was seen to change and the surface became rough, indicating that ablation of the particles occurred under these conditions. Emitted material was also seen to form a bridge between the two particles 1 and 2. This suggests that the electric field enhancement in the hotspots facilitates the generation of a weld between adjacent Ag particles. It should also be noted that, under fs laser irradiation, the isolated particles tended to be ablated at the two poles in the direction parallel to the laser polarization. Ablated material from these locations re-deposited at the poles of the particles (see particle 3 in Fig.5-15b). The location of the ablated area in these particles is consistent with that of LSP-induced hospots [73], indicating that laser induced hotspots selectively enhanced ablation of the particle. This is apparent in the SEM scan of the sample after rotation by 90 ° followed by further irradiation by fs laser pulses for another 50 sec at the same fluence. The SEM image (particle 3 in Fig.5-15c) clearly shows that, when the sample was rotated by 90 °, the ablated area appeared at the other poles whose direction was parallel to the laser polarization. This direction is perpendicular to that of the previous poles. In particle 1 and particle 2, the dependence of ablation on laser polarization is minimized because the influence of the gap distance between them dominates over the polarization on LSP-induced hotspots. This confirms that LSP-induced hotspots generated by fs laser irradiation contribute to localized ablation of the particle and then to the interconnection produced between two adjacent particles.

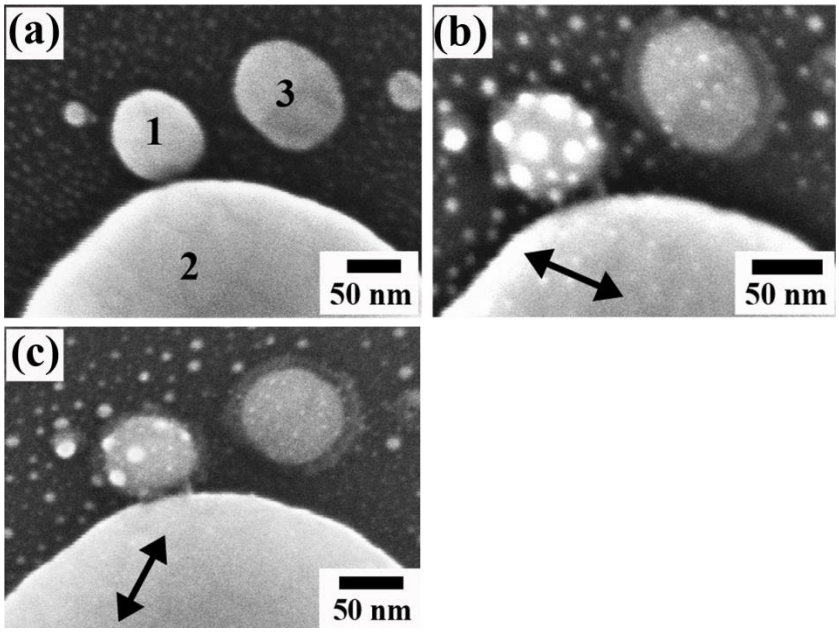

Fig.5-15, Development of joint between two Ag particles under fs laser irradaition at a fluence ~1300 μJ/cm^2. (a) Ag particles before irradaition; (b) same Ag particles after 50 sec laser irradiation with polarization (double-ends arrow) shown; (c) same Ag particles after another 50 sec laser irradiation with the polarization direction perpendicular to that in (b).

It is significant that, due to the use of low fluence combined with the ″non-thermal″ nature of the fs laser-matter interaction, the irradiated particles were virtually unaffected and had no apparent damage after welding (Figs.5-11 and Fig.5-15). This suggests that fs laser irradiation is a promising technique for precision fabrication in the ″non-destructive″ interconnection of submicron/nanodevice parts for applications in nanoelectrics. However, it is noted that, under low fluence fs laser irradiation, the allowable separation distance between two pre-joined particles for achieving joining has to be controlled to a very small value (usually < 40 nm); it will probably limit the application of fs laser in "non-destructive" interconnection. This issue is then the main topic of chapter 6.

5.4 Summary and concluding remarks

In this work, it is shown that PVP coated Ag NPs in specific symmetric plasmonic structures can be efficiently heated up to their melting point and gathered into larger size

spherical particles when irradiated with very low fs laser fluence (~7.2 mJ/cm^2). The first stage in this process, which involves the selective gathering of several nanoparticles prior to bonding, is also of interest as a potential method for the further assembly of functional devices. Enhanced coupling and efficient heating was strongly dependent on the geometry of the NPs structures and laser polarization. This selective heating effect and collection of NPs was found to be most evident in clusters of 2, 3, 4 and 7 Ag NPs. FDTD simulations and measured absorption spectra indicate that the efficient heating, melting and collection of NPs in these structures was triggered by LSP-induced hotspots. The overall effect is strongly dependent on the orientation of laser polarization in relation to the symmetry axis of selected structures.

For bare Ag submicron/nanoparticles on a Si wafer, it is shown that the interconnection of two adjacent Ag particles can be achieved without the use of additional filler material. The Ag particles were self-bonded to the Si wafer following deposition by laser ablation. Adjacent Ag particles separated from each other by a small gap were found to be welded together after fs laser irradiation for 50 sec at fluences between ~ 900 and 1300 μJ/cm^2. SEM and TEM scans show that the metallic interconnection linking the particles was generated by the re-deposition of ablated material in the gap between the particles. The integrity of both particles was conserved in this process and the overall damage to the non-bonded component of the Ag submicron/nanoparticles was found to be negligible. FDTD simulation indicates that the ablation of the Ag submicron/nanoparticles and the formation of the interconnection can be attributed to LSP-induced hotspots. This study points the way to the development of a high integrity and location controllable interconnection technique in the fabrication of submicron and nanodevices.

Chapter 6 Oxygen-assisted Interconnection of Silver Submicron/Nanoparticles with Femtosecond Laser Radiation

6.1 Introduction

Joining metallic nanomaterials by utilizing physical methods which usually produce robust metallic bonding is straightforward, but it usually faces the challenge of minimizing the damage to the pre-joined nanomaterials [3, 35, 128]. Recently, the fs laser nanojoining technique exhibits the potential of solving this issue [129]. As discussed in section 5.3 that two adjacent Ag particles (~ 30 nm separation) which were deposited on the Si wafer were interconnected through the re-deposition of locally ablated material by utilizing fs laser irradiation in high vacuum (10^{-6} Torr), while their geometries were almost intact. However, there is still a long way to go before industrial application of this high integrity interconnection technique; the required small separation distance and the needs of high vacuum are two major limitations.

One possible solution is to employ gases to assist the joining process. The role of gas is to improve the absorption of laser pulse energy [119] or enhance heat generation through chemical reaction with the pre-joined materials [130], which consequently accelerates re-deposition process due to the increased amount of locally ablated material. Atomic gases (He, Xe, Ne and H_2) have been reported to efficiently enhance the absorption of laser pulse energy at high intensity (10^{13} ~ 10^{17} W/cm^2) ps laser irradiation condition by forming plasma [119]. In that case, high intensity laser radiation would unavoidably produce thermal damage to the irradiated nanomaterials. This thermal damage can be minimized if LSP is excited in nanomaterials, because in LSP-induced hotspots the required laser intensity to produce the ionization of diatomic gases can be significantly lowered.

Then, the issue comes to how the ionized gases transfer the absorbed energy to the irradiated nanomaterials. The reaction of the ionized gases with the irradiated nanomaterials is one way, and the recombination of ionized gases on the surface of irradiated nanomaterials is another possibility. In this section, the influence of gases (specifically oxygen) on fs laser irradiated Ag particles which were deposited on Si wafer is studied, and the role of LSP in the irradiation process is identified.

6.2 Experimental and simulation setup

After the deposition of Ag submicron/nanoparticles on Si wafer as described in section 2.5, Ag particles on the Si surface were then irradiated by fs laser pulses at a fluence ranging from ~ 2 mJ/cm^2 (corresponding to ~ 5.7 x 10^{10} W/cm^2) to 14 mJ/cm^2 (corresponding to ~ 4 x 10^{11} W/cm^2) for varying times. Different gases (air, nitrogen and oxygen) and pressures (760, 1, 10^{-2} and 10^{-4} Torr) were used to identify the influence of the gases on fs laser irradiated Ag particles. The morphology of the irradiated Ag particles was analyzed by SEM, and the cross-section of joined Ag particles was analyzed with TEM observation of the sample prepared by focused ion beam etching.

6.3 Morphology study of irradiated Ag submicron/nanoparticles

To study the feasibility of obtaining high integrity interconnection of Ag submicron/nanoparticles at pressures other than at high vacuum (10^{-6} Torr) as mentioned above, Ag particles were irradiated by fs laser pulses at different pressures ranging from 1.3x10^{-4} Torr to 760 Torr (atmosphere pressure). The SEM images of the morphology for irradiated NPs show that, at pressures of 1.3x10^{-4} Torr and 1.7x10^{-2} Torr (Figs.6-1a and 1b), Ag submicron/nanoparticles were ablated in the two pole areas which were parallel to laser polarization direction. The size distribution of these ablated particles was located in the

range of 60~150 nm (Fig.6-1c). This can be contributed to hotspots-enhanced localized ablation in the pole areas due to the excitation of LSP [73]. The ablated material then re-deposited nearby, formed "tab-like" structure, and resulted in the extension of the particle in laser polarization direction. The ratio between the length of the "tab-like" structure (*L*) and the particle's diameter (*D*) (*L/D* ratio) is 0.13±0.06 based on 50 counts. This directional extension of Ag submicron/nanoparticles shows the potential of interconnecting well-separated particles.

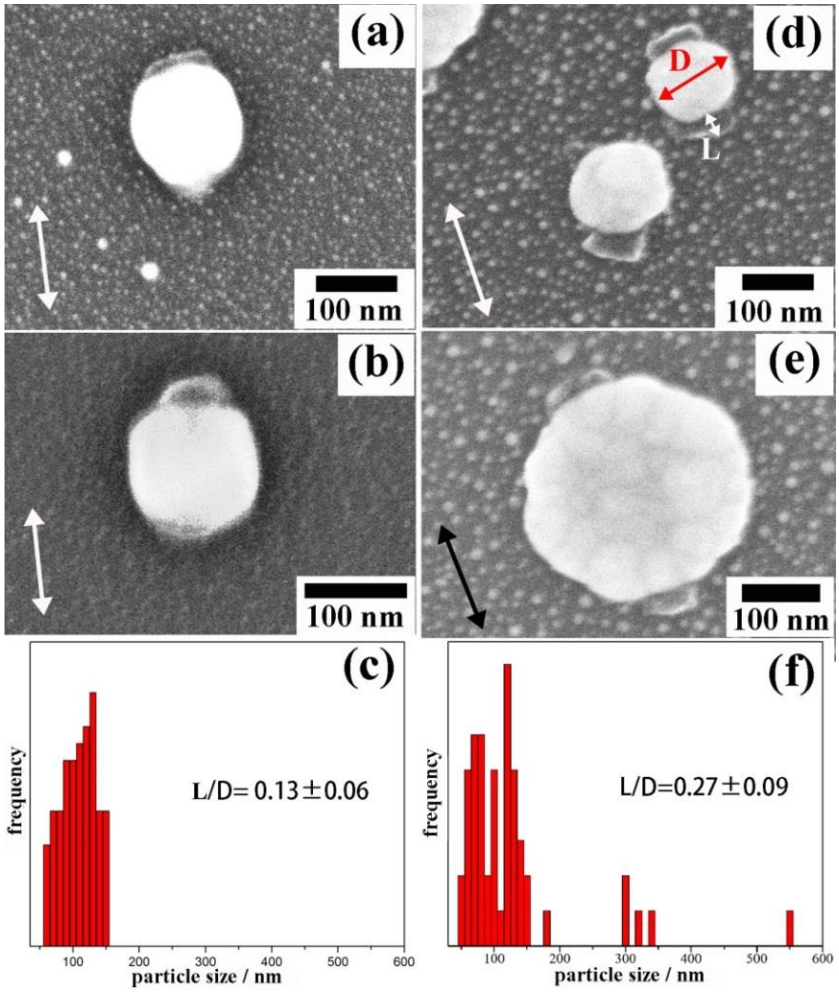

Fig.6-1, SEM morphology and size distribution of Ag particles which were ablated by fs laser irradiation at fluence 7.2 mJ/cm^2 for 10 sec in different pressures. (a) 1.3x10^{-4} Torr, (b) 1.7x10^{-2} Torr, (c) size distribution of the particles irradiated at pressure of 1.7x10^{-2} Torr, (d-e) SEM morphology at pressure of 760 Torr, (f) size distribution of the particles irradiated at pressure of 760 Torr. The double ends arrows show the direction of laser polarization.

When the particles were irradiated in air at pressure of 760 Torr, similar "tab" structures were obtained (Figs.6-1d and 1e), and the *L/D* ratio increased to 0.27 ± 0.09 (based on 50 counts). This suggests that the increase of air pressure enhanced the ablation of the particles in laser polarization direction. Meanwhile, aside from the ablation of the particles in size range of 50-150 nm, ablation was also observed in the particles with sizes larger than 300 nm (Figs.6-1e and 1f). As the enhancement factor in LSP-induced hotspots which contribute to the ablation of irradiated particles is much lower in the large sizes particles (> 300 nm) than that in the particles ranging from 50-150 nm (data is not shown here), the ablation in larger size particles is probably due to LSP-triggered reaction between the particles and air. As the air is consisted of 21 vol% oxygen (O_2) and 78 vol% nitrogen (N_2), their contributions were investigated by irradiating Ag particles in pure N_2 and O_2 at atmosphere pressure, respectively. The SEM images of the morphology for Ag particles irradiated in N_2 (Fig.6-2a) and O_2 (Fig.6-2b) indicate that more serious ablation of the particles happened in O_2 than in N_2. The *L/D* ratio in N_2, 0.12 ± 0.03, was close to that in vacuum, while the ratio in O_2 (0.21 ± 0.04) was much larger than that in N_2 and close to that in the air. It implies that the O_2 played a dominant role in enhancing the ablation of Ag submicron/nanoparticles under fs laser irradiation.

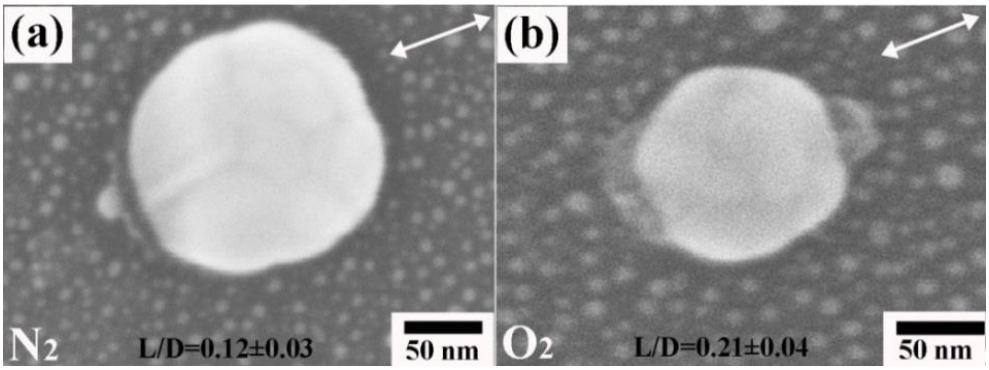

Fig.6-2, SEM images of the morphology for Ag NPs which were irradiated by fs laser pulses at fluence 7.2 mJ/cm^2 for 10s in N_2 (a) and O_2 (b). The double ends arrows show the laser polarization.

6.4 Investigation of mechanism

The reaction between O_2 and Ag is negligible at room temperature [131], this implies that the laser radiation is vital for the reaction of O_2 with Ag. Three different interactions between laser radiation and O_2, corresponding to multi-photon dissociation (photon energy < 5.2 *eV*) or ionization (photon energy < 12.1 *eV*) of O_2, have been reported [132, 133]. They can be written as:

$$O_2 + n_1\, h\nu = O + O \quad (6\text{-}1)$$

$$O_2 + n_2\, h\nu = O_2^+ + e^- \quad (6\text{-}2)$$

$$O + n_3\, \mathrm{hv} = O^+ + e^- , \quad (6\text{-}3)$$

where n_1, n_2, and n_3 are the numbers of the laser photons absorbed by O_2 molecules in the dissociation (eqn.6-1) and ionization (eqns. 6-2 and 6-3) processes. The threshold energy for the dissociation of O_2 (eqn.1) is 5.2 *eV* [134], while those for ionization of O_2 (eqn.6-2) and O (eqn.6-3) are 12.1 *eV* [135] and 13.6 *eV* [136], respectively. It indicates that the dissociation of O_2 is much easier than the ionization of O_2 and O, implying that the dissociation of O_2 will be the primary laser-O_2 interaction. In this work, the photon energy is 1.55 *eV*, and absorption of five photons is needed to dissociate O_2 [132]. After the dissociation of O_2, the generated O with 1.28 *eV* kinetic energy (half of the exceeded energy which is calculated by minus the dissociation energy 5.2 *eV* of O_2 with the total absorbed photon energy 7.75 *eV*) would impact and react with the surface of the particle to become stabilized. Assuming all the kinetic energy of O is released in its reaction with the surface of Ag particle, then the possible reactions of O with Ag can be written as follows [137, 138]:

$$0 + 2Ag = Ag_2O + 154.6 kJ/mol \quad (6\text{-}4)$$

$$O + Ag_2O = (AgO)_2 + 116.7\ kJ/mol \quad (6\text{-}5)$$

$$O + (AgO)_2 = Ag_2O + O_2 + 130.3\ kJ/mol. \quad (6\text{-}6)$$

Eqns.6-4, 6-5, and 6-6 clearly show that a huge amount of energy is released after the reaction of O with Ag; this released energy will cause the localized heating in the particle. Due to its low decomposition temperature (190 ℃), Ag_2O will probably decompose if reaction of eqn.6-4 induced temperature rise in the Ag_2O is higher than 190 ℃. It is noted that the reactions of eqns.6-5 and 6-6 are dependent on the generation of Ag_2O, or in other words the reaction of eqn.6-4, implying that the reactions of eqns.6-5 and 6-6 may not take place in fs laser radiation process. The decomposition of Ag_2O can be written as:

$$Ag_2O = 2Ag + \frac{1}{2}O_2 - 31.1\ kJ/mol, \quad (6\text{-}7)$$

and its activation energy is ~ 124 kJ/mol [139]. The released energy in eqn.6-4 is 154.6 kJ/mol; this value is much larger than the activation energy for the decomposition of Ag_2O, and the enthalpy of formation 31.1 kJ/mol in eqn.6-7, suggesting that Ag_2O will decompose after its initial generation through reaction of eqn.6-4. In other words, Ag_2O is the intermediate product which transfers the kinetic energy of O into the irradiated Ag particles and produce enhanced localized heating; few or even no Ag_2O will be present in the re-deposited material. Then, eqns.6-4 and 6-7 can be simplified as eqn.6-8, supposing that Ag particles only provide the surface for the recombination of O and the energy transfer from O to the particles.

$$2O \xrightarrow{Ag} O_2 + 247\ kJ/mol \quad (6\text{-}8)$$

Eqn.6-8 suggests that the enhanced local heating in fs laser irradiated Ag particles depends on the amount of O which recombines on the surface of the particles. The more recombined O, the more significant localized heating. This is reflected in the increase of the *L/D* ratio as indicated in Fig.6-2.

As shown in Fig.6-3, with the increase of N_2 pressure from 10^{-2} Torr to 760 Torr, the *L/D* ratio of Ag particles which were irradiated by fs laser at a fluence ~10 mJ/cm^2 for 10 sec were ~ 0.16-0.2. The absence of a strong effect of N_2 pressure on the *L/D* ratio arises because N_2 does not react with Ag particles, and the pressure does not significantly influence the deposition of ablated material.

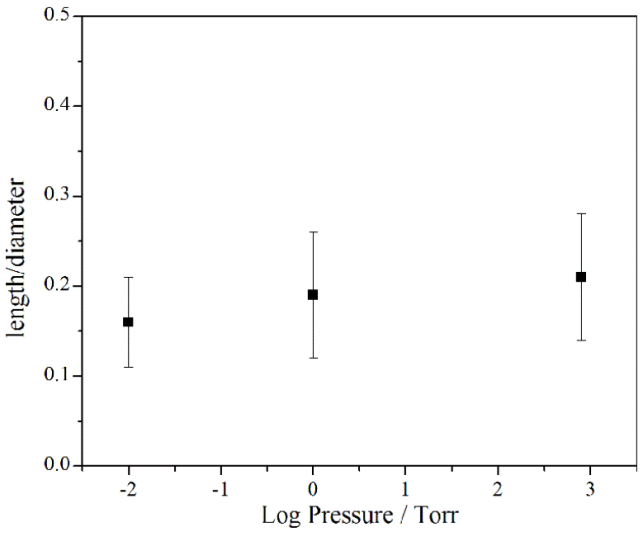

Fig.6-3, Correlation between *L/D* ratio and pressure in fs laser irradiated Ag particles at different N_2 pressures. The laser fluence is ~ 10 mJ/cm^2, and irradiation time is 10 sec.

A significant variation of the *L/D* ratio was observed when the Ag particles were irradiated by fs laser at different air pressures (corresponding to different O_2 concentration). Fig.6-4a shows the change in the *L/D* ratio with O_2 concentration. It is evident that at a laser fluence 7.2 mJ/cm^2, increasing the concentration of O_2 from $6x10^{11}$/cm^3 (corresponding to $1x10^{-4}$ Torr as indicated in Fig.6-4a) to $6x10^{15}$/cm^3 (corresponding to 1 Torr as indicated in

Fig.6-4a), results in an increase in the average *L/D* ratio from 0.1 to 0.25. Further increasing the concentration to $5x10^{17}/cm^3$ (corresponding to 760 Torr as indicated in Fig.6-4a), the average *L/D* ratio remained almost unchanged, only slightly increasing to 0.27. This implies that at certain fs laser fluence the amount of O which is generated from the dissociation of O_2 will be saturated when the O_2 concentration increases up to a critical value. Above the critical O_2 concentration, the amount of generated O can be further increased by increasing laser fluence [133]. Fig.6-4b shows the correlation of *L/D* ratio with laser fluence at O_2 concentrations of $5x10^{17}/cm^3$ (corresponding to 760 Torr) and $6x10^{11}$ $/cm^3$ (corresponding to $1x10^{-4}$ Torr). It indicates that at both concentrations the *L/D* ratio increases with the increase of laser fluence; while it increases much faster at the concentration of $5x10^{17}/cm^3$ than at $6x10^{11}$ $/cm^3$, especially when the fluence is larger than ~7.2 mJ/cm^2. At a concentration of $6x10^{11}$ $/cm^3$, the *L/D* ratio tends to reach constant ~ 0.2 with the increase of laser fluence from ~ 4 mJ/cm^2 to ~ 14 mJ/cm^2. That is because this O_2 concentration is much lower than the critical concentration, and the *L/D* ratio is therefore limited by the concentration of O_2.

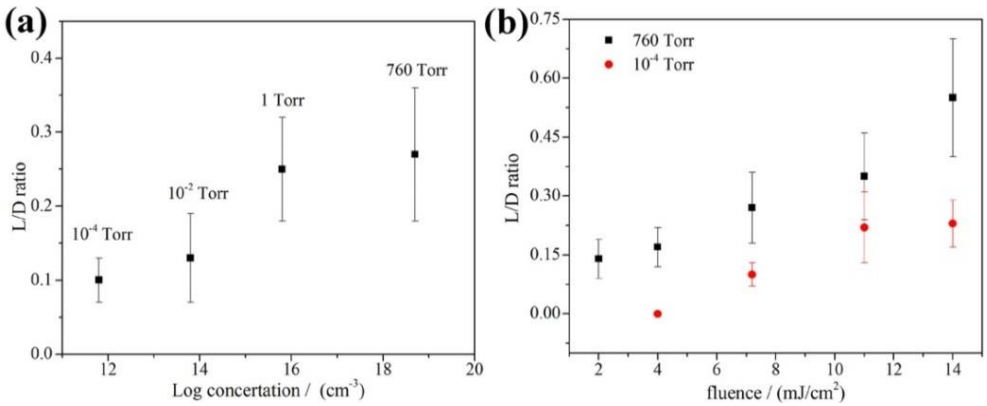

Fig.6-4, Correlation between L/D ratio and the O_2 concentration (a) and the laser fluence (b). The laser fluence in (a) is 7.2 mJ/cm^2.

To better understand the development squence of Ag submicron/nanoparticles under fs laser radiation in air, the morphology change of the irradiated particles with irradiation time

were recorded. Fig.6-5 shows the SEM images of the morphology for Ag submicron/nanoparticles irradiated by fs laser pulses for 1, 4, 7, and 10 sec at a fluence 14 mJ/cm^2. Here, high fluence (~ 14 mJ/cm^2) was used in order to obtain visible morphology change of the irradiated paticles in small irradiation time.

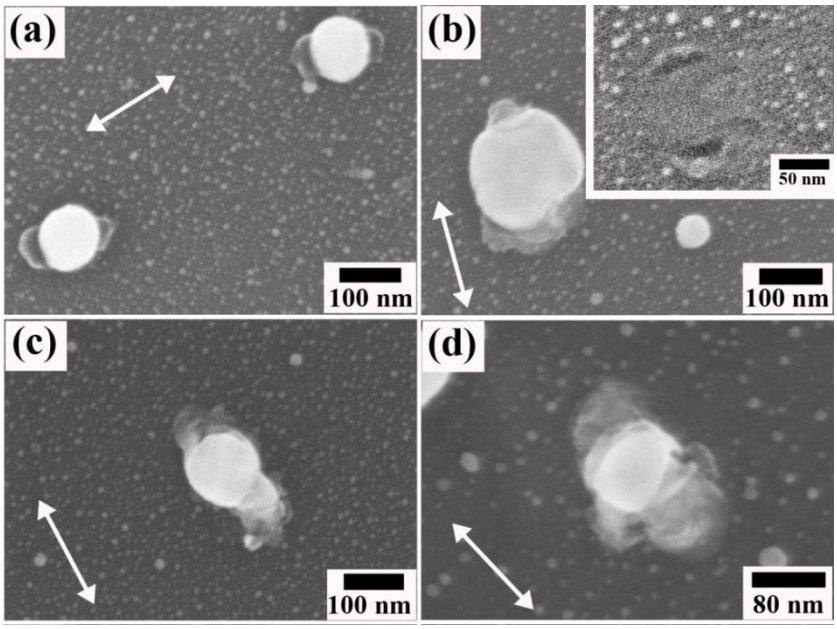

Fig.6-5, SEM images of the morphology for the Ag NPs where were irradiated by fs laser at fluence 14 mJ/cm^2 for different time. (a) 1 sec; (b) 4 sec, the inset image shows the holes in the Si wafer; (c) 7 sec; (d) 10 sec. The double ends arrows show the laser polarization.

Fig.6-5a shows that after 1 sec laser radiation, "tab-like" structure formed on the irradiated particles, but no evident damage to the particles was observed. This is similar with the observations in Figs.6-1 and 6-2. With an increase of irradaition time to 4 sec (Fig.6-5b), the particles start to be ablated. Some particles were blown away after laser irradiation leaving two holes in the Si wafer, as shown in the inset of Fig.6-5b. Since the laser fluence was much lower than the damage threshold fluence of Si wafer [115], the holes in the Si wafer were caused by the enhanced ablation in LSP-induced hotspots as reported previously [73]. This implies that the ablation of the particles started from the edge of its bottom surface where electric field enhancement in the hotspots is much higher that in

other locations (this is supported by the simulated electric field distribution in the NPs, data as shown later in Fig.6-6). Further increases in the irradiation time to 7 sec (Fig.6-5c) and 10 sec (Fig.6-5d), results in more serious ablation of the particles, and the particles were extend in the laser polarization direction due to the re-deposition of ablated materials, facilating the joining of separated Ag submicron/nanoparticles.

As discussed in Fig.6-5, the ablation of a Ag particle starts from the edge of its bottom surface where the hotspots are located due to the excitation of LSP. To demonstrate this, FDTD simulations were carried out to identify the hotspots distribution in the irradiated Ag particles on the Si wafer. The schematic of the simulation setup is shown in Fig.6-6a, where an Ag cylinder with a diameter/height (Y/Z) ratio of 2.8 is placed on the 30 nm thick Si wafer with a 2 nm SiO_2 surface layer. Laser radiation with wavelength 800 nm is incident in the Z direction and the laser polarization direction is parallel to the Y axis. The hotspot distribution in the YZ (Fig.6-6b) and XZ planes at different heights (Figs.6-6c, 6d and 6e) are recorded. Fig.6-6b clearly shows that the hotspots with the highest electric field enhancement factor are located at the bottom edge of the particle. This is consistent with the SEM observation in Fig.6-5b. The hotspot distribution in the XY planes at different heights of the particle, as shown in Figs.6-6c, 6d and 6e, indicates that the electric field enhancement factor at the bottom edges of the Ag particles is several tens times higher than at other locations. It also shows that the distribution of the hotspots is parallel to laser polarization. This is consistent with the SEM observation of directional ablation of the Ag particle in the laser polarization direction, suggesting that LSP-induced electric field enhancement (or hotspots) is the trigger for the enhanced ablation in air.

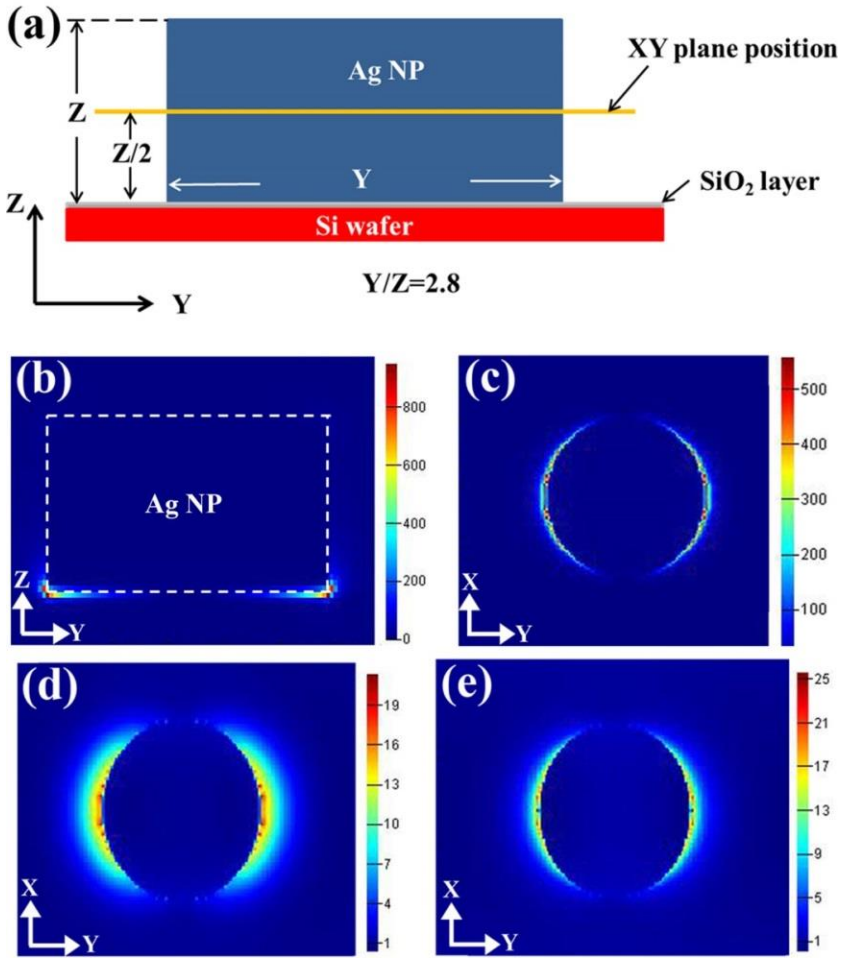

Fig.6-6, Schematic for FDTD simulation of the electric field enhancement in Ag NP (Y=150 nm) which is placed on a 30 nm Si wafer with a 2 nm SiO_2 surface layer (a), electric field enhancement (bright area, the same in the following figures) in XZ plane (b), electric field enhancement in the XZ plane which is 1 nm above the bottom surface of the particle (c), electric field enhancement in the XZ plane which at the half height of the particle (d), electric field enhancement in the XZ plane which is 1 nm below the top surface of the particle (e). The laser with wavelength 800 nm is incident in Z direction, and laser polarization is in Y direction. The enhancement factor in the scale bar is defined as E_1^2/E_0^2.

6.5 Joint analysis of interconnected Ag submicron/nanoparticles

As discussed above, under fs laser radiation, the irradiated submicron/nanoparticles extended in the direction of laser polarization due to the accumulation of ablated material, possessing the potential of interconnecting separated particles for application in the assembly of nanodevices. Fig.6-7a shows that the separation distance between two Ag particles was reduced due to the accumulation of re-deposited material in laser polarization direction after fs laser radiation at fluence ~ 7.2 mJ/cm^2 for 10 sec. Some of the Ag

particles were even interconnected when the separation distance between them was ill-defined, as shown in Fig.6-7b. Ag particles with very large separation distances (~180 nm) could also be interconnected when the irradiation time was increased to 30 sec and 50 sec, as shown in Figs.6-7c and 7d. A bridge is obtained via the accumulation and sintering of ablated material between the separated particles. Prolonging the irradiation time results in the further accumulation of re-deposited material between the separated particles, facilitating the interconnection of particles with large separation distance.

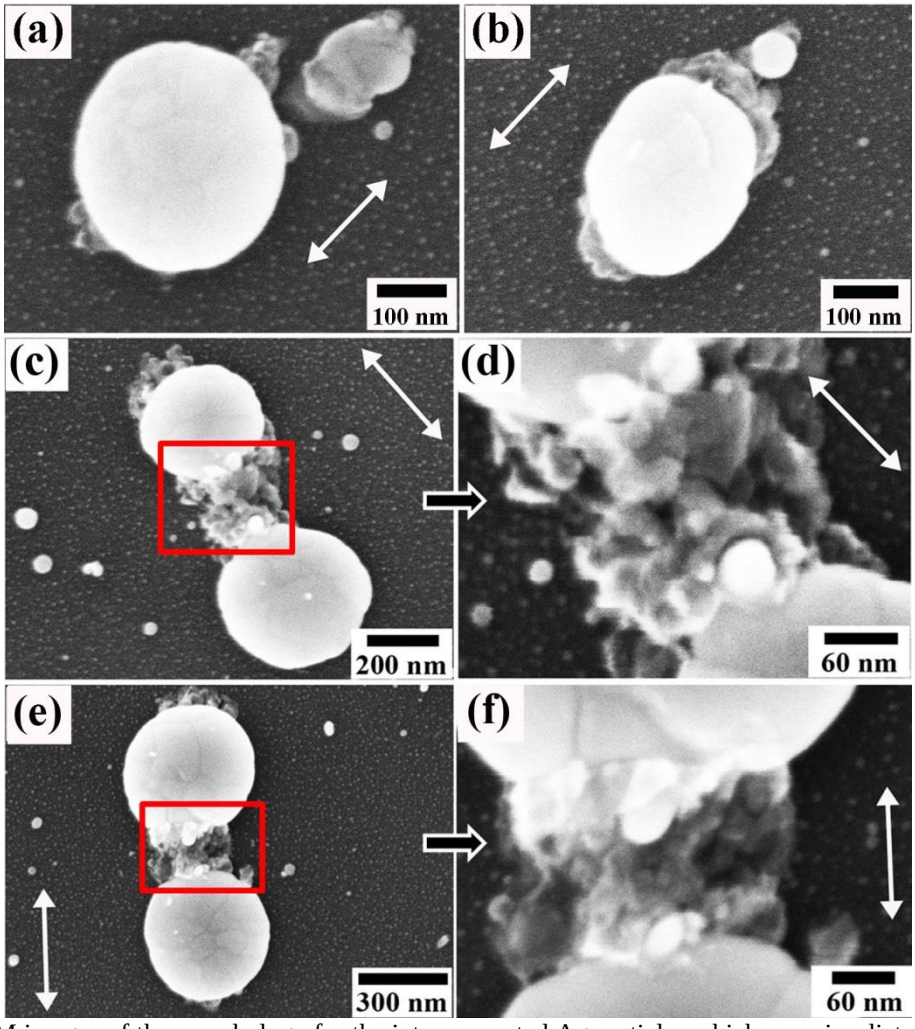

Fig.6-7, SEM images of the morphology for the interconnected Ag particles which were irradiated by fs laser at fluence ~ 7.2 mJ/cm^2 for different time. (a-b) 10 sec, (c) 30 sec, (d) magnified view of the square area in (c), (e) 50 sec, (f) magnified view of the square area in (f). The double ends arrows show the laser polarization direction.

This is supported by the increase of the ratio between the total length L_1 of the irradiated particle and its diameter D with the increase of irradiation time. The schematic for the measurement of L_1 and D is shown in Fig.6-8a. Fig.6-8b shows that, at a fs laser fluence of approximately 7.2 mJ/cm^2, the L_1/D increased from 1.1 to 1.54 and tended to reach a constant when the irradiation time increased from 0 sec to 70 sec. After 70 sec laser pulses irradiation, Ag particles were seriously damaged (Fig.6-8c), and in some cases the remaining part of the irradiated particle would be popped out from the deposited materials as shown in the inset image of Fig.6-8c. This can be contributed to the impact of the ablated material from the bottom edge of the irradiated particles, which is consistent with the SEM observation in Fig.6-5.

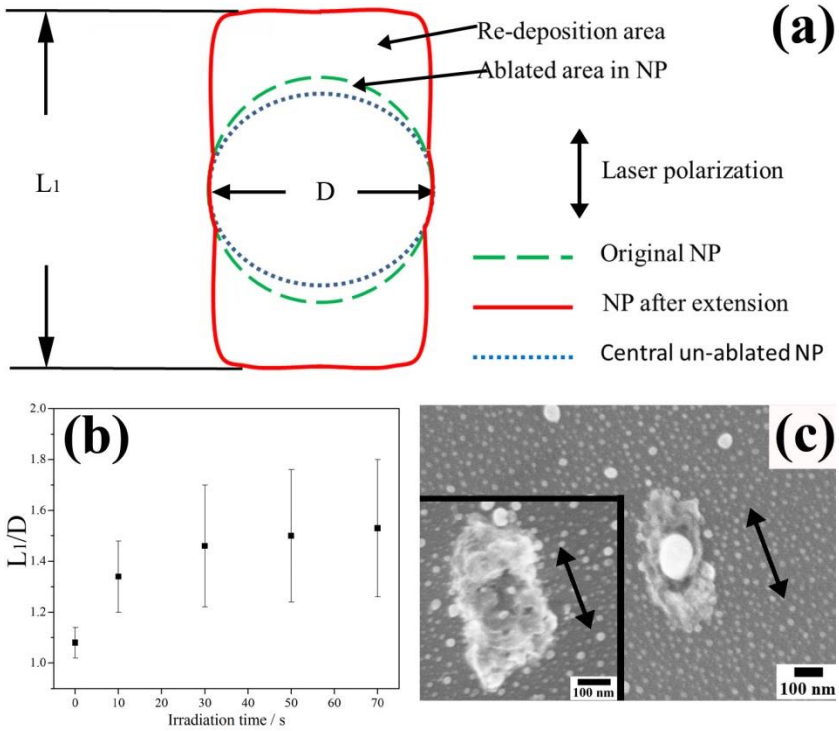

Fig.6-8, Schematic for the measurement of the total length $L_1$and diameter D of the extended NP (a), (b) correlation between L_1/D ratio with irradiation time at fs laser fluence ~7.2 mJ/cm^2, (c) SEM images of the morphology for the Ag NP which was irradiated by fs laser at fluence ~7.2 mJ/cm^2 for 70 sec. The double ends arrows in (c) show the direction of laser polarization.

For fs laser irradiation at higher fluence, the sintering of the re-deposited material in the interconnected area can be more extensive due to higher energy input, and a relatively denser joint structure can be obtained. As shown in Fig.6-9a, dense interconnection between two Ag submicron-sized particles with diameters 430 nm and 500 nm and separation distance 110 nm were obtained by fs laser irradiation at a fluence of approximately 11 mJ/cm^2 for 10 sec. This did not cause serious destruction of the particles except in the pole areas which were parallel to the laser polarization direction. Figs.6-9b and 9c show TEM images of the cross-section morphology in the interconnected area. It can be seen that two Ag submicron particles were interconnected via the accumulation of re-deposited material. This is reflected in the clear bonding interface between the Ag submicron particle and the re-deposited material (Fig.6-9d). The presence of re-deposited material in the Si wafer suggests that the ablated material came from both the Ag sub-micron particles and the wafer due to localized heating. EDS analyses in the interconnected area show that Si and O are present in the area close to the Ag particle. The ratio between Si and O atoms was approximately 1 (EDS spots A, B, C in Fig.6-9c). This ratio is close to that in the SiO_x ($x<2$) layer on the surface of Si wafer [127], suggesting that this material came from the ablation of the Si wafer. In the center of the interconnected area, the material consisted mainly of Ag with a small amount of Si but with some O (EDS spots D in Fig.6-9c), indicating there was no oxidation of Ag during its reaction with the atomic O from the dissociation of O_2. This is consistent with the above analysis and reveals that no Ag_2O is present in the ablated material. This implies that O_2 assisted fs laser processing technique can be used to join well-separated Ag particles without causing oxidation and possesses the potential for application in fabrication of nanoscale electronic

devices. Here, the Si in the re-deposited material came from the ablation of the wafer. The presence of Si in the interconnected area will influence the strength and electric conductivity of the joint. Figs.6-9d and 9e show the HRTEM images of the morphology for the interconnection of spots A and D, respectively. A clear bonding interface between the particle and the re-deposited material was observed in the area close to the particle (Fig.6-9d), while pure Ag-Ag metallic bonding could also be obtained in the center of the interconnected area, suggesting that complete metallic bonding between the irradiated Ag submicron particles could be obtained if the Si can be eliminated by reducing the ablation of the Si wafer.

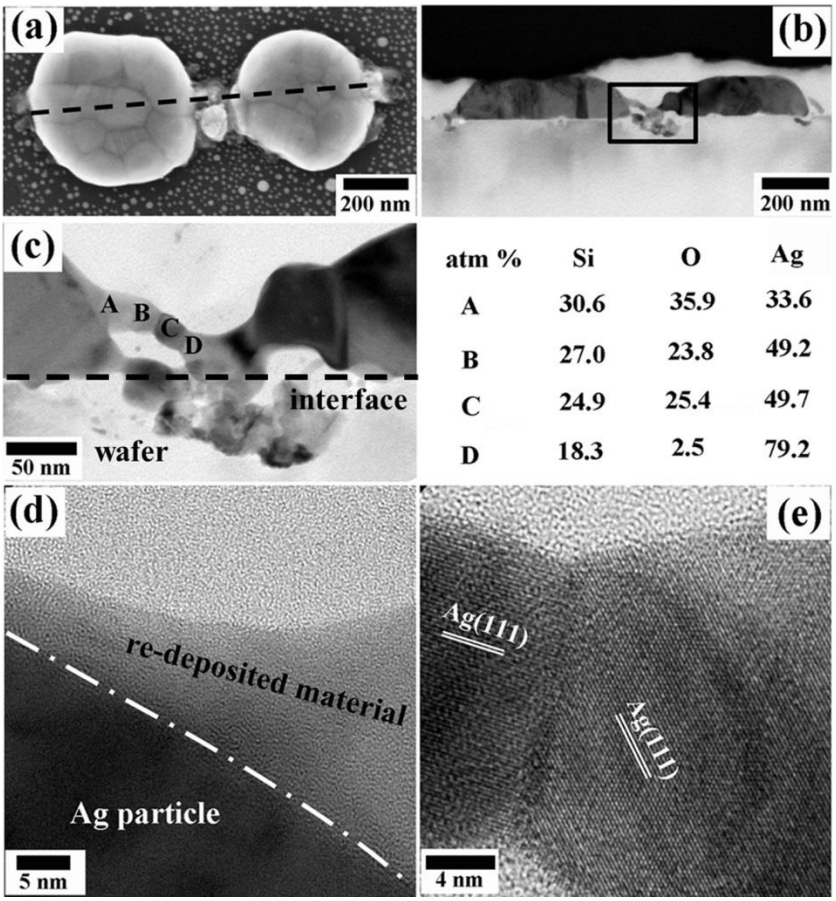

Fig.6-9, SEM and TEM analyses of Ag submicron particles which were irradiated by fs laser at fluence 11 mJ/cm^2 for 10 sec. (a) SEM image of the morphology for Ag submicron particles, the double-ends arrow shows the direction of laser polarization; (b) TEM image of the cross-section view of the submicron particles as the dash line indicates; (c) magified viiew of the square area 1 in (b) and corresponding EDS analyses of spots A, B, C, D; (d) HRTEM image of spot A in (c); (e) HRTEM image of spot D in (c).

Ablation of the Si wafer is due to the generation of hotspots close to the surface of the wafer. This is apparent in a FDTD simulation of the distribution of hotspots in the dimer particles present in Fig.6-9a. Fig.6-10a shows that hotspots are produced at the top and bottom tips of the particles in the region of the gap. The presence of hotspots at the bottom edge of the particles near the surface of Si wafer will be more commonly observed, because the particles usually had curved top surfaces due to the nature of the sputtering deposition process. The effect of curvature on the top of the particles on the location of hotspots can be seen in Fig.6-10b.

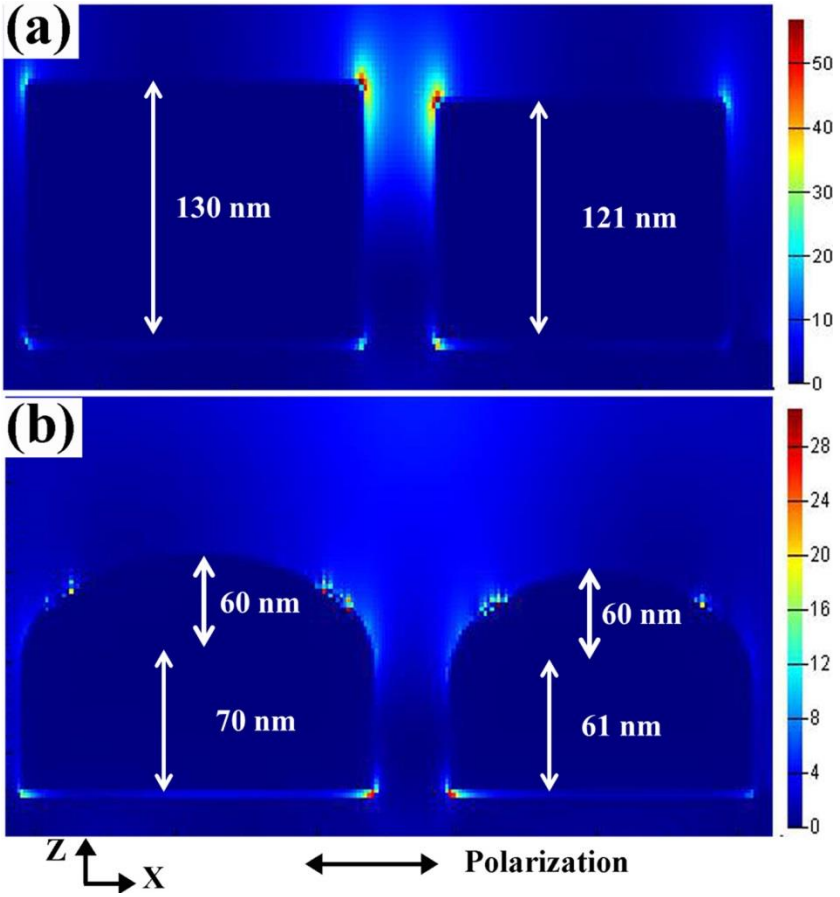

Fig.6-10, LSP-induced hotspots distribution (bright area) in different structures. (a) simulation of the dimer particle in Fig.6-9a, the Ag particles on the left has D_1=500 nm, D_2=470 nm and H=130 nm, the one on the right has D=430 nm and h=121 nm. (b) the effect of introducing curvature as shown. The curvature height is 60 nm. 800 nm wavelength laser radiation is incident in the Z direction, and the black double ends arrow shows the direction of optical electric field.

6.6 Selective tuning of hotspots

Elimination of ablation of the Si wafer can be accomplished by tuning the location of LSP-induced hotspots in the irradiated Ag particles. The influence of particle geometry, the ordering of particles including the distance by which they are separated, and laser wavelength has been studied in this context. Ag cylinders which can be easily fabricated by using electron beam lithography are chosen as representative structures.

Fig.6-11 shows the variation of the distribution of hotspots with the height of pairs of submicron Ag cylinders under irradiation with the 800 nm wavelength laser. The cylinder diameter is 200 nm, and the separation distance between cylinders is kept constant at 40 nm when varying the cylinder height. The simulations show that the hotspots are located at the bottom edges of the cylinders when the height of the cylinders is 80 nm (Fig.6-11a), but that they move to the upper edges of the cylinders when the height increased to 100, 120 and 140 nm (Figs.6-11b, 11c and 11d, respectively). Fig.6-11e records the minimum height/diameter (*H/D*) ratio as a function of diameter consistent with the appearance of hotspots at the upper edges of the cylinders. This indicates that the ratio decreases with an increase in cylinder diameter and that the minimum height should be > 100 nm. It also shows that it is impossible to generate hotspots in the upper edges of pairs of cylinders having diameters of 100 nm. This provides an important guide for the selection of particle sizes.

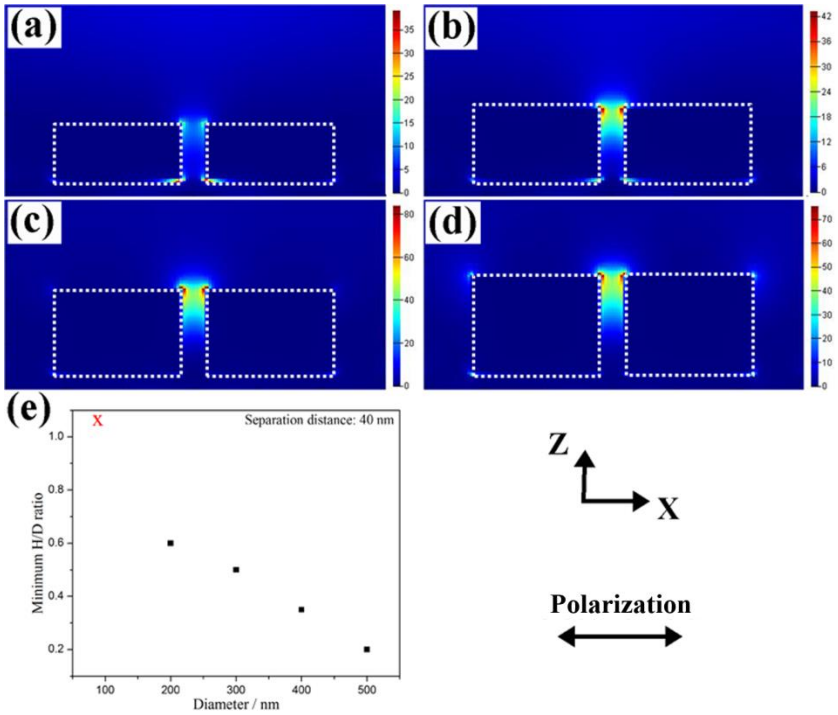

Fig.6-11, Changes in the distribution of hotspots between pairs of identical Ag cylinders having a diameter of 200 nm and different height. (a) Height is 80 nm; (b) Height is 100 nm; (c) Height is 120 nm: (d) Height is 140 nm; (e) Required minimum height/diameter (*H/D*) ratio in cylinders pairs with different diameters for the appearance of hotspots at upper edges; the cross indicates that there are no hotspots at the upper edges. The separation distance between the cylinders is constant at 40 nm, and the cylinders are irradiated by 800 nm wavelength laser in the Z direction.

The effect of separation distance between pairs of cylinders on the spatial distribution of hotspots is shown in Fig.6-12. The simulations show that the hotspots are located at the upper edges of the cylinders when the separation distance is < 100 nm (Figs.6-12a, 12b and 12c). In general, the enhancement factor in the hotspots also decreased with an increase of separation distance (Fig.6-12f). With a further increase in the separation distance to 120 and 160 nm, hotspots appear at the bottom edges of the particles (Fig.6-12d and 12e). Simulations are then useful in determining the irradiation conditions that minimize the damage to the underlying Si wafer.

The effect of laser wavelength on the distribution of hotspots is given in Fig.6-13a. This shows that in pairs of Ag cylinders having 400 nm diameter and 60 nm height, hotspots are

located at the upper edges between the cylinders when irradiated by a 500 nm wavelength laser. This type of distribution minimizes damage to the Si wafer. With laser wavelength is increased to 600, 700, and 800 nm, the hotspots move toward the surface of the Si wafer. This suggests that for pair of cylinders of a given diameter, the required minimum *H/D* ratio can be further decreased by decreasing the wavelength of the laser pulses.

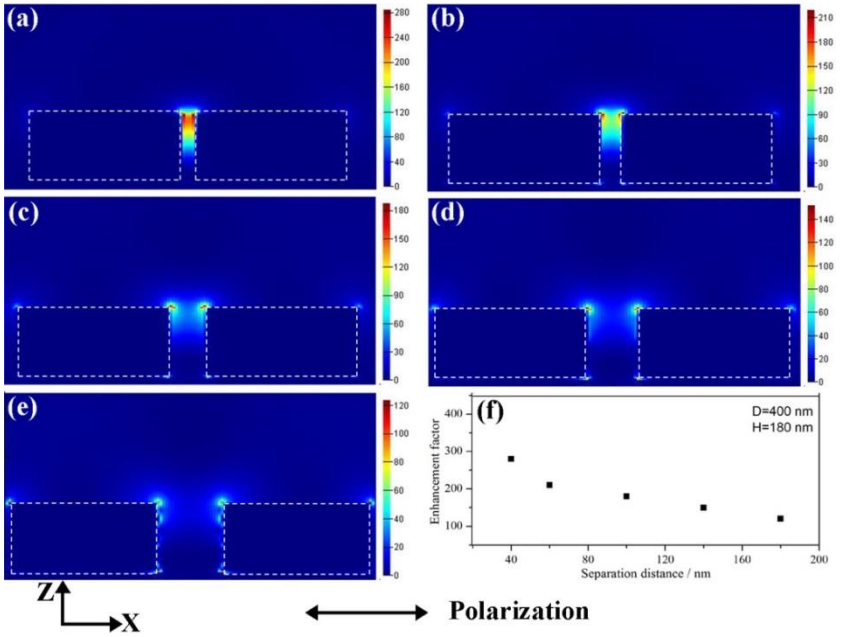

Fig.6-12, Hotspots distribution between pairs of 400 nm diameter Ag cylinders with different separation distances.(a) 40 nm; (b) 60 nm; (c) 100 nm; (d) 120 nm; (e) 160 nm; (f) correlation between separation distance and enhancement factor in the hotspots. The pairs of cylinders are irradiated by 800 nm wavelength laser in the Z direction.

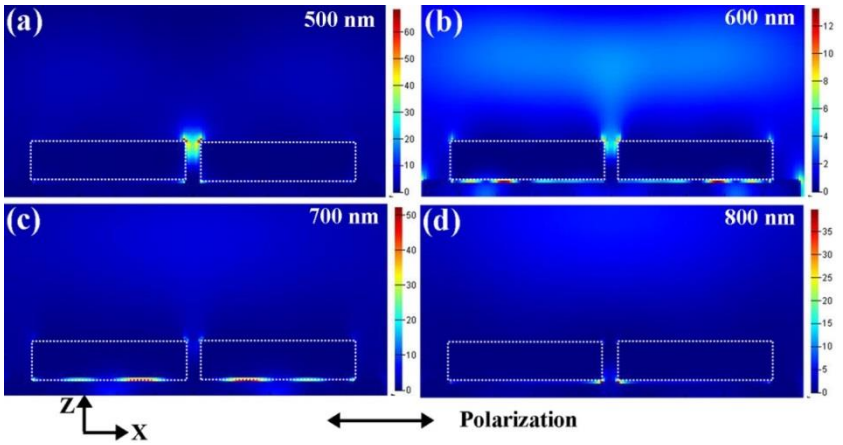

Fig.6-13, Hotspots distribution in pairs of Ag cylinders which are irradiated by different laser wavelengths. (a) 500 nm; (b) 600 nm; (c) 700 nm; (d) 800 nm. The diameter of the cylinders is 400 nm, and the height is 60 nm. The laser is incident in the Z direction, and gap distance is constant at 40 nm.

In summary, varying the particle geometry, the structure of pairs of particles, and the laser wavelength allow for tuning the distribution of hotspots to facilitate the interconnection of adjacent Ag cylinders for specific practical application.

6.7 Summary and concluding remarks

In this work, it is demonstrated that Ag submicron/nanoparticles can be directionally ablated by fs laser irradiation in air via LSP-induced hotspots in fluence range of 2~14 mJ/cm^2. The hotspots also facilitate the dissociation of O_2 which further accelerates the ablation process as O atoms react with the Ag surface and produce additional localized heating. The ablated material re-deposits near the irradiated particles and results in their directional extension in the direction of the laser polarization, facilitating the interconnection of Ag submicron/nanoparticles. TEM analyses of the cross-section morphology for interconnected Ag particles indicate that no Ag_2O is present in the interconnected area but that some SiO_x and Si is present. This material originates from the ablation of the Si wafer. FDTD simulations show that changing particle geometry, structure arrangement and laser wavelength can tune the distribution of hotspots to minimize this effect and damage to the Si wafer. This should result in improved joint strength and electric conductivity in the junction.

Chapter 7 Conclusions and Suggestions for Future Work

7.1 Conclusions

The work described in this thesis has focussed on a study of the interaction of fs laser radiation with Ag submicron/nanoparticles under a variety of conditions. These conditions include, particles with or without a PVP coating, particles in random motion in solution, and particles deposited on a Si wafer in air or high vacuum. The mechanisms responsible for the interconnection of Ag particles under these conditions have been investigated and the role of the excitation and propagation of LSPs in the fs laser irradiation process has been identified. The conclusions drawn from these studies can be summarized as follows:

1. The fs laser radiation causes the dissociation of PVP which is coated on the surface of Ag NPs and its transformation into amorphous carbon. The formation of hydrophobic amorphous carbon on the surface of Ag NPs promotes the adhesive bonding of NPs in the aqueous solution. Hotspots, where electric field is enhanced, are then generated between the adhesively bonded Ag NPs due to the excitation of LSP. This enhances the removal of the amorphous carbon in the junction between NPs, leading to the formation of metallic bonds. In addition, the gradient of the electric field in the hotspots in the joined structure can lead to the appearance of an optical force on nearby NPs. This facilitates the attraction and bonding of the nearby NPs to the original structure, resulting in the formation of larger NPs assemblies consisting of joined component when the NPs solutions are irradiated at fluence > 1.8 J/cm^2.

2. In plasmonic Ag NPs structures deposited on the surface of a Si wafer, NPs are melted and may be joined when irradiated with fs laser pulses at fluence > 7.2 mJ/cm^2, forming

larger spherical particles. This process is attributed to the enhanced absorption of laser radiation which associated with the generation of LSP-induced hotspots in the plasmonic structures. LSP-induced hotspots promote the decomposition of PVP coatings, which further increase the absorption of laser radiation. As a result, an absorption efficiency > 0.7 can be obtained in the plasmonic structures.

3. Ag sub-micron/nanoparticles (50-600 nm) were deposited on the surface of a Si wafer by laser ablation of an Ag target. It was found that at fs laser ablation of these particles in high vacuum (10^{-6} Torr) occurs in the areas near the hotspots. In the case of sub-micron Ag particles pair with a small distance (~ 30 nm), ablation is located between the particles when the laser polarization direction is parallel to the long axis of the particles pair. Ablated material is redeposited between the particles, resulting in their interconnection. The ablation is significantly enhanced when the Ag particles are irradiated in air at a pressure > 1 Torr; and the interconnection of particles with larger separation distance (> 100 nm gap) can be achieved at an air pressure of 760 Torr. This is attributed to the enhanced local heating arising from the reaction of atomic oxygen with the surface of Ag particles. The atomic oxygen is believed to be produced from the multi-photon dissociation of oxygen molecules, and this process is enhanced in the vicinity of laser-induced hotspots.

7.2 Suggestions for future work

Based on the above research results, some future work about fs laser fabrication is suggested as:

1. In-situ fabrication of nanodevices based on pre-fabricated plasmonic structures by manipulating LSP-enhanced optical force, local heating or local ablation. Chemical

synthesis is a convenient method for the production of nanomaterials for nanodevice fabrication, but positioning these chemically synthesized nanomaterials and joining them to a substrate is difficult. Precise manipulation of precursor with AFM tip combined with near scanning optical microscopy (NSOM) without causing serious damage to the nanomaterials is a challenge. Pre-selection of specific plasmonic structures followed by the fabrication of tailored functional nanodevices via the manipulation the hotspots in the pre-fabricated structures as discussed above is an attractive alternative. Electron beam lithography is the technique of choice for pre-fabrication plasmonic structures due to its high resolution. This is enhanced by FDTD calculations which guide the design of pre-fabricated plasmonic structures. These studies will be helpful for obtaining better understanding LSP facilitated nanofabrication.

Fig.7-1 shows an example of a field effect transistor which can be produced based on pre-fabricated metallic plasmonic nanocylinders, electrodes (drain and source) and single crystalline Si nanocube on the insulate substrate, by utilizing electron beam lithography technique and fs laser radiation. Before fs laser irradiation, the pre-fabricated nanocylinders, electrodes, and nanocubes are isolated. After fs laser irradiation with a polarization direction parallel to nanostructures array, the metallic nanocylinders will be ablated and extended along both sides along the laser polarization direction due LSP-induced local ablation as reported in chapter 6. This will result in the interconnection of the electrodes and the Si nanocube and formation of a single particle field effect transistor. Fig.7-2 shows the proposed fabrication protocol for this field effect transistor. The procedure includes resist coating, electron beam etching, metallic film deposition, lift-off, positioning of the Si nanocube, and fs laser radiation. The first four operations in the fabrication procedure are

standard processes in electron beam lithography. After lift-off, the Si nanocube can be positioned into the pre-fabricated pattern by charge patterning as reported previously [140], and then be interconnected to the drain or source by fs laser radiation, forming a field effect transistor. This procedure can also be used to produce transistor arrays for applications as sensor arrays.

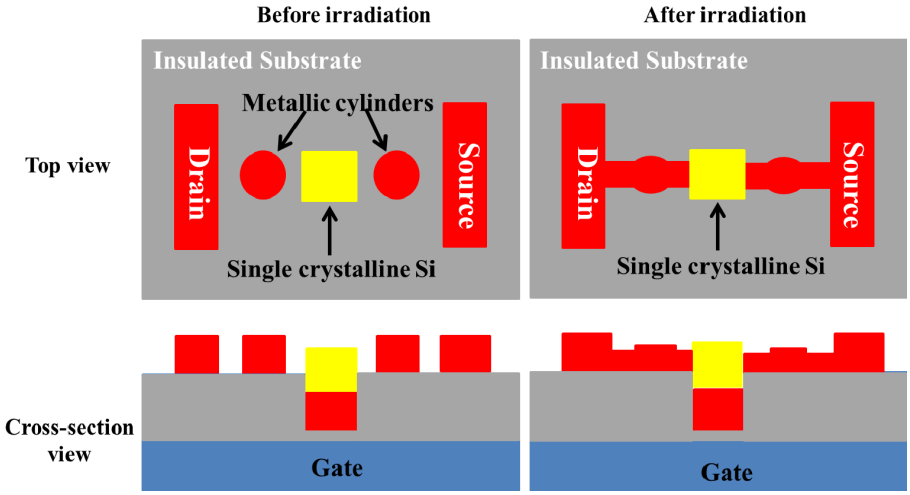

Fig.7-1, Schematic for the design of a single particle field effect transistor

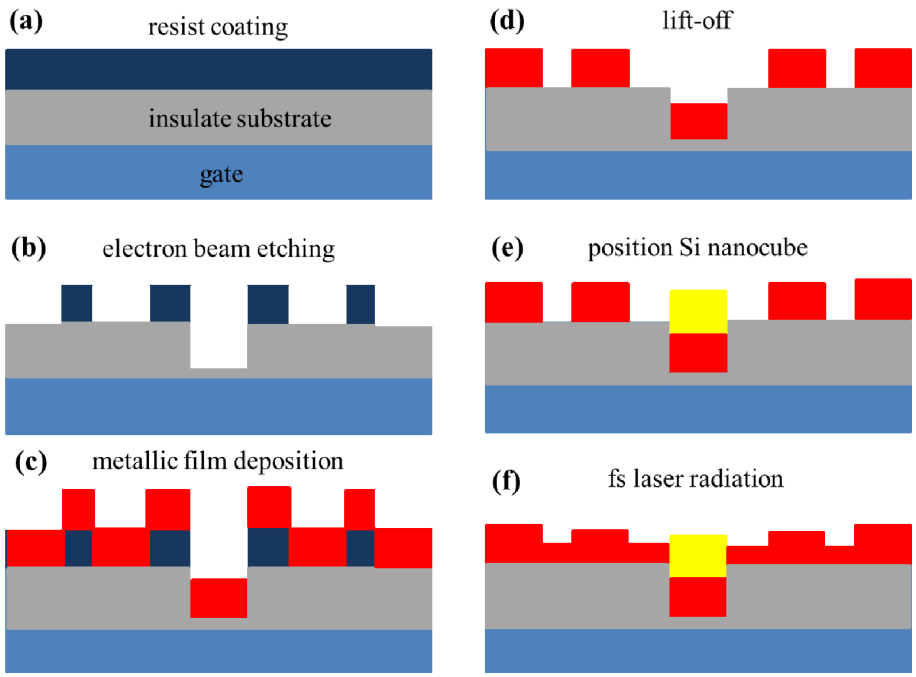

Fig.7-2, Procedure of producing a single crystalline Si field effect transistor by combining electron beam lithography and fs laser radiation.

2. Investigation and quantitative characterization of the stability of Ag and Cu nanomaterials after fs laser irradiation. Ag nanomaterials show promise applications in nano-electronics or optics because of their excellent electrical or optical properties. However, these nanomaterials, especially Ag nanowires which are usually produced by chemical synthesis method, are not stable when they are thermally heated or exposed to sulfur-containing air. The stability of Ag nanomaterials can be improved by modifying the crystal structure. As reported, Ag nanowires with <111> crystal facets are more stable than those with other types of facets [141]; while fs laser annealing at low fluence (less than several tens of millijoule per square centimeter) might be an effective way of obtaining thermally stable crystal structures. In addition, fs laser induced dissociation of the polymer on the surface of Ag nanomaterial into amorphous carbon can also be used to inhibit the reaction of Ag with sulfur-containing chemicals in air. A quantitative characterization the stability of Ag nanomaterials can provide a valuable guide for the use of these materials in industrial applications.

Identify the feasibility of improving the anti-oxidation ability of Cu nanomaterials by transforming their polymer coating on the surface into amorphous carbon with fs laser radiation, and then quantitatively characterize the anti-oxidation ability of carbon coated Cu nanomaterials will also be an interesting topic for nanoelectronics. The Cu nanomaterials have similar electric conductivity to Ag nanomaterials, it is less susceptible to electromigration and the cost is much lower.

3. Extend the research into gas assisted fs laser processing for high aspect hole drilling for applications in integrated optics. In integrated optics, holes with ~200-300 nm diameters have to be drilled to deeper than 2 μm in photonic crystals (InP or InGaAsP based), in

order to produce vertical step-index waveguides for compact optical solutions. Chemical assisted ion beam etching (CAIBE) or plasma etching are two widely used methods, where chlorine (Cl_2) is usually used as assistant chemical. In these methods, a mask is usually needed to protect the photonic crystals against the damage from the high energy ion beam or plasma. It is found that the ion beam or plasma tends to produce a rough sidewall which affects the waveguide performance.

By utilizing fs laser irradiation, self-focusing of laser beam can generate localized high intensities, trigger the ionization and dissociation of Cl_2. This could facilitate etching of these photonic crystals. In addition, the dissociation energy of Cl_2 is only 2.5 *eV*. This can reduce the requirement of the incident laser intensity, minimize laser induced damage to the photonic crystal and obtain higher quality holes. Mask material may be not necessary, which makes the procedure much simpler.

References

1. M. Takagi, *Electron-diffraction study of liquid-solid transition of thin metal films.* J. Phys. Soc. Jpn, 1954. **9**(3): p. 359-363.
2. C. Tang, Y. M. Sung, and J. Lee, *Nonlinear size-dependent melting of silica-encapsulated silver nanoparticles.* Appl. Phys. Lett., 2012. **100**: p. 201903.
3. A. Hu, et al., *Low temperature sintering of Ag nanoparticles for flexible electronics packaging.* Appl. Phys. Lett., 2010. **97**: p. 153117.
4. D. O. Lapotko, E. Lukianova, and A. A. Oraevsky, *Selective laser nano-thermolysis of human leukemia cells with microbubbles generated around clusters of gold nanoparticles.* Lasers Surg. Med., 2006. **38**(6): p. 631-642.
5. F. J. Beck, A. Polman, and K. R. Catchpole, *Tunable light trapping for solar cells using localized surface plasmons.* J. Appl. Phys., 2009. **105**: p. 114310.
6. N. Nuntawonga, et al., *Surface-enhanced Raman scattering substrate of silver nanoparticles depositing on AAO template fabricated by magnetron sputtering.* Vacuum, 2010. **84**(12): p. 1415-1418.
7. X. Zhou, et al., *Size-dependent catalytic activity and dynamics of gold nanoparticles at the single-molecule level.* J. Am. Chem. Soc., 2010. **132**(1): p. 138-146.
8. R. Jin, et al., *Size-dependent catalytic properties of Au nanoparticles supported on hierarchical nickel silicate nanostructures.* Dalton Trans., 2013. **42**(22): p. 7888-7893.
9. C. Liu, et al., *Room-temperature cold-welding of gold nanoparticles for enhancing the electrooxidation of carbon monoxide.* Chem Commun (Camb), 2011. **47**(15): p. 4481-4483.
10. S. J. Hardman, et al., *Electronic and surface properties of PbS nanoparticles exhibiting efficient multiple exciton generation.* Phys. Chem. Chem. Phys., 2011. **13**(45): p. 20275-20283.
11. G. Y. Yurkov, et al., *Electrical and magnetic properties of nanomaterials containing iron or cobalt nanoparticles.* Inorg. Mater., 2007. **43**(8): p. 834-844.
12. F. C. Chen, et al., *Plasmonic-enhanced polymer photovoltaic devices incorporating solutionprocessable metal nanoparticles.* Appl. Phys. Lett., 2009. **95**: p. 013305.
13. D. M. Bruls; T. H. Evers, J.A.H.K., P. J. W. van Lankvelt, M. Ovsyanko, E. G. M. Pelssers, J. J. H. B. Schleipen, F. K. de Theije, C. A. Verschuren, T. van der Wijk, J. B. A. van Zon, W. U. Dittmer, A. H. J. Immink, J. H. Nieuwenhuis and M. W. J. Prins;, *Rapid integrated biosensor for multiplexed immunoassays based on actuated magnetic nanoparticles.* Lab on a Chip, 2009. **9**: p. 7.
14. Q. Xu, et al., *Broadband light absorption enhancement in dye-sensitized solar cells with Au-Ag alloy popcorn nanoparticles.* Scientific Reports, 2013. **3:2112**: p. 1-7.
15. D. Boyer, et al., *Photothermal imaging of nanometer-sized metal particles among scatterers.* Science, 2002. **297**(5584): p. 1160-1163.
16. Y. Zhou and A. Hu, *From microjoining to nanojoining.* Open Surf. Sci. J., 2011. **3**: p. 32-41.
17. B. J. Roxworthy and K.C.T. Jr, *Femtosecond pulsed plasmonic nanotweezers.* Scientific Reports, 2012. **2:660**: p. 1-6.
18. P. Peng, et al., *Self-Oriented Nanojoining of Silver Nanowires via Surface Selective Activation.* Particle & Particle Systems Characterization, 2013. **30**(5): p. 420-426.
19. J. A. Fan, et al., *DNA-Enabled Self-Assembly of Plasmonic Nanoclusters.* Nano Letters, 2011. **11**(11): p. 4859-4864.

20. R. L. Stoermer and C. D. Keating, *DNA-directed assembly of barcoded nanowires onto glass slides for biosensing applications.* Smart Medical and Biomedical Sensor Technology Ii, 2004. **5588**: p. 51-58.
21. K. E. Sapsford, et al., *Selective DNA-mediated assembly of gold nanoparticles on electroded substrates.* Langmuir, 2008. **24**(18): p. 10245-10252.
22. H. Yao, et al., *DNA-directed self-assembly of gold nanoparticles into binary and ternary nanostructures.* Nanotechnol., 2007. **18**: p. 015102.
23. L. B. Zhong, et al., *Self-Assembly of Au Nanoparticles on PMMA Template as Flexible, Transparent, and Highly Active SERS Substrates.* Analytical Chemistry, 2014. **86**(13): p. 6262-6267.
24. P. Dey, et al., *Hyperbranched Polymer−Gold Nanoparticle Assemblies: Role of Polymer Architecture in Hybrid Assembly Formation and SERS Activity.* Langmuir, 2014. **30**: p. 2249−58.
25. C. M. Hangarter, et al., *Hierarchical magnetic assembly of nanowires.* Nanotechnology, 2007. **18**(20).
26. Y. Lu, et al., *Cold welding of ultrathin gold nanowires.* Nature Nanotechnol., 2010. **5**(3): p. 218-224.
27. S. C. Laza, et al., *Selective cold welding of colloidal gold nanorods.* Part. Part. Syst. Charact., 2013. **30**: p. 584-589.
28. C. Chen, et al., *Ultrasonic nanowelding of carbon nanotubes to metal electrodes.* Nanotechnol., 2006. **17**: p. 2192-2197.
29. P. Peng, A. Hu, and Y. Zhou, *Laser sintering of silver nanoparticle thin films: microstructure and optical properties.* Appl. Phys. A, 2012. **108**: p. 685-691.
30. S. J. Kim and D.J. Janga, *Laser-induced nanowelding of gold nanoparticles.* Appl. Phys. Lett., 2005. **86**: p. 033112.
31. L. Liu, et al., *Nanobrazing of Pt-Ag nanoparticles under femtosecond laser irradiation.* Nano-Micro Lett., 2013. **5**: p. 88-92.
32. Y. Peng, T. Cullis, and B. Inkson, *Bottom-up nanoconstruction by the welding of individual metallic nanoobjects using nanoscale solder.* Nano Lett., 2009. **9**(1): p. 91-96.
33. R. Chaim, *Electric field effects during spark plasma sintering of ceramic nanoparticles.* Journal of Materials Science, 2013. **48**(1): p. 502-510.
34. P. Saravanan, et al., *Consolidation of FePd nanoparticles by spark plasma sintering.* Intermetallics, 2010. **18**(11): p. 2262-2265.
35. S. Xu, et al., *Nanometer-scale modification and welding of silicon and metallic nanowires with a high-intensity electron beam.* Small, 2005. **1**(12): p. 1221-9.
36. M. José-Yacamán, et al., *Surface diffusion and coalescence of mobile metal nanoparticles.* J. Phys. Chem. B, 2005. **109**: p. 9703-9711.
37. H. Pan, S.H. Ko, and C. P. Grigoropoulos, *The solid-state neck growth mechanisms in low energy laser sintering of gold nanoparticles: a molecular dynamics simulation study.* J. Heat Transfer, 2008. **130**: p. 092404.
38. M. R. Zachariah and M. J. Carrier, *Molecular dynamics computation of gas-phase nanoparticle sintering: a comparison with phenomenological models.* J. Aerosol Sci., 1999. **30**(9): p. 1139-1151.
39. T. Yamakawa, et al., *Influence of joining conditions on bonding strength of joints: efficacy of low-temperature bonding using Cu nanoparticle paste.* J. Electronic Mater., 2013. **42**: p. 1260-1267.
40. H. Tohmyoh, et al., *Welding of Pt nanowires by Joule heating.* Scripta Materialia, 2007. **57**: p. 953-956.

41. F. Mafune, et al., *Nanoscale soldering of metal nanoparticles for construction of higher-order structures.* J. Am. Chem. Soc., 2003. **125**: p. 1686-1687.
42. A. Hu, Y. Zhou, and W. W. Duley, *Femtosecond Laser-Induced Nanowelding: Fundamentals and Applications.* Open Surf. Sci. J., 2011. **3**: p. 42-49.
43. D. von der Linde, K. Sokolowski-Tinten, and J. Bialkowski, *Laser–solid interaction in the femtosecond time regime.* Appl. Surf. Sci., 1997. **109/110**: p. 1-10.
44. L. Jiang and H. L. Tsai, *Improved two-temperature model and its application in ultrashort laser heating of metal films.* J. Heat Transfer, 2005. **127**(10): p. 1167-1173.
45. D. Palik, *Handbook of Optical Constants of Solids.* Academic Press, 1985. **1**: p. 50.
46. J. P. Holman, *Heat transfer*. 10th ed. McGraw-Hill series in mechanical engineering. 2010, Boston: McGraw Hill Higher Education. xxii, 725 p.
47. H. Wabnitz, et al., *Multiple ionization of atom clusters by intense soft X-rays from a free-electron laser.* Nature, 2002. **420**(6915): p. 482-485.
48. C. Unger, et al., *Time-resolved studies of femtosecond-laser induced melt dynamics.* Opt Express, 2012. **20**(22): p. 24864-72.
49. http://hyperphysics.phy-astr.gsu.edu/hbase/atmos/blusky.html.
50. K. Svoboda, and S. M. Block, *Biological applications of optical forces.* Annu. Rev. Biophys. Biomol. Struct., 1994. **23**: p. 247-285.
51. T. A. Nieminen, *Optical Manipulation Trapping Ions.* Nature Photonics, 2010. **4**(11): p. 737-738.
52. K. M. Mayer and J. H. Hafner, *Localized surface plasmon resonance sensors.* Chem Rev, 2011. **111**(6): p. 3828-3857.
53. K. A. Willets and R. P. Van Duyne, *Localized surface plasmon resonance spectroscopy and sensing.* Annual Review of Physical Chemistry, 2007. **58**: p. 267-297.
54. J. M. Pitarke, et al., *Theory of surface plasmons and surface-plasmon polaritons.* Rep. Prog. Phys., 2007. **70**: p. 1-87.
55. I. V. Bondarev, *Single-wall carbon nanotubes as coherent plasmon generators.* Phys. Rev. B, 2012. **85**(3).
56. M. Shahzad, et al., *Infrared surface plasmons on heavily doped silicon.* J. Appl. Phys., 2011. **110**(12).
57. M. A.Garcia, *Surface plasmons in metallic nanoparticles: fundamentals and applications.* J. Phys.D-Appl. Phys., 2011. **44**(28): p. 283001.
58. S. Agnihotri, S. Mukherji, and S. Mukherji, *Size-controlled silver nanoparticles synthesized over the range 5–100 nm using the same protocol and their antibacterial efficacy.* RSC Adv., 2014. **4**: p. 3974-3983.
59. E. Hutter and J. Fendler, *Exploitation of localized surface plasmon resonance.* Adv. Mater., 2004. **16**(19): p. 1685-1706.
60. J. R. Heath, *Size-dependent surface-plasmon resonances of bare silver particles.* Phys. Rev. B Condens. Matter., 1989. **40**(14): p. 9982-9985.
61. L. W. Chou, et al., *Tunable Mid-Infrared Localized Surface Plasmon Resonances in Silicon Nanowires.* Journal of the American Chemical Society, 2012. **134**(39): p. 16155-16158.
62. E. Ringe, et al., *Unraveling the Effects of Size, Composition, and Substrate on the Localized Surface Plasmon Resonance Frequencies of Gold and Silver Nanocubes: A Systematic Single-Particle Approach.* Journal of Physical Chemistry C, 2010. **114**(29): p. 12511-12516.
63. I. Pastoriza-Santos and L. M. Liz-Marzan, *Colloidal silver nanoplates. State of the art and future challenges.* Journal of Materials Chemistry, 2008. **18**(15): p. 1724-1737.
64. J. J. Mock, et al., *Shape effects in plasmon resonance of individual colloidal silver nanoparticles.* Journal of Chemical Physics, 2002. **116**(15): p. 6755-6759.

65. C. L. Nehl and J. H. Hafner, *Shape-dependent plasmon resonances of gold nanoparticles.* Journal of Materials Chemistry, 2008. **18**(21): p. 2415-2419.
66. L. Liu, et al., *Highly localized heat generation by femtosecond laser induced plasmon excitation in Ag nanowires.* Appl.Phys. Lett., 2013. **102**: p. 073107.
67. V. K. Valev, et al., *Plasmon-enhanced sub-wavelength laser ablation: plasmonic nanojets.* Adv. Mater., 2012. **24**(10): p. OP29-35.
68. S. Link, et al., *Laser-induced shape changes of colloidal gold nanorods using femtosecond and nanosecond laser pulses.* J. Phys. Chem. B, 2000. **104**(26): p. 6152-6163.
69. V. K. Valev, et al., *Plasmon-Enhanced Sub-Wavelength Laser Ablation: Plasmonic Nanojets.* Adv. Mater., 2012. **24**: p. OP29-OP35.
70. H. Xu and M. Kall, *Surface-plasmon-enhanced optical forces in silver nanoaggregates.* Phys. Rev. Lett., 2002. **89**(24): p. 246802.
71. M. Righini, et al., *Surface plasmon optical tweezers: tunable optical manipulation in the femtonewton range.* Phys. Rev. Lett., 2008. **100**(18): p. 186804.
72. M. Tokita, *Mechanism of spark plasma sintering.* Sumitomo Coal Mining Company, Ltd.
73. A. Plech, et al., *Femtosecond laser near-field ablation from gold nanoparticles.* Nature Phys., 2006. **2**: p. 44-47.
74. S. Mukherjee, et al., *Hot Electrons Do the Impossible: Plasmon-Induced Dissociation of H2 on Au.* Nano Lett, 2012(13): p. 240-247.
75. www.diss.fu-berlin.de/diss/servlets/MCRFileNodeServlet/FUDISS_derivate_000000001304/02_kap2.pdf?hosts=.
76. Y. Hu, et al., *Nanodevices in diagnostics.* Wiley Interdiscip Rev Nanomed Nanobiotechnol, 2011. **3**(1): p. 11-32.
77. N. Gandra, et al., *Plasmonic planet-satellite analogues: hierarchical self-assembly of gold nanostructures.* Nano Lett., 2012. **12**(5): p. 2645-2651.
78. R. M. Erb, et al., *Magnetic assembly of colloidal superstructures with multipole symmetry.* Nature, 2009. **457**(7232): p. 999-1002.
79. S. L. Biswal and A. P. Gast, *Rotational dynamics of semiflexible paramagnetic particle chains.* Phys. Rev. E, 2004. **69**(4 Pt 1): p. 041406.
80. T. Ding, K.Song, K. Clays, and C. Tung, *Fabrication of 3D Photonic Crystals of Ellipsoids: Convective Self-Assembly in Magnetic Field.* Advance Material, 2009. **21**: p. 1936-1940.
81. G. Jalani, et al., *Controlled biohybrid nanoprobes with silver nanoparticle clusters for Raman imaging.* Analyst, 2013. **138**(17): p. 4756-4759.
82. C. Shi, et al., *Manipulation and light-induced agglomeration of carbon nanotubes through optical trapping of attached silver nanoparticles.* Nanotechnol., 2008. **19**(21): p. 215304.
83. Y. Zhang, et al., *Optical trapping and light-induced agglomeration of gold nanoparticle aggregates.* Phys. Rev. B, 2006. **73**: p. 165405.
84. S. Ahlawat, R. Dasgupta, and P. K. Gupta, *Optical trapping near a colloidal cluster formed by a weakly focused laser beam.* J. Phys. D: Appl. Phys., 2007. **41**: p. 105107.
85. Y. Seol, A. E. Carpenter, and T. T. Perkins, *Gold nanoparticles: enhanced optical trapping and sensitivity coupled with significant heating.* Opt. Lett., 2006. **31**(16): p. 2429-2431.
86. A. J. Hallock, P. L. Redmond, and L. E. Brus, *Optical forces between metallic particles.* PNAS, 2005. **102**: p. 1280-1284.
87. M. Hu, et al., *Gold nanostructures: engineering their plasmonic properties for biomedical applications.* Chem. Soc. Rev., 2006. **35**(11): p. 1084-1094.
88. P. Peng, et al., *Functionalization of silver nanowire surfaces with copper oxide for surface-enhanced Raman spectroscopic bio-sensing.* J. Mater. Chem., 2012. **22**: p. 15495.

89. J. N. Israelachivili, *Intermolecular and Surface Forces (American Elsevier, third edition).* 2011: p. 71-166.
90. W. Haiss, et al., *Determination of size and concentration of gold nanoparticles from UV-vis spectra.* Anal. Chem., 2007. **79**(11): p. 4215-4221.
91. M. M. Jiang, et al., *Hybrid quadrupolar resonances stimulated at short wavelengths using coupled plasmonic silver nanoparticle aggregation.* J. Mater. Chem. C, 2014. **2**: p. 56-63.
92. A. Plech, et al., *Femtosecond laser near-field ablation from gold nanoparticles.* Nature Phys., 2005. **2**: p. 44-47.
93. G. Compagnini, G. C. Messina, L. D'Urso, E. Messina, M. G. Sinatra, O. Puglisi, and M. Zimbone, *Aggregation Phenomena and Electromagnetic Amplification Properties in Silver Nanoparticles Joined Through Highly Conjugated Carbon Chains.* Open Surf. Sci. J., 2011. **3**: p. 50-54.
94. J. R. Anema, et al., *Shell-Isolated Nanoparticle-Enhanced Raman Spectroscopy: Expanding the Versatility of Surface-Enhanced Raman Scattering.* Annu. Rev. Anal. Chem., 2011. **4**: p. 129-150.
95. A. Hu, P. Peng, H. Alarifi, X. Y. Zhang, J. Y. Guo, Y. Zhou, and W. W. Duley, *Femtosecond laser welded nanostructures and plasmonic devices.* J. Laser Applic., 2012. **24**: p. 042001.
96. F. Feng, et al., *SERS detection of low-concentration adenine by a patterned silver structure immersion plated on a silicon nanoporous pillar array.* Nanotechnol., 2009. **20**: p. 295501.
97. T. Sannomiya and J. Voros, *Single plasmonic nanoparticles for biosensing.* Trends Biotechnol., 2011. **29**(7): p. 343-351.
98. D. C. Marinica, et al., *Quantum Plasmonics: Nonlinear Effects in the Field Enhancement of a Plasmonic Nanoparticle Dimer.* Nano Lett., 2012. **12**: p. 1333-1339.
99. M. A. Asoro, et al., *Coalescence and sintering of Pt nanoparticles: in situ observation by aberration-corrected HAADF STEM.* Nanotechnol., 2010. **21**: p. 025701.
100. P. G. Roth and F. J. Boerio, *Surface-enhanced raman scattering from poly(4-vinyl pyridine).* J. Poly. Sci. Part B, 1987. **25**: p. 1923-1933.
101. A. C. Ferrari, and J. Robertson, *Raman spectroscopy of amorphous, nanostructured, diamond–like carbon, and nanodiamond.* Phil. Trans. R. Soc. Lond. A 2004. **362**: p. 2477-2512.
102. F. Piazza, A. Golanski, S. Schulze, and G. Relihan, *Transpolyacetylene chains in hydrogenated amorphous carbon films free of nanocrystalline diamond.* Appl. Phys. Lett., 2003. **82**: p. 358-360.
103. L. C. Nistor, et al., *Direct observation of laser-induced crystallization of a-C:H films.* Appl. Phys. A, 1994. **58**: p. 137-144.
104. M. J. Wesolowski, et al., *Synthesis of Polymer-like Hydrogenated Amorphous Carbon by fs-pulsed Laser Induced Plasma Processing of Solid Hexane.* Plasma Proc. Polym., 2012. **9**: p. 701-708.
105. P. Yang, et al., *Structure and properties of annealed amorphous hydrogenated carbon (a-C:H) films for biomedical applications.* Surf. Coat. Technol., 2004. **177-178**: p. 747-751.
106. Y. Borodko, et al., *Probing the Interaction of Poly(vinylpyrrolidone) with Platinum Nanocrystals by UV-Raman and FTIR.* J. Phys. Chem. B, 2006. **110**: p. 23052-23059.
107. Y. K. Du, et al., *Thermal decomposition behaviors of PVP coated on platinum nanoparticles.* J. Appl. Polym. Sci,, 2006. **99**(1): p. 23-26.
108. W. W. Duley, *UV Lasers: Effects and applications in materials science.* New York CUP, 1996: p. 67.
109. R. T. Sanderson, *Chemical bonds and bond energy (2d ed.).* Academic Press (London), 1976.

110. L. Calliari, M. Filippi, and N. Laidani, *Electron beam irradiation of hydrogenated amorphous carbon films.* Surf. Interf. Anal., 2004. **30**: p. 1126-1129.
111. Q. Ding, et al., *An explanation for laser-induced spallation effect in a-C:H films: Altered phase evolution route caused by hydrogen doping.* J. Appl. Phys., 2011. **109**: p. 013501.
112. T. V. Kononenko, et al., *Laser-induced spallation in diamond-like carbon films.* Appl. Phys. A, 2004. **79**: p. 543-549.
113. H. A. Alarifi, et al., *Molecular Dynamics Simulation of Sintering and Surface Premelting of Silver Nanoparticles.* Mater Trans, 2013. **54**(6): p. 884-889.
114. W. Widiyastuti, et al., *Sintering behavior of spherical aggregated nanoparticles prepared by spraying colloidal precursor in a heated flow.* Adv. Powder. Technol., 2009. **20**: p. 318-326.
115. H. O. Jeschke, et al., *Laser ablation threshold of silicon for different pulse durations:theory and experiment.* Appl. Surf. Sci., 2002. **197-198**: p. 839-844.
116. J. Park, et al., *Subwavelength light focusing using random nanoparticles.* Nature Photonics, 2013. **7**: p. 454-458.
117. A. Gloskovskii, et al., *Electron emission from films of Ag and Au nanoparticles excited by a femtosecond pump-probe laser.* Phys. Rev. B, 2008. **77**: p. 195427.
118. T. Döppner, et al., *Ion and electron emission from silver nanoparticles in intense laser fields.* Phys. Rev. A, 2006. **73**(3): p. 031202.
119. T. Ditmire, et al., *High intensity laser absorption by gases of atomic clusters.* Phys. Rev. Lett., 1997. **78**(16): p. 3121-4.
120. M. Kundu and D. Bauer, *Nonlinear resonance absorption in the laser-cluster interaction.* Phys. Rev. Lett., 2006. **96**(12): p. 123401.
121. Q. Jiang, S. Zhang, and M. Zhao, *Size-dependent melting point of noble metals.* Mater. Chem. Phys., 2003. **82**: p. 225-227.
122. É. Boulais, R. Lachaine, and M. Meunier, *Plasma mediated off-resonance plasmonic enhanced ultrafast laser-induced nanocavitation.* Nano Lett., 2012. **12**: p. 4763-4769.
123. Z. B. Wang, et al., *The influences of particle number on hot spots in strongly coupled metal nanoparticles chain.* J. Chem. Phys., 2008. **128**: p. 094705.
124. A. T. T. Tran, et al., *Influence of substrate surface conditions on the deposition and spreading of molten droplets.* Thin Solid Films, 2011. **219**: p. 2445-2456.
125. S. Brossard, et al., *Study of the splat formation for plasma sprayed NiCr on aluminum substrate as a function of substrate condition.* Surf. Coat. Technol., 2010. **204**: p. 2647-2656.
126. A. Habenicht, et al., *Jumping nanodroplets.* Science, 2005. **309**(5743): p. 2043-5.
127. A. H. Al-Bayati, et al., *Composition and structure of the native Si oxide by high depth resolution medium energy ion scattering* Surf. Sci., 1991. **241**: p. 91-102.
128. H. Tohmyoh, et al., *Welding of Pt nanowires by joule heating.* Scripta Materialia, 2007. **57**(10): p. 953-6.
129. H. Huang, et al., *Controlled joining of Ag nanoparticles with femtosecond laser radiation.* J. Appl. Phys., 2012. **112**: p. 123519.
130. M. Sobih, P. L. Crouse, and L. Li, *Elimination of striation in laser cutting of mild steel.* J. Phys. D-Appl. Phys., 2007. **40**(22): p. 6908-16.
131. A. W. Czanderna, *The adsorption of oxygen on silver* J. Phys. Chem., 1964. **68**: p. 2765-72.
132. S. Yang, W. T. Hill III, and S. N. Dixit, *Multiphoton dissociative ionization of O2: competition between dissociation and ionization in excited states.* J. Chem. Phys., 1994. **100**: p. 6434-44.

133. A. L' Huillier, G. Mainfray, and P. M. Johnson, *Multiphoton ionization versus dissociation of diatomic molecules irradiated by an intense 40 ps laser pulse.* Chem. Phys. Lett., 1984. **103**(6): p. 447-50.
134. Y. R. Luo, *Comprehensive handbook of chemical bond energies.* CRC Press (Boca Raton), 2007.
135. R. J. Dewhurst, *Comparative data on molecular gas-breakdown thresholds in high laser radiation fields.* J. Phys. D-Appl. Phys., 1978. **11**(16): p. L191-5.
136. D. R. Lide, *Ionization potentials of atoms and atomic ions* CRC Handbook of Chemistry and Physics (73rd Edition, CRC Press, Boca Raton), 1992: p. 10-211.
137. A. L. Myerson, *Silver catalyzed surface recombination in a step function flow of atomic oxygen.* J. Chem. Phys., 1963. **38**: p. 2043-5.
138. A. L. Myerson, *Mechanisms of surface recombination from step function flows of atomic oxygen over noble metals.* J. Chem. Phys., 1965. **42**: p. 3270-6.
139. B. V. L'vov, *Kinetics and mechanism of thermal decomposition of silver oxide.* Thermochimica Acta, 1999. **333**(1): p. 13-19.
140. S. A. Campbell, et al., *Single Nanoparticle Devices, A New Technique for Bottom-Up Manufacturing.* NSF Nanoscale Science and Engineering Grantees Conference, 2004. **Grant # 0304211**.
141. E. Marzbanrad, et al., *How morphology and surface crystal texture affect thermal stability of a metallic nanoparticle: the case of silver nanobelts and pentagonal silver nanowires.* Phys, Chem. Chem. Phys., 2015. **17**(1): p. 315-324.